

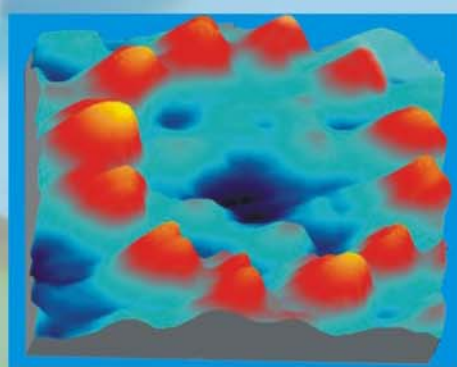
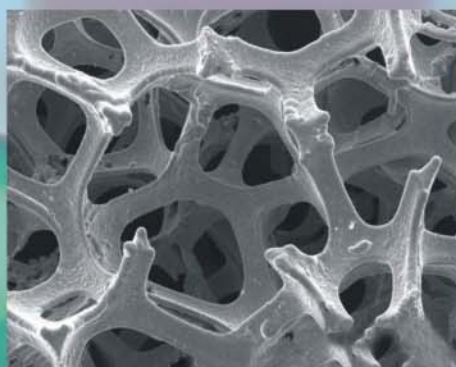
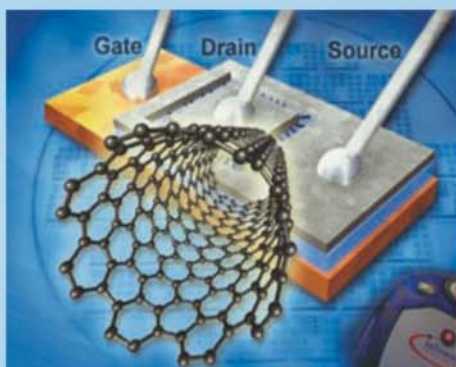


ISSN 2161-6221

From Knowledge to Wisdom

Journal of
**Materials Science
and Engineering**

Volume 3, Number 5, May 2013



Advanced Functional Solid-State Materials

David Publishing Company
www.davidpublishing.com

Journal of Materials Science and Engineering B

Volume 3, Number 5, May 2013 (Serial Number 20)



David Publishing Company
www.davidpublishing.org

Publication Information:

Journal of Materials Science and Engineering B (formerly parts of Journal of Materials Science and Engineering ISSN 1934-8959, USA) is published monthly in hard copy (ISSN 2161-6221) by David Publishing Company located at 9460 Telstar Ave Suite 5, EL Monte, CA 91731, USA.

Aims and Scope:

Journal of Materials Science and Engineering B, a monthly professional academic journal, particularly emphasizes new research results in realm of materials science and engineering. Articles interpreting practical application of up-to-date technology are also welcome.

Editorial Board Members:

Prof. M.V.V. Reddy (Singapore), Prof. Preecha Yupapin (Thailand), Prof. V.S. Vallabhapurapu (Pretoria), Prof. David Hui (New Orleans), Prof. Mustafa Acaroğlu (Turkey), Prof. Padmalochan Nayak (India), Prof. Maheshwar Sharon (India), Assoc. Prof. Muntean Edward Ioan (Cluj-Napoca), Assoc. Prof. Michalis Konsolakis (Greece), Dr. Emad Hassan Aly (Egypt), Dr. Wenqi Luan (Singapore), Dr. Starokadomsky Dmitro Lvovich (researcher, Ukraine).

Manuscripts and correspondence are invited for publication. You can submit your papers via web submission, or E-mail to materials@davidpublishing.org. Submission guidelines and web submission system are available at <http://www.davidpublishing.com>, www.davidpublishing.org.

Editorial Office:

9460 Telstar Ave Suite 5, EL Monte, CA 91731, USA

Tel: 1-323-984-7526, 323-410-1082

Fax: 1-323-984-7374, 323-908-0457

E-mail: materials@davidpublishing.org; materials1934-8959@hotmail.com

Copyright©2013 by David Publishing Company and individual contributors. All rights reserved. David Publishing Company holds the exclusive copyright of all the contents of this journal. In accordance with the international convention, no part of this journal may be reproduced or transmitted by any media or publishing organs (including various websites) without the written permission of the copyright holder. Otherwise, any conduct would be considered as the violation of the copyright. The contents of this journal are available for any citation. However, all the citations should be clearly indicated with the title of this journal, serial number and the name of the author.

Abstracted / Indexed in:

Chemical Abstracts Service (CAS)

Database of EBSCO, Massachusetts, USA

Cambridge Science Abstracts (CSA)

Ulrich's Periodicals Directory

Summon Serials Solutions

Chinese Database of CEPS, Airiti Inc. & OCLC

Chinese Scientific Journals Database, VIP Corporation, Chongqing, China

ProQuest

Subscription Information:

Print \$520, Online \$360, Print and Online \$680 (12 issues)

David Publishing Company

9460 Telstar Ave Suite 5, EL Monte, CA 91731, USA

Tel: 1-323-984-7526, 323-410-1082; Fax: 1-323-984-7374, 323-908-0457

E-mail: order@davidpublishing.com



David Publishing Company
www.davidpublishing.com

Journal of Materials Science and Engineering B

Volume 3, Number 5, May 2013 (Serial Number 20)

Contents

Technological Studies

- 263 **Study of the Adsorption Space of Modified Clinoptilolites**
Rolando Roque-Malherbe, Alba N. Costa-Hernandez, Christymarie Rivera-Maldonado, Frances N. Lugo-Alvarado and Ramon Polanco-Estrella
- 281 **Application of Two-Color LIF Thermometry to Nucleate Boiling**
Nadine Kosseifi, Pascal Henry Biwole, Christian Mathis, Germain Rousseaux, Séverine Agnès Éliette Boyer, Harunori Nakagawa Yoshikawa and Thierry Coupez
- 291 **Effect of the Al_2O_3 and BaO Addition on the Thermal and Physical Properties of Ternary Glass System (B_2O_3 - BaO- Al_2O_3)**
Djamila Aboutaleb, Brahim Safi, Azzeddine Ayadi and Aicha Iratni
- 298 **Research into Excited Long Lived 0.6-6.0 keV Energy Levels in the Cathode Solid Medium of Glow Discharge by X-Ray Spectra Emission**
Alexander Borisovich Karabut
- 305 **New Composite Electrode Material Based on Glassy Carbone/Polythiophene/ MnO_2**
Imene Chikouche, Ali Sahari, Fahima Charef and Ahmed Zouaoui
- 310 **Gas Sensing Mechanism of Metal Oxide Doped PANi Composites**
Kailash R. Nemade and Sandeep A. Waghuley
- 314 **Evaluation of Effect of Eddy Currents in PLC Influenced by Atmospheric Corrosion in the Electronics Industry**
Gustavo López Badilla, Elizabeth Romero Samaniego, Sandra Luz Toledo Perea, Miriam Maleny García Castrellon and Luis Alberto Gameros Rios
- 322 **The Influence of the Concentration of Dissolved Substances in the Effluent Sulfate Pulp and Paper Mills on the Productivity of Semi-Permeable Membranes**
Terpugov Grigory, Truberg Arseniy, Katsereva Olga and Terpugov Daniil

Theoretical Studies

- 326 **Classification of Raw Sources of Rare-Earth Elements in Kazakhstan**
Madali Naymanbayev, Nina Lokhova and Zhazira Baltabekova

Study of the Adsorption Space of Modified Clinoptilolites

Rolando Roque-Malherbe, Alba N. Costa-Hernandez, Christymarie Rivera-Maldonado, Frances N. Lugo-Alvarado and Ramon Polanco-Estrella

Institute for Physical Chemical Applied Research, School of Science, University of Turabo, Gurabo, PR 00778-3030, USA

Received: February 14, 2013 / Accepted: March 15, 2013 / Published: May 25, 2013.

Abstract: Carbon dioxide (CO₂) adsorption is an important adsorbent characterization method and a significant industrial process. In separation and recovery technology, the adsorption of the CO₂ is important to reduce the concentration of this gas considered as one of the greenhouse gases. Natural zeolites, particularly clinoptilolite, are widely applied as adsorbents. In this regard, in the present research, the structure, composition and morphology of modified with hexafluorosilicate (HFSi) and orthophosphoric acid (H₃PO₄) clinoptilolites were investigated by characterizations and measurements made with, X-ray diffraction (XRD), thermogravimetric analysis (TGA), scanning electron microscopy-energy dispersive X-ray analysis (SEM-EDAX) and gravimetric adsorption. Additionally, the surface Chemistry of the modified clinoptilolites was analyzed by applying diffuse reflectance fourier transform infrared spectrometry (DRIFTS). Further, the interaction of CO₂ within the adsorption space of these modified clinoptilolites and a synthetic ZSM-5 zeolite was studied with the help of adsorption measurements. After all, an appropriate theoretical methodology for the analysis of the XRD and adsorption data was applied. The calculated cell parameters of the tested are similar to those reported for a typical clinoptilolite of: $a = 17.662 \text{ \AA}$, $b = 17.911 \text{ \AA}$, $c = 7.407 \text{ \AA}$ and $\beta = 116.40^\circ$. The resolution of the TGA derivative profiles indicated the presence of two steps for water release, one of them represents the loss of majority of the water present in the micropores. This was evidenced as a broad peak centered at about 50°C for the CSW-HFSi-0.1, but at 100°C for the samples CSW-HFSi-0.4. The SEM micrographs corresponding to the modified clinoptilolites, was evidenced that the CSW zeolite shows secondary particles exhibiting diameters from 3 to $40 \mu\text{m}$, formed by primary clinoptilolite crystallites showing a crystallite size, $\Phi = 40 \text{ nm}$. The EDAX elemental analysis it can be demonstrated that the exchange process replaced about 85% of the charge compensating ions. The DRIFT spectra of the modified clinoptilolites, specifically, CSW-HFSi-0.1, show a narrow band at about: $3,740 \text{ cm}^{-1}$ corresponding to terminal silanol groups (Si-OH) and a band $3,600\text{-}3,650 \text{ cm}^{-1}$ resulting from extra-framework Al-OH. With the precision of the measured micropore volumes related to the excellent fitting of the adsorption data by the D-R isotherm equation, it can be affirm that carbon adsorption took only place in the micropore region. The isosteric heat of adsorption calculated for the modified clinoptilolites was greater than those values reported of ZSM-5 zeolite, particle packing silica, dealuminated Y zeolite (DAY) Cd, Zn and Ni-nitroprussides and Cu-nitroprusside and a Ni-MOF. With the obtained result it can be concluded that the modified clinoptilolites with HFSi showed a quality as adsorbent comparable to commercial synthetic zeolites.

Key words: Natural zeolites, modification, clinoptilolite, carbon dioxide, adsorption space, surface chemistry.

1. Introduction

Adsorption is a very important industrial process, and it is the source of many methods for the study of the adsorption space of adsorbents [1-5]. Natural zeolites are significant materials as adsorbents [6-12]

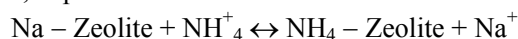
and other uses such as, ion exchangers [13, 14], catalysts [15, 16], catalyst supports [17, 18], ion conductors [19, 20], the production of porous [21] and hard ceramics [22]. These minerals are mined from deposits, where the zeolitic phases are mixed, principally, with montmorillonite, quartz, calcite, feldspars, magnetite and volcanic glass [8, 9]. However, in some cases it is possible to find highly pure

Corresponding author: Rolando Roque-Malherbe, professor, research fields: physical chemistry of materials, energy and pollution abatement applications. E-mail: rroque@suagm.edu and rroqueumalh@aol.com.

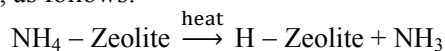
materials, to be precise, more than 90 wt% of a single zeolitic phase in the mineral [11, 21]. In this regard, the main reason to conduct this research is the modification of a highly pure natural zeolite adsorbent to produce an adsorbent comparable to synthetic zeolite. In other word, the modification of a powdered clinoptilolite rock to produce a functional adsorbent.

For gas-phase applications commercial zeolites are applied as adsorbents in different bound forms, composed of the zeolite and a binder to produce a reliable adsorption bed and prevent an extreme pressure drop [23]. Typically the zeolite content of the bound form is, in general, around 85-90 wt.% [2]. Clinoptilolite, the most abundant natural zeolite could be found with a zeolite content in the rock up to 85-90 wt.% [9, 21]. Besides, natural zeolite rocks are harder than commercial zeolite bound forms [22]. Further, if natural zeolites are properly crushed, approximately spherical particles, with a diameter 1-10 mm, could be obtained. If these particles are modified by ion exchange and chemical and heat treatments we consider that will be produced materials with more zeolite per weight and with a quality as adsorbent comparable in many applications to commercial zeolites.

The character of the zeolite micropore surface is strongly affected by the nature of their surface sites. In this sense, a zeolite exchanged with ammonium cations, expressed as follow:



It can be transformed into an acid zeolite by the thermal decomposition of the exchanged ammonium cations, as follows:



In this situation, protons are connected to the zeolite oxygen atoms forming OH bridged groups. These sites are responsible for the Brönsted acidity of natural and other aluminosilicate zeolites. The hydroxyl bridged groups have been widely studied by, IR spectrometry [24], microcalorimetry [25], nuclear magnetic resonance [26], and other methods [27, 28]. Between other conclusions, it was proposed that the

acidity of these sites is related with the ease of the proton to be released, i.e., if the interaction between the proton and the oxygen is weaker the Brönsted site should be more acid and the zeolite more active as an acid catalyst [24-29]. This inference, however, is not totally exact, since other effects, influences the properties of these acid sites [28]. In this regard, sorption effects are responsible for changes in the reaction rates of paraffin cracking, a reaction catalyzed by acid zeolites [30, 31].

One of the methods to increase the acidity of acid zeolites is dealumination. This process can be done for example: by hydrothermal treatments (steaming), acid leaching, or with treatments in flowing silicon tetrachloride (SiCl_4) or hexafluorsilicates ($(\text{NH}_4)_6\text{SiF}_6$) [24]. These dealumination methods could increase the amount of zeolite in the sample, eliminate charge compensating cations to open the zeolite channels, create mesopores and increase the adsorption field. All these improvements could lead to a useful adsorbent.

To show that a material is a good adsorbent, carbon dioxide adsorption could provide very useful information about the adsorption space of microporous materials [32], where, the adsorption space, is the three dimensional location, where molecules are subjected to the adsorption force fields [33].

One of the important applications of carbon dioxide adsorption as a characterization tool is the measurement of the: micropore volume, the most important parameter for the geometrical characterization of the adsorption space of microporous materials. Usually, these measurements are carried out with the help of nitrogen adsorption isotherms measured at -196°C [3, 5]. But at such a low temperature, the transport kinetics of the nitrogen molecules through the micropores is very slow in pores smaller than 0.7 nm. But, in the case of carbon dioxide adsorption, at 0°C the higher temperature of adsorption applied cause that the carbon dioxide molecules have a bigger kinetic energy;

subsequently, they are capable to go into the microporosity for pores of sizes less than 0.7 nm [32]. Therefore, an experimental solution for this difficulty is the use of carbon dioxide adsorption at 0 °C instead of nitrogen at -196 °C, in order to apply the Dubinin adsorption isotherm to describe carbon dioxide adsorption. The obtained data can be used for the determination of the micropore volume and the calculation of the isosteric heat of adsorption in order to qualify the geometry and the nature of the interaction between carbon dioxide and the zeolite framework, allowing, in sum, the characterization of the geometry and the interactions within the adsorption space [5, 10].

Carbon dioxide adsorption is not only an important adsorbent characterization method but it is an important industrial application of adsorbents. In this regard, the separation and recovery of carbon dioxide is a very important research problem; since it is a greenhouse gas which contributes to global warming and a reactant in significant industrial processes; as for example the Solvay process for the production of NaHCO_3 [35-37]. Independently of the carbonaceous adsorbents, molecular sieves, alumina or silica gel can be applied for carbon dioxide separation. The activated alumina is currently considered the most suitable sorbent for removing carbon dioxide from air in the pressure swing adsorption (PSA) process [37]. Nevertheless, cheap and environmentally friendly natural zeolite materials, with high micropore volume and strong surface interaction with the carbon dioxide molecule have potential applications in carbon dioxide separations [38].

In these research the structure, composition and morphology of clinoptilolites modified with hexafluorosilicate (HFSi) and orthophosphoric acid (H_3PO_4), with measurements and characterizations by means of, X-ray diffraction (XRD), thermogravimetric analysis (TGA), scanning electron microscopy-energy dispersive X-ray analysis (SEM-EDAX) and gravimetric adsorption measurements.

Further, was studied the surface chemistry of the modified clinoptilolites and the interaction of carbon dioxide with the framework of the modified clinoptilolites, two synthetic ZSM-5 zeolites used for comparison and data previously obtained for the adsorption of carbon dioxide in amorphous silica and a dealuminated Y zeolite [34], a metal organic framework [39], and four nitroprussides [40, 41] by applying diffuse reflectance Fourier transform infrared spectrometry (DRIFTS) and adsorption measurements with the help of an automatic adsorption analyzer. Finally an appropriate theoretical methodology for the analysis of the X-ray diffraction profiles and the adsorption data was applied [5, 34, 39-41]. As far as we know the modification of clinoptilolite with HFSi to improve their adsorption properties had not been previously attempted.

2. Experiments

2.1 Materials and Modification Procedures

All the consumable chemicals were analytical grade without additional purification. The water used in the synthesis process was bi-distilled.

The natural zeolite studied in the present research was a clinoptilolite mined in the deposit located in Sweetwater, Wyoming, USA. The sample was provided by ZeoponiX Inc., Louisville, Colorado. This natural zeolite was labeled Clinoptilolite Sweetwater (CSW). The measured mineralogical composition of this material was, clinoptilolite, 90 ± 5 wt.%, and the rest, montmorillonite (2 wt.%), quartz (2 wt.%), calcite (2 wt.%), feldspars (1 wt.%), magnetite (1 wt.%) and volcanic glass (2 wt.%).

A powdered sample of CSW clinoptilolite of 30 to 40 meshes (0.4-0.6 mm) was modified by an ion exchange treatment with a 1 M ammonium chloride solution (NH_4Cl) to get the sample $\text{NH}_4\text{-CSW}$ [13]. This solution was prepared with 13.40 g of ammonium chloride in 250 mL of deionized water (DDW). 25 g of natural zeolite were exchanged in

reflux five times with the 1 M NH_4Cl solution at 100 °C, each exchange had a duration of 3 h. This treatment produced an ammonium clinoptilolite that was identified as $\text{NH}_4\text{-CSW}$. This zeolite was thereafter filtered, washed exhaustively with bi-distilled water and dried in an oven at 70 °C. Further, the ammonium clinoptilolite was dealuminated with a 0.1 M solution of ammonium hexafluorosilicate (HFSi), explicitly: $(\text{NH}_4)_6\text{SiF}_6$ [24]. This solution was prepared with 0.05 g of $(\text{NH}_4)_6\text{SiF}_6$ in 500 mL of DDW. Another 0.4 M solution was prepared with 0.20 g of $(\text{NH}_4)_6\text{SiF}_6$ in 500 mL of DDW. A sample of 10 g of ammonium zeolite was refluxed for four h with 500 mL of 0.1 M $(\text{NH}_4)_6\text{SiF}_6$ at 80 °C. The same treatment was given to another 10 g of ammonium zeolite but with a 0.4 M solution of $(\text{NH}_4)_6\text{SiF}_6$. Following this treatment, each sample was filtered, washed exhaustively and dried in an oven at 70 °C. Finally each sample was calcined at 500 °C for a period of 2 h. The calcined sample prepared with 0.1 M HFSi was identified as CSW-HFSi-0.1 and the calcined sample prepared with 0.4 M of HFSi was identified as CSWHFSi-0.4.

The natural clinoptilolite was also dealuminated with orthophosphoric acid. To be precise, 20 g of natural clinoptilolite was refluxed with a 4 M solution of orthophosphoric acid (H_3PO_4) at 100 °C, for a period of 20 min. After the treatment with H_3PO_4 the sample was washed and dried in an oven at 70 °C. This treatment resulted in the clinoptilolite dealumination by isomorphous replacement of aluminum atoms by phosphorus atoms [18]. The samples dealuminated with orthophosphoric acid were identified as CSW- H_3PO_4 -20 and CSW- H_3PO_4 -40.

To compare our data were tested three synthetic zeolites, H-ZSM-5 (CBV-3020, $\text{SiO}_2/\text{Al}_2\text{O}_3 = 32$) and H-ZSM-5(CBV5020, $\text{SiO}_2/\text{Al}_2\text{O}_3 = 53$), both provided by the PQ Corporation and one Na-X, provided by Laporte [12]. Additionally, was studied a homoionic sodium natural clinoptilolite from the deposit located in Castillas, Havana, Cuba,

labeled Na-HC [17]. The mineralogical composition of this zeolite rock labeled HC was clinoptilolite 85 ± 5 wt.%, and the rest montmorillonite (5-6 wt.%), quartz (3-4 wt.%), calcite (1-2 wt.%), feldspars (1-2 wt.%), magnetite (0-1 wt.%) and volcanic glass (1-2 wt.%) [9]. The HC zeolite was exchanged with a 1 M sodium chloride solution in reflux, five times at 100 °C, for a period of three h to get the Na-HC sample [17]. Finally, the CSW zeolite was exchanged with sodium, following the process applied in the case of the HC sample, to produce the homoinic zeolite Na-CSW [21].

2.2 Characterization Methods.

X-ray diffraction tests were carried out with a Bruker D8 Advance system in a Bragg- Brentano vertical goniometer configuration. The angular measurements were made with a (Theta/2Theta) of ± 0.0001 reproducibility, by applying steps of 0.01° from 5° to 40° to get XRD profiles that could be accurately resolved by least square methods. The X-ray radiation source was a ceramic X-ray diffraction Cu anode tube type KFL C 2 K of 2.2 kW, with long fine focus.

A variable computer-controlled motor driven divergence slit with 2.5° Soller slits were included to allow kept the irradiated area on the sample surface constant. A Ni filter was placed, prior to the detector, to eliminate $\text{Cu-K}\beta$ radiation. A LynxEyeTM one-dimensional detector was employed. This detector is based on a Bruker AXS compound silicon strip technology and increases measured intensities, without sacrificing resolution and peak shape. This together with the use of small scanning step resulted in high quality XRD profiles suitable for mathematical treatment [39-41].

The TGA testing process was carried out with a TA, Q-500 equipment. To make the TGA test, the samples were placed into a ceramic sample holder, which is suspended from an analytical balance. Then, the sample holder was heated according to a

predetermined thermal cycle, that is: the temperature was linearly scanned, from 27 to 350 °C, at a heating rate of 5 °C/min, in a flow of 100 mL/min of the purge gas that is pure N₂. The data collection, the temperature control, the programmed heating rate, and the gas flow control, were automatically controlled by the software of the TA, TQ500 TGA. The TGA data was collected as a weight percent $W(t)$ versus T (°C) profile, where: $W(T) = (M(T)/M_0) \times 100$, is the per-cent ratio of the sample mass during the thermal treatment, $M(T)$, and the initial mass of the sample M_0 .

Elemental chemical analysis of the tested samples were performed using an energy dispersive X-ray (EDAX) spectrometer coupled to a JEOL Model JSM-6360 scanning electron microscope (SEM), equipped with an energy dispersive X-ray analysis detector and with a JEOL JLSM-6000 SEM and EDAX analysis system. The acceleration of the electron beam was 20 kV in both cases. The sample grains were placed on a carbon tape, and then introduced into the sample-holder. In order to guarantee, that we were testing a sample with a homogeneous distribution within the sample, different spots were analyzed. Together with the EDAX analysis scanning electron micrographs of the tested samples were obtained.

To get the diffuse reflectance infrared Fourier transform spectra, was applied a Thermo Scientific Nicolet iS10 FTIR spectrometer with the Smart Collector for diffuse reflectance analysis and the environmental chamber for the smart collector. The spectra were collected with a resolution of 4 cm⁻¹ and were made 100 scans per sample. To get the spectra in the case of the dehydrated samples, a background with KBr (FTIR pure, provided by Nicolet) located in the sample holder of the environmental chamber was made by applying the same conditions used to get, later, the sample spectra. To dehydrate the samples, it were heated, at 300 °C, under N₂ (Praxair, 99.99%) flow at a rate of 50 cc/min for a duration of 2 h. Lastly, the spectra of the dehydrated zeolite were obtained

with the sample inside the environmental chamber, at room temperature, under N₂ (Praxair, 99.99%) flow at a rate of 50 cc/min.

Water adsorption was measured gravimetrically at atmospheric pressure in air containing water vapor at different partial pressures [10, 11]. To study carbon dioxide adsorption, isotherms were collected, in an upgraded Quantachrome Autosorb-1 automatic physisorption analyzer, the adsorption isotherms of CO₂ at 0 °C were collected for samples degassed at 300 °C for a period of three h in high vacuum (10⁻⁶ Torr). In this case since the carbon dioxide vapor pressure, P_0 , at 0 °C, is high, to be precise, $P_0 = 26,141$ Torr, subsequently, we will be working in the following relative pressure range: $0.00003 < P < 0.03$. The experience indicates that the adsorption process in this range is very well described by the Dubinin adsorption isotherm equation [42]. The Dubinin-Astakhov (D-A) adsorption isotherm equation can be represented in a log-log scale as follows [43]:

$$\ln(n_a) = I(N_a) - \left(\frac{RT}{E}\right)^n \ln\left(\frac{P_0}{P}\right)^n \quad (1)$$

This relation, describes the relation between the amount adsorbed, n_a , and the inverse of the relative pressure, i.e., P/P_0 . Where, E , is a parameter named the characteristic energy of adsorption, N_a , is the maximum amount adsorbed in the volume of the micropore, and, n ($1 < n < 5$) is an empirical parameter. This equation is a very powerful tool for the description of the experimental data of adsorption in microporous material [42, 43]. The fitting process of Eq. (1) allowed us to calculate the best fitting parameters, i.e., N_a , E , and n . If, $n = 2$, we get the Dubinin-Radushkevitch (D-R) equation that was the equation applied here. Then, with the help of the CO₂ adsorption isotherms and Eq. (1) with: $n = 2$, the micropore volume, $W_{MP} = N_a V_L$ (where V_L is the molar volume CO₂ at 0 °C) and the characteristic energy of adsorption, E (kJ/mol) were measured [5, 39-41].

3. Results and Discussion

In Fig. 1a, it is shown that the XRD profiles of the modified samples and in Figs. 1b and 1c the details of the patterns corresponding to the samples, $\text{NH}_4\text{-CSW}$, CSW-HFSi-0.1 and $\text{CSW-H}_3\text{PO}_4\text{-20}$. The search carried out with the PDF-2, 2009 release database, created by the International Center for Diffraction Data produced a match of the XRD profile of the modified samples with the profiles of clinoptilolite. The clinoptilolite framework type is HEU; whose maximum space group (SG) symmetry is the monoclinic, $C2/m$ (SG No. 12) [44]. The cell parameters data reported for a representative clinoptilolite are: $a = 17.662 \text{ \AA}$, $b = 17.911 \text{ \AA}$, $c = 7.407 \text{ \AA}$ and $\beta = 116.40$ [45]. We calculated the cell parameters, of the modified clinoptilolite samples by fitting the XRD profiles of these materials with mathematical functions simulating XRD patterns by applying the Pawley method [46]. These calculations were concretely made supposing the $C12/m1$ (No. 12) space group. In Table 1, are reported the calculated cell parameters for this space group alongside the Gaussian crystallite size (Φ). The TOPAZ software together with the Pawley calculations made the corrections to separate instrumental and strain effects from the crystallite size by applying the Williamson-Hall method [47]. The calculations were made by assuming a spherical shape for the Gaussian crystallite size (Φ). Further, in Fig. 2 is reported one of the fitted profiles as an illustration of the performed process. The calculated parameters are similar to those reported for a typical clinoptilolite [45]. But, a variation of the values of these parameters throughout the dealumination process was observed (Table 1 and Fig. 1b). These differences could be linked to the ionic radius of Al^{3+} and Si^{4+} in tetragonal coordination (0.39 \AA for Al^{3+} and 0.26 \AA for Si^{4+} [48]).

The state of the zeolitic water is also important for the structural characterization of these materials. TGA data can be applied as a means for the study of the

state of water in porous materials, since in the hydrated state the TG profile of these materials, from

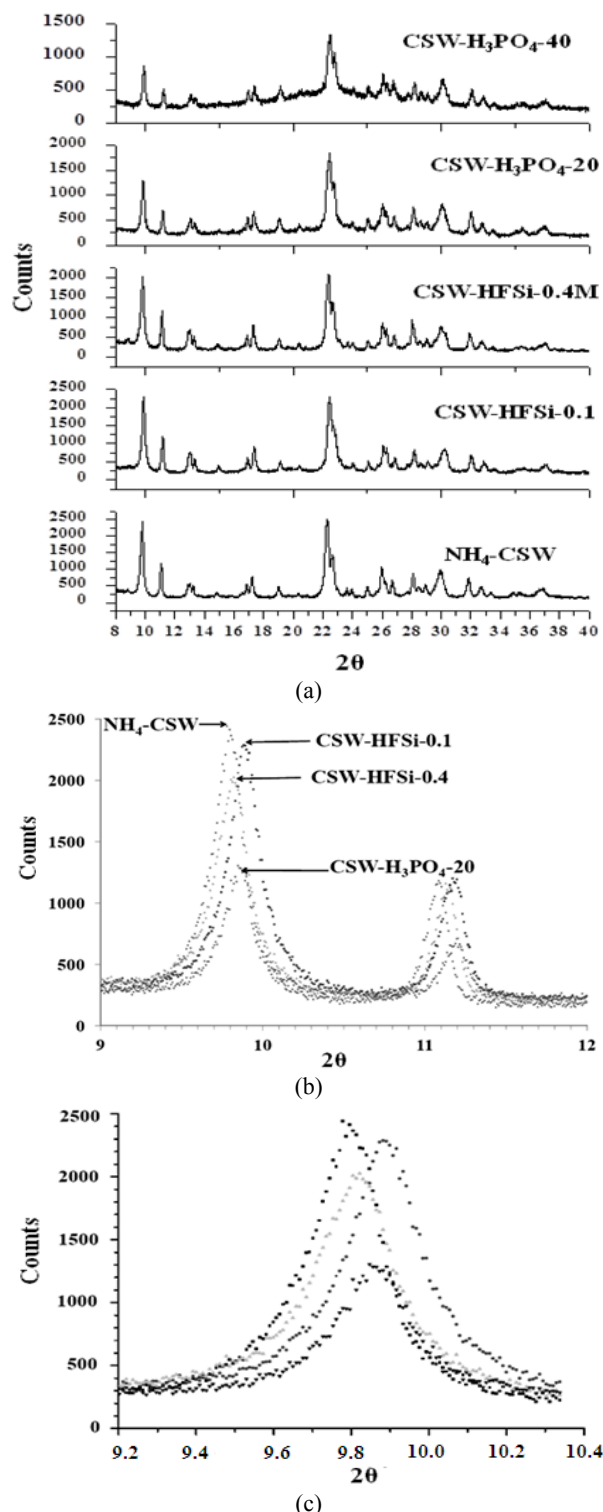
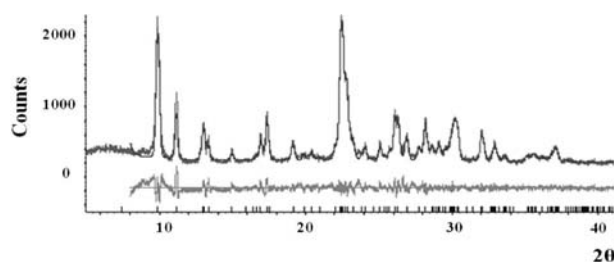


Fig. 1 XRD profiles of the modified natural clinoptilolites (a) detail of samples $\text{NH}_4\text{-CSW}$, CSW-HFSi-0.1 , CSW-HFSi-0.4 and $\text{CSW-H}_3\text{PO}_4\text{-20}$.

Table 1 Cell parameters for the treated clinoptilolite samples calculated with the Pawley method assuming the $C2/m$ space group and Gaussian crystallite size (Φ).

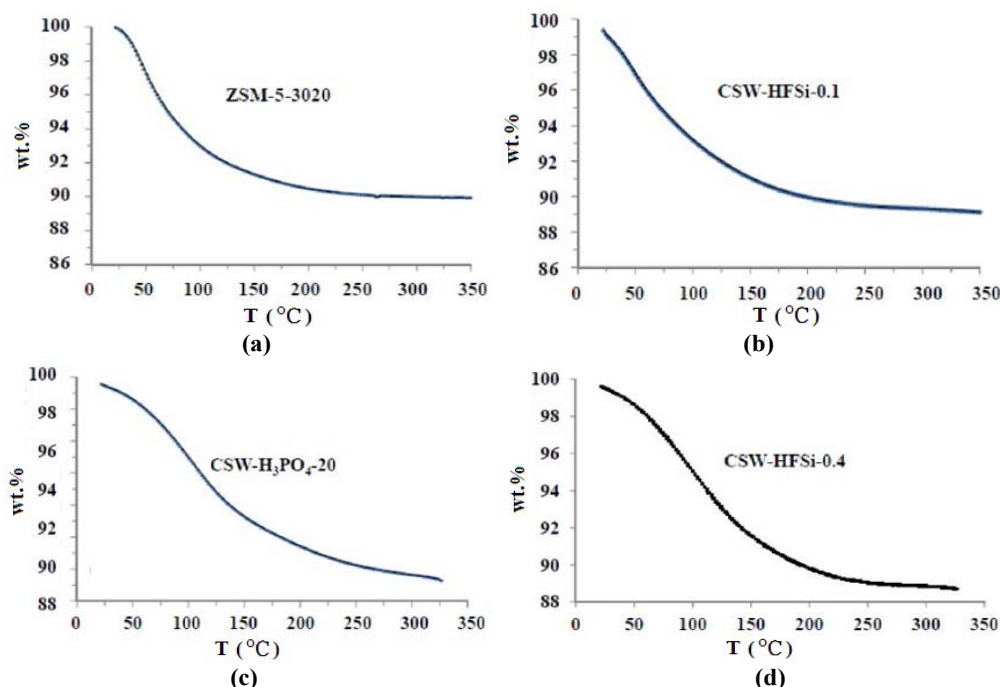
Sample	a (Å)	b (Å)	c (Å)	β (degree)	V (Å ³)	ϕ (nm)
CSW-NH ₄	17.693 (4)	17.959 (4)	7.404 (6)	116.01 (1)	2,114 (1)	40 (1)
CSW-HFSi-0.1	17.659 (4)	17.858 (3)	7.394 (5)	116.34 (1)	2,089 (1)	39 (1)
CSW-HFSi-0.4	17.688 (5)	17.965 (3)	7.403 (1)	116.31 (1)	2,108 (1)	39 (1)
CSW-H ₃ PO ₄ -20	17.672 (4)	17.975 (6)	7.416 (6)	116.33 (1)	2,111 (1)	37 (1)
CSW-H ₃ PO ₄ -40	17.695 (8)	17.99 (1)	7.411 (2)	116.18 (1)	2,116 (1)	29 (1)

**Fig. 2** XRD profile of the CSW-HFSi-0.1 sample fitted with the Pawley method for the $C2/m$ space group (c).

30 to 300 °C, is merely a water thermo-desorption profile (Fig. 3). During the TG analysis, the process of water thermo-desorption occurs by the release of water adsorbed in different sites of the zeolite tunnels. In Fig. 4, the resolved TGA derivative profiles corresponding to the modified natural clinoptilolites: CSW-HFSi-0.1, CSW-HFSi-0.4, CSW-H₃PO₄-20 and

the ZSM-5 (CBV-3020) are shown. These profiles were resolved by fitting a theoretical profile, computed as the sum of two Lorentzian functions, to the experimental data by applying the peak separation and analysis software Peak Fit (Seasolve Software Inc., Framingham, Massachusetts) based on the least square procedure. The experimental profile is the continuous line, this profile is fitted by the theoretical function illustrated by the dashed line, further, the two peaks employed to compute the calculated profile are shown also as dashed curves (Fig. 4).

The resolution of the TGA derivative profiles indicated the presence, essentially, of two steps for water release. During the first, was lost the majority of the water present in the micropores. This thermal effect

**Fig. 3** TGA profiles of the modified natural clinoptilolites: (a) the ZSM-5 (CBV-3020), (b) CSW-HFSi-0.1, (c) CSW-H₃PO₄-20 and (d) CSW-HFSi-0.4.

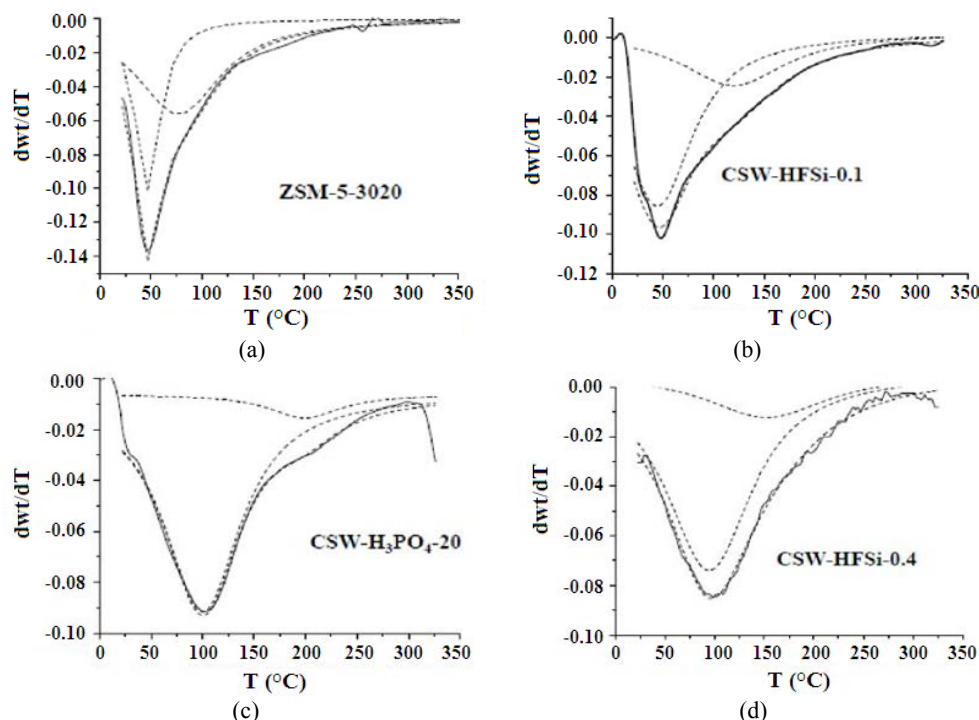


Fig. 4 TGA derivative profiles of the modified natural clinoptilolites: (a) ZSM-5 (CBV-3020), (b) CSW-HFSi-0.1, (c) CSW-H₃PO₄-20 and (d) the CSW-HFSi-0.4.

was evidenced as a broad peak centered at about 50 °C for the samples ZSM-5 (CBV-3020) and CSW-HFSi-0.1, but at 100 °C for the samples CSW-HFSi-0.4 and CSW-H₃PO₄-20. The second effect was placed at around 75 °C for the sample ZSM-5 (CBV-3020), but at 125 °C for CSW-HFSi-0.1, 150 °C for CSW-HFSi-0.4 and 175 °C for CSW-H₃PO₄-20 (Fig. 4). The first process characterized the release of physically adsorbed water from an energetically heterogeneous adsorbent as a zeolite [10], to be precise, since water was released at different temperatures, these facts mean that it was linked with different adsorption energies to the framework. The second peak was related to the removal of coordinated water.

Fig. 5 is reported the DRIFTS spectrum of the difference spectra of the modified natural clinoptilolite CSW-HFSi-0.1 after a treatment at 250 °C under nitrogen flow by two h and after the same treatment at 500 °C. To get this spectrum the sample located in the sample holder of the environmental chamber was dehydrated at 250 °C, under N₂ (Praxair,

99.99%) flow at a rate of 50 cc/min for a duration of 2 h and then the temperature was lowered to room temperature. A DRIFT spectrum was taken at that moment and saved as background. Later, the spectrum of the sample at room temperature after a treatment inside the environmental chamber, at 500 °C, under N₂ (Praxair, 99.99%) flow at a rate of 50 cc/min was collected. The resulting spectrum is difference spectrum shown in Fig. 5. This DRIFTS profile indicated that all the water contained in the studied zeolite was removed after the first treatment at 250 °C. This result was coincident with the TGA data (Fig. 3), which indicated that water was totally released from the modified sample CSW-HFSi-0.1 at 250 °C. Consequently, these samples were, totally dehydroxylated during the modification treatment. As a result all the water released during the TGA process was only located in the adsorption space of the zeolite CSW-HFSi-0.1.

In sum, the TGA and DRIFTS data previously discussed indicated that all the water was released up to 250 °C in two steps. These steps can be related, in

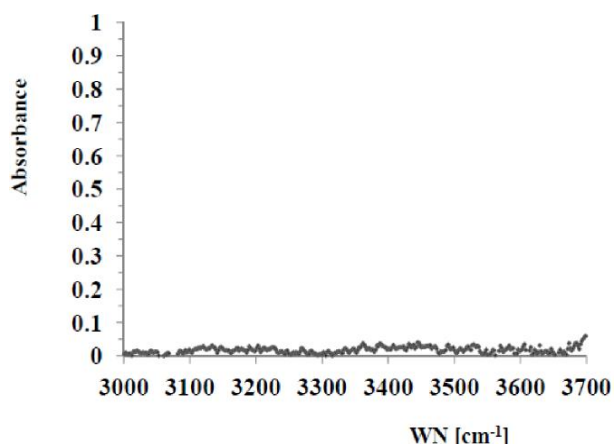


Fig. 5 DRIFTS spectrum of the difference spectra of the modified natural clinoptilolite CSW-HFSi-0.1 after a treatment at 250 °C under nitrogen flow by two h and after the same treatment at 500 °C.

sequence, to the removal of water physically adsorbed on the micropore and coordinated water, respectively [41].

Fig. 6 shows the SEM micrographs corresponding to the modified clinoptilolites, CSW-NH₄, CSW-HFSi-0.1 and CSW-HFSi-0.4. In the reported micrographs was evidenced that the CSW zeolite shows secondary particles exhibiting diameters from 3 to 40 μm, formed by primary clinoptilolite crystallites showing a crystallite size, $\Phi = 40$ nm.

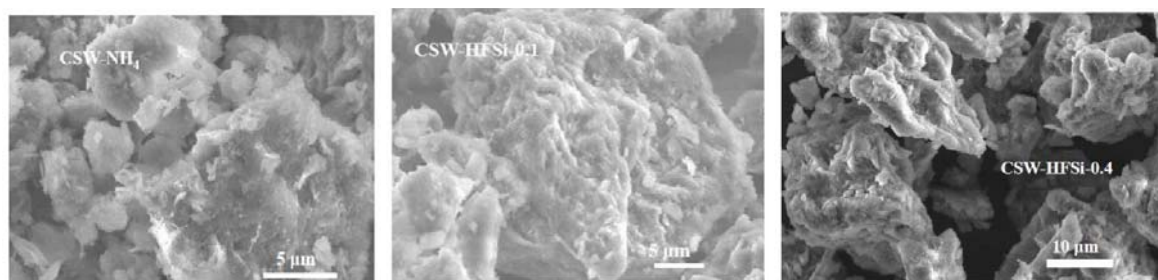


Fig. 6 SEM micrographs corresponding to the samples NH₄-CSW, CSW-HFSi-0.1 (bar = 5 μm) and CSW-HFSi-0.4 (bar = 10 μm).

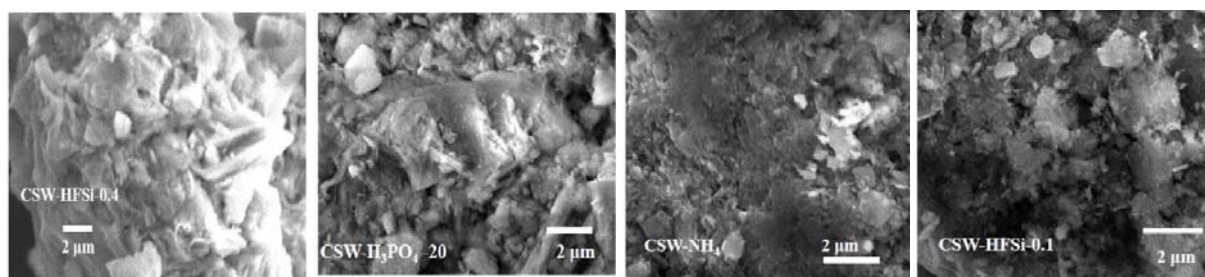


Fig. 7 SEM micrographs corresponding to the samples NH₄-CSW, CSW-HFSi-0.1, CSW-HFSi-0.4 and CSW-H₃PO₄-20 (bar = 2 μm).

Additionally, in Fig. 7 are displayed the SEM micrographs of the modified clinoptilolites: CSW-NH₄, CSW-HFSi-0.1, CSW-HFSi-0.4 and CSW-H₃PO₄-20 at higher magnification. These last micrographs evidenced the lath morphology of the primary clinoptilolite crystallites.

The elemental analysis of the clinoptilolite samples Na-CSW [21], Na-HC [17] and CSW-NH₄, CSW-HFSi-0.1, CSW-HFSi-0.4 and CSW-H₃PO₄-20 was determined by EDAX elemental analysis. These results are reported in Table 2. These results demonstrated that the exchange process replaced about 85% of the charge compensating ions, to be precise, the Na⁺, K⁺, Ca²⁺ and Mg²⁺ present in the natural material were exchanged by Na⁺ or in the produced homoinic clinoptilolites [17], to produce the Na-CSW and NH₄-CSW homoinic samples. In the case of the samples treated with orthophosphoric acid, together with the dealumination process the Na⁺, K⁺, Ca²⁺ and Mg²⁺ located in the micropores of the natural clinoptilolite were exchanged by protons [18]. In addition to the ion exchange was evidenced a slight increase in the Si/Al relation during the dealumination

Table 2 EDAX elemental analysis of the natural and modified samples in wt.%.

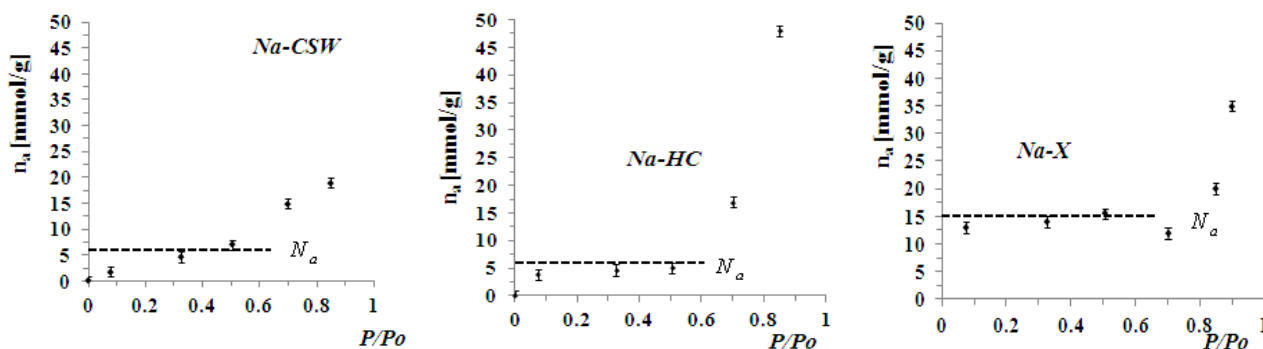
Sample	Si	Al	O	Na	K	Ca	Mg	Fe	Si/Al
Na-CSW	37.4	9.3	45.2	5.5	0.9	0	0.7	1.1	4.0
Na-HC	37.5	9.4	45.4	5.8	1.0	0	0.4	0.5	4.0
CSW-NH4	40.8	10.3	45.5	0.3	1	0	0.7	1.4	4.0
CSW-HFSi-0.1	41.4	9.6	46.3	0.1	0.9	0	0.3	1.0	4.3
CSW-HFSi-0.4	45.4	9.5	43.1	0.1	0.8	0	0.3	0.8	4.8
CSW-H3PO4-20	40.1	6.6	50.8	0.6	0.9	0	0.0	1.0	6.1

process. All this facts indicated a change in the zeolite chemistry that must be reflected in the adsorption properties of the modified clinoptilolites.

With the help of water adsorption, we studied the morphology of the tested clinoptilolites. Water vapor adsorption in a complex porous systems as natural zeolites occurs something like that [5, 10]: initially micropore filling, where the adsorption behavior is dominated nearly completely by the interactions of the adsorbate, and the pore wall; after that, at higher pressures, external surface coverage, consisting of monolayer, and multilayer adsorption on the walls of mesopores, and open macropores, and at last capillary condensation in the mesopores. In Fig. 8, are reported the water adsorption isotherms at 27 °C in Na-CSW, Na-HC and Na-X zeolites. During this adsorption process, water vapor at low pressures filled the micropores as was evidenced by the plateau in the following range of relative pressure: $0.2 < P/P_0 < 0.4$, at higher pressures $P/P_0 > 0.5$ the external surface was covered and finally near $P/P_0 = 1$ capillary condensation in the mesopores takes place. The previously described adsorption processes, indicated the existence of micropores, mesopores and

macropores [49], or simply a primary porosity, that is, the cavities and channels which constitute the zeolite framework and a secondary porosity describing the macroporosity and the mesoporosity developed between the zeolite crystals [8].

Fig. 9 is shown these DRIFT spectra, in the range between: $3,200\text{--}3,800\text{ cm}^{-1}$. Between, the bands present in the recorded DRIFTS spectra, the most important are the OH stretching vibrations related to the hydroxyl functionalities, specifically: silanol groups: Si-OH that is, terminal hydroxyl groups showing low acidity bridged hydroxyl groups: Si-OH-Al in which the proton shows Brönsted acid character and non-acidic extra-framework hydroxyl groups [50]. In the specific case of the DRIFTS spectrum corresponding to the ZSM-5, reported in Fig. 9, were evidenced three bands caused by the O-H stretching vibrations, to be precise: a band around: $3,590\text{ cm}^{-1}$ corresponding to the Brönsted acid sites, another band at $3,660\text{ cm}^{-1}$ related to extra-framework, Al-OH, that is: positively charged extra-framework aluminum, and a peak located at $3,740\text{ cm}^{-1}$ related to terminal silanol groups [26]. In the case of the modified clinoptilolites,

**Fig. 8** Adsorption isotherms of water at 27 °C on: Na-CSW, Na-HC and Na-X.

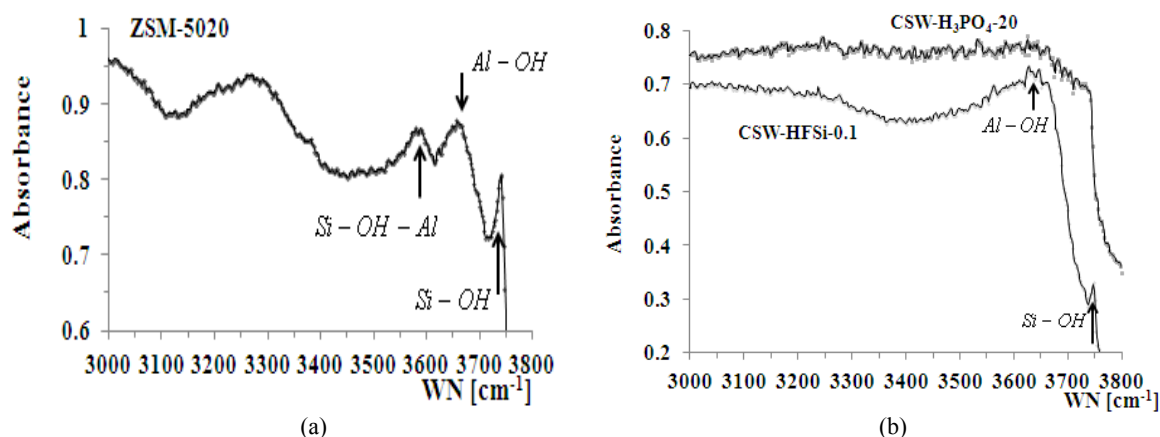


Fig. 9 DRIFTS spectra of the modified natural clinoptilolites: (a) CSW-HFSi-0.1 and CSW-H₃PO₄-20 and (b) the ZSM-5 (CBV-5020).

specifically, CSW-HFSi-0.1, a narrow band at about: 3,740 cm⁻¹ corresponding to terminal silanol groups (Si-OH) was evidenced; in the rest of the OH stretching vibration range, i.e., 3,000-3,700 cm⁻¹; was only evidenced a band 3,600-3,650 cm⁻¹ resulting from extra-framework Al-OH. The CSW-H₃PO₄-20 DRIFTS profile didn't show peaks in the range between: 3,200-3,800 cm⁻¹. The explanation that can be given to this profile should be related to dehydroxylation; since this process, in zeolites [6] and silica [51], produces the condensation of the OH groups. In the particular case of zeolites is generally accepted that during the process of dehydroxylation at temperatures up to 500 °C, bridged hydroxyls condenses to produce water and left behind the zeolite framework negatively charged [52], trigonal aluminum [53] and different types of positively charged extra-framework aluminum [54], at higher temperatures a dehydrogenation process is as well produced [55]. Thereafter, the modification process made to produce the sample CSW-HFSi-0.1 created a framework charged with positive and negative charges, where the charge compensating cations of the zeolite were removed, making available an open adsorption

space where adsorbed molecules are subjected to electrostatic interactions with the framework. This surface Chemistry is appropriate for adsorption, since this adsorption space is open. Besides, the electrostatic field, created by the negative and positive charge of the framework produces electrostatic interactions between the adsorbed molecule and the adsorbent.

Fig. 10 is reported the Dubinin plots of the adsorption isotherms of carbon dioxide at 0 °C on the modified zeolites CSW-HFSi-0.1 and CSW-HFSi-0.4. For comparison was as well reported the isotherm of CO₂ adsorption at 0 °C on the ZSM-5 (CBV-5020) zeolite [34]. The values of the micropore volume measured with the help of carbon dioxide adsorption, $W_{MP}^{CO_2}$, are reported in Table 3. This parameter was measured by fitting Eq. (1), with: $n = 2$, to the reported adsorption data (Fig. 10).

The precision of the measured micropore volumes is related to the excellent fitting of the adsorption data by the D-R isotherm equation, the appropriate relative pressure range tested ($0.00003 < P/P_0 < 0.03$) and the big amount of adsorption points produced during the adsorption test. All these facts allowed us to affirm that carbon adsorption took only

Table 3 Micropore volume and zeolitic phase amount calculated with the Dubinin Radushkevish isotherm equation.

Samples	N_a (mmol/g)	$W_{MP}^{CO_2}$ (cm ³ /g)	f (wt.%)
ZSM-5-3020	3.55 ± 0.01	0.169 ± 0.001	94
CSW-HFSi-0.1	3.13 ± 0.01	0.149 ± 0.001	93
CSW-HFSi-0.4	2.81 ± 0.01	0.134 ± 0.001	84

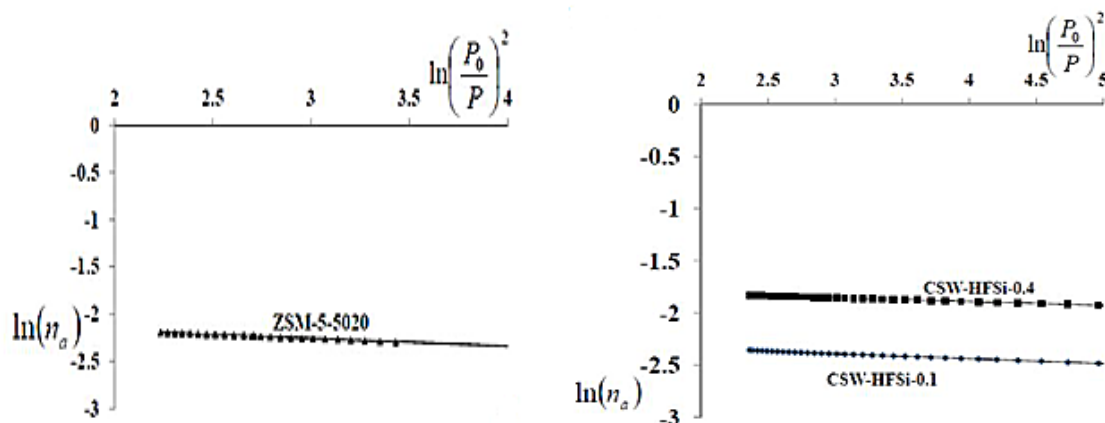


Fig. 10 Dubinin-Radushkevitch (D-R) plots of the adsorption isotherms of carbon dioxide at 0 °C on: CSW-HFSi-0.1, CSW-HFSi-0.4 and the ZSM-5 (CBV-5020).

place in the micropore region; consequently, the adsorption of carbon dioxide at 0 °C clearly evaluated the micropore volume of the studied zeolite samples.

With the help of the micropore volume, W_{MP} , of the zeolite present in the natural zeolite rock or in a bound form of a commercial zeolite and the micropore volume of the corresponding pure phase, W_{phase}^{pure} , of the same zeolite, we can determine the amount f , of zeolitic phases in wt.% (whenever it is the only zeolitic phase present), with the help of the equation: $f = W_{MP}^{CO_2} / W_{phase}^{pure}$. It is very well known that the micropore volume for pure clinoptilolite $W_{HEU} \approx 0.16 \text{ cm}^3/\text{g}$ [12] and the microporous volume of the MFI framework of pure H-ZSM-5 is $W_{MFI} \approx 0.18 \text{ cm}^3/\text{g}$ [58]. Subsequently, with the help of these data the amount f , of the zeolitic phase present in the modified clinoptilolites and the H-ZSM-5 used for comparison were calculated (Table 3). Further, the X-ray diffraction data (Figs. 1b and 1c) allowed the calculation of the phase composition of the modified clinoptilolites by means of standards [21] by applying a previously developed methodology [56, 57]. In the present case the standard was the sample $\text{NH}_4\text{-CSW}$.

Table 4 shows the results obtained applying this methodology. These results indicated that the modification increased the amount of clinoptilolite, in the case of the sample CSW-HFSi-0.1.

This was one of the aims of the treatments to produce an adsorbent comparable to commercial zeolites. However, in the case of samples CSW-HFSi-0.1 was observed a decrease in the amount of clinoptilolite in the sample and for the sample CSW- $\text{H}_3\text{PO}_4\text{-20}$ a big decrease (Figs. 1b and 1c). These results indicated that the increase in the concentration of $(\text{NH}_4)_6\text{SiF}_6$ and the treatment with orthophosphoric acid are not useful to achieve the proposed goals.

Is knowed in general, if a molecule contact the surface of a solid adsorbent, it become subjected to diverse interaction fields, such as: the dispersion energy, repulsion energy, polarization energy, field dipole energy, field gradient quadrupole energy, and as well some specific interactions, as the acid-base interaction, ϕ_{AB} , and the adsorbate-adsorbate interaction energy [59]. Dispersion and repulsion forces are present during physical adsorption in all adsorbents.

Table 4 Phase composition of the modified clinoptilolites.

Sample	Clinoptilolite (wt.%)	Others (wt.%)
CSW- NH_4	91 (5)	9 (5)
CSW-HFSi-0.1	95 (5)	5 (5)
CSW-HFSi-0.4	72 (5)	28 (5)
CSW- $\text{H}_3\text{PO}_4\text{-20}$	41 (5)	59 (5)

The electrostatic interactions between the adsorbed molecule and the adsorbent framework, depend on the structure and composition of the adsorbed molecule and the adsorbent itself [1-5]. That is, the interaction between the adsorbent and molecules with, for example, a noticeable quadrupolar moment, like the carbon dioxide molecule ($Q_{CO_2} = -4.3 \times 10^{-42} \text{ C}\cdot\text{m}^2$) give raise to specific interactions, where the combination of the dispersive and electrostatic attractive interactions are normally stronger than merely the dispersion interactions. In the case of interest here it is accepted that carbon dioxide interacts with surfaces through their dispersive and quadrupole moment interactions [1].

The parameters calculated with the D-R adsorption isotherm equation not only allowed us to evaluate the micropore volume of the sample, but also the adsorption interaction between the adsorbate and the adsorbent. To evaluate this interaction was used the characteristic energy of adsorption, calculated by fitting Eq. (1), with: $n = 2$, to the data reported in Fig. 10 (Table 3). The accuracy of the measured characteristic energy is related to the same arguments previously discussed for the micropore volume.

The quantitative evaluation of the interaction between carbon dioxide and the zeolite will be carried out with help of the isosteric heat of adsorption, q_{iso} [1-5]. In this regard, it is possible to calculate, q_{iso} , in an original way using only one isotherm as follows [42]:

$$q_{iso}(\theta) = -\Delta G + EF(T, \theta) \quad (2)$$

In which:

$$\Delta G = RT \ln \left(\frac{P}{P_0} \right)$$

and

$$F(T, \theta) = \frac{\alpha T}{2} (\ln[1/\theta])^{\left(\frac{1}{n}\right)-1} \quad (3)$$

where: $\theta = n_a/N_a$; $\alpha = -d\ln N_a/dT$ and E , and n , are the parameters of the Dubinin adsorption equation (in our case: $n = 2$, and E is reported in Table 5). It is also possible to assert that: $E = \Delta G(1/e)$, where: $\theta = 1/e$, in which, $e \approx 2.71828183$ is the base of the Napierian logarithm system. Now with the help of Eqs. (2) and (3), for $\theta = 1/e \approx 0.37$ is possible to get the following equation [34]:

$$q_{iso}(0.37) = -\Delta G(0.37) + EF(T, 0.37) = E[F(T, 0.37) - 1] \quad (4)$$

To calculate, $F(T, 0.37)$, with the help of Eq. (4) was used trustworthy experimental calorimetric data reported in literature, i.e, $q_{iso} = 22 \text{ kJ/mol}$ for the adsorption of carbon dioxide at 27°C in the range: $0.1 < n_a < 0.7 \text{ mmol/g}$ in MCM-41 [58] and the characteristic energy of adsorption, E , calculated by fitting Eq. (1), with: $n = 2$, to carbon dioxide adsorption on MCM-41 previously reported, $E = 19 \text{ kJ/mol}$ [34]. Consequently, it was possible to estimate that: $F(T, 0.37) \approx 2.16$. Thereafter, with the relation:

$$q_{iso}(0.37) = 1.16 E$$

were calculated the isosteric heat of adsorption (Table 5). The results reported indicated that the tested modified zeolites shows similar values for the measured isosteric heat of adsorption; but greater than those value of the isosteric heat of adsorption reported also in the present paper for the ZSM-5 zeolite, also larger than those reported for a particle packing silica and a dealuminated Y zeolite (DAY) [34], Cd, Zn and Ni-nitroprussides [41] and Cu-nitroprusside [40] and a Ni-MOF [39] (Table 6), as well bigger than experimental isosteric adsorption heats measured for the adsorption carbon dioxide on MCM-41- [58], silicalite [59], Na clinoptilolite

Table 5 Parameters calculated with the Dubinin-Radushkevish isotherm equation.

Sample	N_a (mmol/g)	$E_{CO_2}^{CO}$ (Kj/mol)	$q_{iso}^{CO_2}$ (Kj/mol)
ZSM-5-3020	3.55 ± 0.01	33 ± 1	38 ± 2
CSW-HFSi-0.1	3.13 ± 0.01	40 ± 1	46 ± 2
CSW-HFSi-0.4	2.81 ± 0.01	43 ± 1	50 ± 2

Table 6 Parameters Calculated with the Dubinin-Radushkevich Equation for a particle packing silica, Cd, Zn, Cu and Ni-nitroprussides (NPs), dealuminated Y zeolite (DAY) and a Ni MOF.

Sample	E^{CO_2} (KJ/mol)	$q_{\text{iso}}^{\text{CO}_2}$ (KJ/mol)	N_a (mmol/g)	$W_{\text{MP}}^{\text{CO}_2}$ (cm ³ /g)	Reference
P-68-Silica	24 ± 1	28 ± 1	3.57 ± 0.01	0.170 ± 0.001	Ref. [26]
Cd-NP	21 ± 1	25 ± 1	2.67 ± 0.01	0.127 ± 0.001	Ref. [33]
Cu-NP	20 ± 1	24 ± 1	3.23 ± 0.01	0.154 ± 0.001	Ref. [34]
DAY	17 ± 1	20 ± 1	6.93 ± 0.01	0.331 ± 0.001	Ref. [26]
Ni-MOF	16 ± 1	18 ± 1	1.68 ± 0.01	0.080 ± 0.01	Ref. [32]
Zn-NP	12 ± 1	14 ± 1	5.08 ± 0.01	0.242 ± 0.001	Ref. [33]
Ni-NP	9 ± 1	11 ± 1	5.78 ± 0.01	0.275 ± 0.001	Ref. [33]

and K-clinoptilolite [60], Na-A [61] and Na-X and MOF-5 [62] and MOF-508b [63], but similar to measured isosteric heats of adsorption for the adsorption of carbon dioxide on sodium ferrerite (Na-FER) [64].

The previously described adsorption data indicated that the interaction of the carbon dioxide molecule with the modified zeolites is strong. Subsequently, these materials could be very useful in gas separations. One of the causes of adsorption selectivity, are adsorption interactions. In this regard, the electrostatic interactions between the adsorbed molecule and the adsorbent framework, which depends on the structure and composition of the adsorbed molecule and the adsorbent itself, have an important role in adsorption selectivity. For example, for molecules such as: H₂O, H₂S, SO₂ and NH₃ with a high dipole moment and CO₂ a molecule with a high quadrupole moment, the electrostatic interactions are stronger than the dispersion plus repulsion interactions when are adsorbed in an aluminosilicate zeolite as the modified clinoptilolites. Dispersion and repulsion are forces present in all the adsorption couples. In the case of: H₂, Ar, CH₄, N₂ and O₂; given that, the dipole moments of these molecules is zero, the quadrupole moment is very low or absent, and the polarization effect will be only noticeable in the case of adsorbents with high electric fields, then dispersion forces are the only interaction present during the adsorption process of these gases. [5, 10, 12]. Thereafter, these gases are less strongly adsorbed in aluminosilicate zeolites and related materials than those showing electrostatic interactions. Consequently, the adsorption of H₂O, H₂S, SO₂ and NH₃ in aluminosilicate zeolites is very strong and those of

CO₂ relatively strong; then these zeolites will remove these gases selectively in mixtures with: H₂, Ar, CH₄, N₂ and O₂. These interactions are, as well, responsible for the high regeneration temperatures needed by zeolites to be applied; fact that oblige to spend a large quantity of energy for their regeneration.

As was above commented, the elemental chemical analysis of the modified clinoptilolites shown in table 2 indicated that ammonium exchanged about 90% of the charge compensating ions present in the natural zeolite. Thereafter, since the modified clinoptilolites CSW-HFSi-0.1 and CSW-HFSi-0.4 were further treated with (NH₄)₆SiF₆ and finally calcined, both zeolites were practically completely dehydroxylated producing a framework negatively and positively charged. The previously discussed energetic factor is very important for a precise description of the adsorption space. However, the geometrical factor is as well decisive. In this sense, the experimental evidence accumulated by us indicated that CSW natural clinoptilolite didn't adsorb nitrogen at 77 K. However, it adsorbs carbon dioxide at 0 °C. The structure of clinoptilolite, HEU framework type, show 3 channels; i.e., one 8-MR channel along [100], with an access of 2.6 × 4.7 (Å)²; two parallel channels along [001] one 8-MR with a window of access with 3.3 Å × 4.6 Å, and a 10-MR with an access of 3.0 Å ×

Table 7 Kinetic diameter (σ) of some gases [6, 67].

Gas	σ (Å)	Gas	σ (Å)
N ₂	3.64	H ₂ O	2.64
O ₂	3.46	N ₂ O	3.17
CO ₂	3.3	H ₂ S	3.4
CH ₄	3.76	NH ₃	3.1

7.6 Å [37]. Additionally, the kinetic diameter of: carbon dioxide is 3.4 Å and those of nitrogen 3.6 Å (Table 7) [6, 67]. We can conclude from the previous discussion that the effective access window of the modified clinoptilolite could be estimated to be around 3.5 Å, value that was as well reported by other authors [23]. This is an optimum value for the application of these modified clinoptilolites in bio-gas and natural gas cleaning, carbon dioxide recovery and gas drying. Since, the kinetic diameter of: water, hydrogen sulfide indicates that it can be fitted into the clinoptilolite pores, on the other hand those of oxygen and methane don't fit (Table 7).

Consequently, the modified clinoptilolites, like other microporous crystalline materials could be successfully applied for removing of H₂O, NH₃, NO₂, SO₂, SH₂, CO₂, and other impurities from gas streams.

4. Conclusions

In the research reported here was studied the structure, composition and morphology of modified clinoptilolites with, XRD, TGA, SEM-EDAX and gravimetric adsorption measurements. With the obtained data were calculated, the cell parameters, was measured the elemental and phase composition, studied the state of water and the morphology of the tested materials. The calculated cell parameters were similar to those reported for a typical clinoptilolite, but a variation of the values of these cell parameters during dealumination, was observed. To be precise, a small diminution of the cell volume was observed. The resolution of the TGA derivative profiles denoted the presence of two steps for water release. The first process was the desorption of physically adsorbed water from an energetically heterogeneous adsorbent as a zeolite and the second peak was related to the release of coordinated water. The water adsorption processes denoted the existence of micropores and mesopores in the CSW sample. The elemental analysis of the tested clinoptilolite samples determined with EDAX elemental

analysis demonstrated that the exchange process replaced about 85% of the original zeolite charge compensating ions, by Na⁺ or in the produced homoinic clinoptilolites. For the samples treated with orthophosphoric acid together with the dealumination process the Na⁺, K⁺, Ca²⁺ and Mg²⁺ located in the micropores of the natural clinoptilolite are exchanged by protons. Besides, it was evidenced a slight increase in the Si/Al relation during the dealumination process. As well, the CSW-HFSi samples were, practically, completely dehydroxylated during the modification treatment. All this facts indicated a change in the zeolite chemistry that must be reflected in the adsorption properties of the modified clinoptilolites. The surface chemistry of the modified clinoptilolites utilizing DRIFTS was studied. Besides, the interaction of carbon dioxide within the adsorption space of the modified clinoptilolites and two synthetic ZSM-5 zeolites were studied with the help of an automatic physisorption analyzer. Finally, an appropriate theoretical methodology for the analysis of the XRD and adsorption data was applied.

These results indicated that the modification process augmented the amount of clinoptilolite in the sample CSW-HFSi-0.1, but diminished it in the rest of the modified samples. The modification created an open adsorption space, since the charge compensating cations of the zeolite were removed. Additionally, a framework charged with positive and negative charges was produced in the samples treated with HFS. In this adsorption space, adsorbed molecules are subjected to strong electrostatic interactions with the framework. Additionally, the pore size of the obtained material only allow the adsorption of small molecules, subsequently these materials could be very useful in gas separations. Thereafter, the treatments produced adsorbents comparable to commercial zeolites.

The modification of clinoptilolite with HFSi to improve their adsorption properties had not been previously attempted.

Acknowledgments

The authors acknowledge the financial support provided by the US Department of Energy through the Massey Chair project at the University of Turabo. We also recognize the support of the National Science Foundation under the project CHE-0959334. We are also grateful to the Department of Mathematics and Physics of the University of Puerto Rico-Cayey Campus for the help provided during the SEM-EDAX analysis. As well we recognize the help provided by Mr. Carlos Muñiz, Mr. Raul Perez, and the Puerto Rico Energy Center in some of the SEM-EDAX tests.

References

- [1] R.M. Barrer, *Zeolites and Clay Minerals as Sorbents and Molecular Sieves*, Academic Press, London, 1978, p. 497.
- [2] D.M. Ruthven, *Principles of Adsorption and Adsorption Processes*; John Wiley and Sons, New York, 1984, p. 62.
- [3] F. Rouquerol, J. Rouquerol, K.S.W. Sing, *Adsorption by Powder Porous Solids*, Academic Press, New York, 1999, p. 93.
- [4] M. Thommes, *Nanoporous Materials: Science and Engineering*, Imperial College Press, London, 2004, p. 317.
- [5] R. Roque-Malherbe, *Adsorption and Diffusion in Nanoporous Materials*, Boca Raton, Florida, CRC Press, 2007, p. 57.
- [6] D.W. Breck, *Zeolite Molecular Sieves*, J. Wiley, and Sons, New York, 1974, p. 593.
- [7] R. Roque-Malherbe, A. Berazain, J.A. del Rosario, Calorimetric measurement of ion exchange heats in homioic heulandite and mordenite, *J. Thermal Anal.* 32 (1987) 949.
- [8] C.de las Pozas, R.L. Cordero, J.A. González-Morales, N. Travieso, R.R. Malherbe, A comparative study of MeAPO molecular sieves with AFI structure type Zeolites, *J. Mol. Catal.* 83 (1993) 145.
- [9] M. Fuentes, J. Magraner, C. de las Pozas, R.R. Malherbe J.P. Pariente, A. Corma, Cyclization of citronellal to isopulegol by zeolite catalysis, *App. Catal.* 47 (1989) 367.
- [10] C. de las Pozas, R.L. Cordero, C.D. Aguilar, M. Cora, R.R. Malherbe, Location and reducibility of Ni ions in HEU type zeolite, *J. Sol. State Chem.* 114 (1995) 108.
- [11] F.A. Mumpton, *Natural Zeolites, Occurrence, Properties, Use*, Pergamon Press, New York, 1978, p. 3.
- [12] G.V. Tsitsisvili, T.G. Andronikashvili, G.N. Kirov, L.D. Filizova, *Natural Zeolites*, Ellis Horwood, New York, 1992, p. 295.
- [13] R. Roque-Malherbe, *Handbook of Surfaces and Interfaces of Materials*, Volume 5, H. Academic Press, New York, 2001, p. 495.
- [14] R. Roque-Malherbe, *Physical Chemistry of Materials: Energy and Environmental Applications*, Boca Raton, Florida, CRC Press, 2009, p. 63.
- [15] R. Roque-Malherbe, L. Lemes, L. López-Colado, A. Montes, *Zeolites '93 Full Papers Volume*. International Committee on Natural Zeolites Press, Brockport, New York, 1995, p. 299.
- [16] R.R. Malherbe, Complementary Approach to the Volume Filling Theory of Adsorption, *Mic. Mes. Mat.* 41 (2000) 227.
- [17] R.R. Malherbe, W. del Valle, J. Ducongé, E. Toledo, Lead, cooper, cobalt and nickel removal from water solutions by dynamic ionic exchange in LECA zeolite beds, *Int. J. Env. & Pollution* 31 (2007) 292-303.
- [18] C. de las Pozas, W. Kolockiewics, R.R. Malherbe, Modification of clinoptilolite by orthophosphoric acid leaching, *Mic. Mat.* 5 (1996) 325.
- [19] R.R. Malherbe, M.H. Vélez, Foundations of thermoelectric analysis: Part 1. Cationic polarization, *J. Thermal Anal.* 36 (1990) 1025.
- [20] R.R. Malherbe, *Handbook of Surfaces and Interfaces of Materials*, Volume 2, Academic Press, New York, Chapter 13, 2001, p. 509.
- [21] R.R. Malherbe, R. Roque-Malherbe, W. del Valle, F. Marquez, J. Duconge, M.F.A. Goosen, Synthesis and characterization of zeolite based porous ceramic membranes, *Separation Sci. & Tech.* 41 (2006) 73.
- [22] M.H. Vélez, O. Raymond, A. Alvarado, A. Jacas, R.R. Malherbe, New materials obtained from high temperature phase transformations of natural zeolites, *J. Mater. Sci. Letters* 14 (1995) 1653.
- [23] S. Sircar, A.L. Myers, *Handbook of Zeolite Science and Technology*, Marcell Dekker Inc., New York, 2003, p. 1063.
- [24] G.H. Köhl, *Catalysis and Zeolites, Fundamentals and Applications*, Springer-Verlag, Berlin, 1999, p. 81.
- [25] N.C. Martinez, J.A. Dumesic, Applications of Adsorption Microcalorimetry to the Study of Heterogeneous Catalysis, *Adv. Catal.* 38 (1992) 149.
- [26] W.E. Farneth, R. Gorte, Method for characterizing zeolite acidity *Chem. Rev.* 95 (1995) 615.
- [27] H.G. Karge, M. Hunger, H.K. Beyer, *Catalysis and*

- Zeolites. Fundamentals and Applications, Springer-Verlag, Berlin, 1999, p. 198.
- [28] C. Li, Z. Wu, Handbook of Zeolite Science and Technology, Marcell Dekker Inc., New York, 2003, p. 423.
- [29] C. delas Pozas, C. Díaz-Aguila, E. Reguera-Ruiz, R. Roque-Malherbe, Mössbauer study of the hydrothermal transformation of clinoptilolite in faujasite, *J. Solid State Chem.* 93 (1991) 215.
- [30] L. Yang, K. Trafford, O. Kresnawahjuesa, J. Sepa, R. J. Gorte, D. White, An Examination of Confinement Effects in High-Silica Zeolites, *J. Phys. Chem. B*, 105 (2001) 1935.
- [31] R. Roque-Malherbe, F. Diaz-Castro, Calculation of the energy of adsorption of *n*-paraffins in nanoporous crystalline and ordered acid catalysts, and its relationship with the activation energy of the monomolecular catalytic cracking reaction, *J. Mol. Catal. A* 280 (2008) 194.
- [32] D.C. Amoros, J.A. Monge, M.A. de la Casa-Lillo, A.L. Solano, A CO₂ as an Adsorptive to characterize carbon molecular sieves and activated carbons, *Langmuir* 14 (1998) 4589.
- [33] C. Muñiz, J. Duconge, R. Roque-Malherbe, Paranitrophenol liquid-phase adsorption in dealuminated Y zeolite, *J. Coll. Int. Sci.* 329 (2009) 11-16.
- [34] R.R. Malherbe, R. Polanco, F.M. Linares, Study of the interaction between silica surfaces and the carbon dioxide molecule, *J. Phys. Chem. C* 114 (2010) 17773.
- [35] C. Knöfel, C. Martin, V. Hornebecq, P.L. Llewellyn, Study of carbon dioxide adsorption on mesoporous aminopropylsilane-functionalized silica and titania combining microcalorimetry and in situ infrared spectroscopy, *J. Phys. Chem. C* 113 (2009) 21726.
- [36] M.T. Ho, G.W. Allinson, D.E. Wiley, Reducing the Cost of CO₂ Capture from Flue Gases Using Pressure Swing Adsorption, *Ind. Eng. Chem. Res.* 47 (2008) 4883-4890.
- [37] S. Deng, Encyclopedia of Chemical Processing; Taylor and Francis: Boca Raton, FL, USA, 2006, p. 2825.
- [38] R.V. Siriwardane, M.S. Shen, E. P. Fisher, Adsorption of CO₂, N₂, and O₂ on Natural Zeolites, *Energy & Fuels* 17 (2003) 571.
- [39] A. Rios, C. Rivera, G. Garcia, C. Lozano, P. Fierro, L.F. Cobas et al., Synthesis, structure, adsorption space and magnetic properties of Ni-oxalate porous molecular magnet, *J. Mat. Sci. & Eng. A* 2 (2012) 284.
- [40] R.R. Malherbe, O.N.C. Uwakweh, C. Lozano, R. Polanco, A.H. Maldonado, P. Fierro, et al., Structural Effects and Interactions of Carbon Dioxide Molecules Adsorbed on Ni, Zn, and Cd Nitroprussides, *J. Phys. Chem. C* 115 (2011) 15555.
- [41] R.R. Malherbe, C. Lozano, R. Polanco, F. Marquez, F. Lugo, A.H. Maldonado et al., Study of carbon dioxide adsorption on a Cu nitroprusside polymorph, *J. Sol. State Chem.* 184 (2011) 1236.
- [42] B.P. Bering, M.M. Dubinin, V.V. Serpinskii, On thermodynamics of adsorption in micropores, *J. Coll. Int. Sci.* 38 (1972) 185-194.
- [43] M.M. Dubinin, Physical adsorption of gases and vapors in micropores, *Prog. Surf. Memb. Sci.* 9 (1975) 1.
- [44] C.H. Baerlocher, W.M. Meier, D.H. Olson, Atlas Zeolite Framework Type, 5th ed., Elsevier, Amsterdam, 2001, p. 156.
- [45] M.M. Treacy, J.B. Higgins (eds.), Collection of Simulated XRD Powder Patterns for Zeolites, Elsevier, Amsterdam, 2001, p. 186.
- [46] G.S. Pawley, Unit-cell refinement from powder diffraction scans, *J. Appl. Cryst.* 14 (1981) 357.
- [47] G.K. Williamson, X-ray line broaden-ingfromjiled aluminium and wolfram, W.H. Hall. *Acta Metallurgica* 1 (1953) 22-31.
- [48] R.D. Shannon, Revised effective ionic radii and systematic studies of interatomic distances in halides and chalcogenides, *Acta. Cryst. A* 32 (1976) 751.
- [49] K.S.W. Sing, D.H. Everett, R.A.W. Haul, L. Moscou, R.A. Pirotti, J. Rouquerol, et al., Reporting physisorption data for gas/solid systems with special reference to the determination of surface area and porosity, *Pure App. Chem.* 57 (1985) 603.
- [50] P. A. Jacobs, Acid zeolites: An attempt to develop unifying concept, *Catal. Rev. Sci. Eng.* 24 (1982) 415.
- [51] R. Mueller, H.K. Kammiller, K. Wegner, S.E. Pratsinis, OH surface density of SiO₂ and TiO₂ by thermogravimetric analysis, *Langmuir* 19 (2003) 160.
- [52] J.B. Uytterhoeven, L.G. Christner, W.K. Hall, Studies of the hydrogen held by solids: VIII. The decationated zeolites, *J. Phys. Chem.* 69 (1965) 2117.
- [53] J.A. van Bokhoven, A.M.J. van der Eerden, D.C. Koningsberger, Three-coordinate aluminum in zeolites observed with *in-situ* X-ray absorption near-edge spectroscopy at the Al K-edge: Flexibility of aluminum coordinations in zeolites, *J. Am. Chem. Soc.* 125 (2003) 7435.
- [54] G. Catana, D. Baetens, T. Mommaerts, R.A. Schoonheydt, B.M. Weckhuysen, Relating structure and chemical composition with lewis acidity in zeolites: A spectroscopic study with probe molecules, *J. Phys. Chem. B* 105 (2001) 4904.
- [55] M.J. Nash, A.M. Shough, D.W. Fickel, D.J. Doren, R.F. Lobo, High temperature dehydrogenation of bronsted acid sites in zeolites, *J. Am. Chem. Soc.* 130 (2008) 2460.
- [56] C. Gonzales, R.R. Malherbe, E.D. Shchukin, Theoretical principles for quantitative x-ray analysis in

- systems with high microabsorption, *J. Mater. Sci. Letters* 6 (1987) 604.
- [57] C. Gonzales, R.R. Malherbe, Optimization of quantitative X-ray phase analysis by Monte Carlo methods, *Acta Crystall. A* 43 (1987) 622
- [58] C. Kladis, S.K. Bhargava, K. Fogar, D.B. Akolekar, Effects of air pollutants on the cerium exchanged high silica zeolite catalyst: a Fourier transform infrared study, *J. Mol. Cat. A* 171 (2001) 243.
- [59] J.N. Israelachvili, *Intermolecular and Surface Forces* 3rd ed., Elsevier, Amsterdam, 2011, p. 9.
- [60] Y. He, N.A. Seaton, Heat of adsorption and adsorption heterogeneity for methane, ethane and carbon dioxide in MCM-41, *Langmuir* 2 (2006) 1150.
- [61] J.A. Dunne, M. Rao, S. Sircar, R.J. Gorte, A.L. Myers, Calorimetric heats of adsorption and adsorption isotherms: 2. O₂, N₂, Ar, CO₂, CH₄, C₂H₆, and SF₆ on NaX, H-ZSM-5, and Na-ZSM-5 zeolites, *Langmuir* 12 (1996) 5896.
- [62] S.U. Rege, R.T. Yang, M.A. Buzanowski, Sorbents for air, prepurification in air separation, *Chem. Eng. Sci.* 55 (2000) 4827.
- [63] A.R. Perez, G. Aguilar-Armenta, Adsorption kinetics and equilibria of carbon dioxide, ethylene, and ethane on 4A(CECA) zeolite, *J. Chem. Eng. Data* 55 (2010) 3625.
- [64] D. Saha, S. Deng, Adsorption equilibria and kinetics of carbon monoxide on zeolite 5A, 13X, MOF-5 and MOF-177, *J. Chem. Eng. Data* 54 (2009) 2245.
- [65] L. Bastin, P.S. Barcia, E.J. Hurtado, J.A.C. Silva, A.E. Rodrigues, B. A microporous metal-organic framework for separation of CO₂/N₂ and CO₂/CH₄ by fixed-bed adsorption, *Chen, J. Phys. Chem. C* 112 (2008) 1575.
- [66] A. Pulido, P. Nachtigall, A. Zukal, I. Domínguez, J. Cejka, Adsorption of CO₂ on sodium-exchanged ferrierites: The bridged CO₂ complexes formed between two extraframework cations, *J. Phys. Chem. C* 113 (2009) 2928.
- [67] R.W. Baker, *Membrane Technology and Applications* 2nd ed., J. Wiley and Sons, New York, 2004, p. 531.

Application of Two-Color LIF Thermometry to Nucleate Boiling

Nadine Kosseifi¹, Pascal Henry Biwolé², Christian Mathis², Germain Rousseaux³, Séverine Agnès Éliette Boyer⁴, Harunori Nakagawa Yoshikawa⁵ and Thierry Coupez¹

1. Center for Material Forming CEMEF, Mines ParisTech, UMR CNRS 7635, Sophia Antipolis 06904, France

2. Laboratory J.A. Dieudonné, University of Nice, Sophia Antipolis, UMR CNRS 6621, P arc Valrose, 06108 Nice, France

3. Axis HydEE, University of Poitiers, Department of Aerodynamics ISAE, ENSMA, UPR CNRS 3346, Institut P Prime, Futuroscope 86962, France

4. Physics and Mechanics of Materials Departement, University of Poitiers, ISAE-ENSMA-UPR CNRS 3346, Institut P Prime, Futuroscope 86961, France

5. Waves and complex Media Laboratory, University of Havre, UMR CNRS 6294, Havre76058, France

Received: January 31, 2013 / Accepted: February 27, 2013 / Published: May 25, 2013.

Abstract: The laser-induced fluorescence (LIF) thermometry is applied to measure the temperature field surrounding a single vapor bubble growing at an artificial nucleation site. In order to correct measurement errors due to the non-uniformity of the incident laser intensity, the two-color LIF thermometry technique is used in this nucleate boiling experiment. This technique is based on the use of two fluorescent dyes: the temperature sensitive dye Rhodamine B and the temperature insensitive dye Sulforhodamine-101. The concentration of the dyes is optimized by analyzing the behavior of fluorescence intensities. The mapping between the two images is determined through a geometrical calibration procedure. This technique presents a success in correcting the non uniformities due to the reflection of the light at the bubble surface and to the temperature gradient. The obtained temperature fields show that the two-color LIF is a promising technique in the investigation of nucleate boiling.

Key words: Two-color LIF thermometry, stereoscopic camera calibration, nucleate boiling.

Nomenclature

V_{α} :	Pixel values of camera α
V_{β} :	Pixel values of camera β
$c_{dye, 1}$ and $c_{dye, 2}$:	Concentrations of the first and second dye
$V_{\alpha, 0}$, $V_{\beta, 0}$:	Sensor offset values
I_0 :	Incident laser intensity
$u = (v, w)$:	Pixel intensity measured at pixel coordinates
f :	Dimensionless focal length
$[R_{ij}]$:	Rotation matrix
$[T_i]$:	Translation vector
(\tilde{V}, \tilde{W}) :	Pinhole projection
U :	Coordinate transformation
M :	Mapping from u_{β} to u_{α}

Greek letters

θ :	Temperature
θ_e :	Temperature of ethanol
θ_w :	Temperature of the wall
θ_{sat} :	The saturation temperature
λ :	Wavelength

1. Introduction

Comprehension of the vapor bubble behavior on a heated surface is primordial to understand the heat transfer during the boiling near the surface. The behavior of a growing bubble has been studied by different numerical methods [1-4]. To validate and improve these simulations, experimental data on both flow and thermal field around the bubble are

Corresponding author: Nadine Kosseifi, postdoctoral researcher in applied mathematics, research fields: two color LIF thermometry, numerical simulation, boiling and quenching. E-mail: Nadine.El_Kosseifi@mines-paristech.fr.

required [4, 5].

The laser-induced fluorescence (LIF) thermometry has been applied to several engineering problems, such as combustion studies [6] and heating and cooling system [7, 8]. This technique consists in temperature dependence of emission intensity of fluorescent dye molecules. These molecules are excited by a narrow spectrum of light and emit another spectrum of light with longer wavelengths due to the Stokes shift. The emission of the light source is separated by optical filters; the emission intensity distribution is imaged over an interest area by a digital camera. The sensor pixel values V reflects the temperature field.

First experimental LIF protocols used one single dye [9]. But during the recent years, different LIF techniques have been developed. Lavieille [10] presented a method where one single sensitive dye (Rhodamine B) is used with two or three separated color bands. When using one single dye with three spectral color bands, the advantage of this method is that the ratios of the emission of each band determine the temperature while correcting the effects of fluorescent re-absorption [11]; however this method is not suitable for evaporating problem [12]. Sakakibara [13] and Kim [14] described another LIF method, known as two-dyes LIF where two fluorescent dyes (temperature sensitive and temperature insensitive) are used with two synchronized cameras (camera α and camera β). When using this technique, the measurement errors due to the non-uniformity of the incident laser intensity are eliminated.

During boiling, a steep temperature gradient exists near the heating wall. This thermal gradient is accompanied by an optical index variation. The incident laser light is then nonuniform near the wall. Furthermore, the reflection of the light at vapor bubble surface also contributes to non-uniformity. Therefore, the use of two dyes is essential to avoid the measurement errors due to these non-uniformities and to get an accurate measurement of the temperature field in nucleate boiling problem. The two-color LIF

thermometry technique has been applied to the thermal transport at microscale [15], to the thermal plume [16] and to the plane impinging jet [17] but not to the nucleate boiling problem.

In the present work, a methodology to measure the temperature field around a vapor bubble by the two-color LIF thermometry is performed. This optical technique offers a non-intrusive temperature measurement with high spatial resolution, different from the pointwise measurement of thermocouples [18]. A brief review of the principle of two-color LIF thermometry is presented in Section 2. In Section 3, the experimental apparatus is introduced. It includes a heating system, a thermal control system and an optical system. The camera calibration procedure and the image mapping are then presented in Sections 4 and 5, respectively. After explaining the choice of the dyes' concentration and the temperature calibration in section 6, a measurement of temperature field surrounding a vapor bubble is presented and discussed. Conclusions with perspectives are given in the last section.

2. Principle of Two Color LIF Thermometry

The two color LIF technique consists in using two dyes, one temperature sensitive and the other insensitive. Two cameras are used, α and β , equipped with optical filters with different ranges of wavelength. The pixel values V_α and V_β corresponding to a physical point (x, y) of cameras α and β , respectively, are given by:

$$V_\alpha = (a_1(\theta)c_{dye,1} + a_2(\theta)c_{dye,2})I_0(x, y) + V_{\alpha,0} \quad (1)$$

$$V_\beta = (b_1(\theta)c_{dye,1} + b_2(\theta)c_{dye,2})I_0(x, y) + V_{\beta,0} \quad (2)$$

where, $c_{dye,1}$ and $c_{dye,2}$ are the concentrations of the first and second dyes, respectively. The constants $V_{\alpha,0}$ and $V_{\beta,0}$ are the sensor offset values. The coefficients a_1 , a_2 , b_1 and b_2 are functions of the temperature θ and of the optical configuration of the experimental setup. They are independent from the incident laser intensity I_0 . Taking the ratio of V_α and V_β after subtracting the offsets, an I_0 -independent function $F = F(\theta)$ is

obtained:

$$F(\theta) = \frac{V_\alpha - V_{\alpha,0}}{V_\beta - V_{\beta,0}} = \frac{a_1(\theta)c_{dye,1} + a_2(\theta)c_{dye,2}}{b_1(\theta)c_{dye,1} + b_2(\theta)c_{dye,2}} \quad (3)$$

Once this F -function is known, the temperature field can be given by:

$$\theta = F^{-1}\left(\frac{V_\alpha - V_{\alpha,0}}{V_\beta - V_{\beta,0}}\right) \quad (4)$$

A wide library of dyes exists in the literature. Natrajan & Christensen [15] reported success in combining Rhodamine B as a temperature sensitive dye with Sulforhodamine-101 as a temperature insensitive dye. In the present work, the same dyes are selected, Rhodamine B (RhB, Dye content 99%; VWR-France) and Sulforhodamine-101 (SR101, Dye content 95%; Sigma-Aldrich-USA), to measure the temperature in nucleate boiling problem. Since these experimental investigations are performed at a relatively high temperature (60-80 °C), the application of the two-color LIF thermometry technique is quite challenging because the dye fluorescence intensity must be visible at these temperatures.

3. Setup

A heating system similar to those developed by Siedel, et al. [19] and Kowaleski, et al. [20] was especially designed to generate isolated vapor bubbles. The designs of the optical cell, the longitudinal section of the heating element and the general view of the device are presented in Figs. 1a and 1b. Heat generated by a cartridge heater (6 mm in diameter and 48 mm in length) is transmitted to a horizontal circular copper disk through a copper stem. The copper disk is 20 mm in diameter and 0.2 mm in thickness. The temperature is monitored with four K-type thermocouples (chromel-alumel, Tc Direct-France) at distances, 17 mm, 12 mm, 7 mm and 2 mm from the disk (Fig. 1a). The temperature of the heater is controlled with the use of a PID. The bubbles are nucleated at an artificial cavity made at the center of the copper disk. The cavity has a mouth diameter of 0.2 mm.

The whole heating system is integrated to a vertically installed cylindrical glass container with the copper disk facing up. The container has an inner diameter of 50 mm and is filled partially by a test liquid (Fig. 1b). Ethanol (96% Vol; VWR-France) is chosen as the test liquid because of its low boiling temperature ($\theta = 78.4$ °C) at atmospheric pressure. Typical ethanol volume of 100 mL is considered. The container is immersed in an outer square tank $170 \times 170 \times 210$ mm³ which is filled by water circulating from and to a thermostatic bath. This tank serves to condition the ambient temperature and correct optical distortion due to the curvature of the cylindrical container. The temperature of ethanol, θ_e , and the temperature of water, θ_w , are monitored by K-type thermocouples. Fluctuation in these temperatures during an experiment is typically 0.1 °C. The difference $\theta_e - \theta_w$ is typically -0.3 °C without heating the copper disk and is around 1 °C when heating it.

The illumination source is a double cavity Nd:YAG laser from Litron Laser with a pulse energy about 100 mJ per pulse during 8 ns and a wavelength of 532 nm. The dyes are excited by a 0.5 mm-thick vertical laser sheet that passes exactly over the artificial cavity (Fig. 1b). In the current paper, the mean thermal field is obtained over a small area near the bubble. The fluorescence of each dye is separated by a dichroic filter with a transition wavelength $\lambda = 600$ nm, size $(50 \times 50 \times 2)$ mm³. The fluorescence signal of each dye is captured by two identical CCD cameras (Image Pro X from Lavision) recording images at 14 Hz. These cameras, camera α and camera β , are both equipped with filters (size of 50 mm diameter). A band-pass filter of $550 \text{ nm} < \lambda < 580 \text{ nm}$ is fixed on camera α to observe the emission of RhB and a long-pass filter of $\lambda > 665 \text{ nm}$ is fixed on camera β to observe the emission of SR101. All filters are provided by Chroma Technology Corp, USA. The focal length of the lens is 200 mm, a shorter focal length can not be used because of the equipment size.

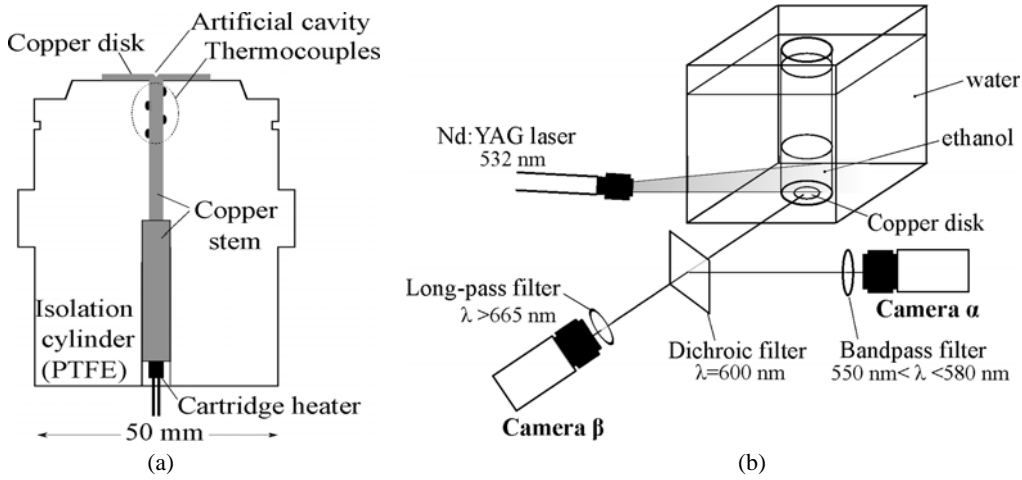


Fig. 1 Details of the developed experimental setup. (a) Longitudinal section of the heating element and (b) device configuration.

4. Camera Calibration

In the two-color LIF thermometry, the pixel intensity measured at pixel coordinates $u_\alpha = (v_\alpha, w_\alpha)$ on a camera α 's image is divided by the pixel intensity at $u_\beta = (v_\beta, w_\beta)$ on a camera β 's image (Eq. (3)). This division is performed for all pairs of u_α and u_β that point to the same physical point. The mapping from u_β to u_α (or, inverse) should be known accurately. This mapping is determined through a geometrical camera calibration procedure, which gives intrinsic and extrinsic parameters of both cameras.

The calibration is performed with the camera Calibration Toolbox for Matlab [21], which does not require a full 3D calibration object but a 2D planar checkerboard, moved on several locations. The adopted estimations for planar homographies and for maximum likelihood are those in Ref. [22]. The closed-form estimation of camera intrinsic parameters uses explicitly the orthogonality of vanishing points. Tangential distortion coefficients are also taken into account by following the camera model in Ref. [23]. The outputs of the calibration include: dimensionless focal lengths f_1 and f_2 measured in the horizontal and vertical sizes of a sensor element, respectively; the skew coefficients k_1 , k_2 and k_5 represent the image radial distortion and k_3 , k_4 represent the tangential one; the rotation matrix $|R_{ij}|$ and translation vector $[T_i]$

give the transformation from a real world coordinate system to a 3D camera's coordinate system. In our application, the plane $Z = 0$ is considered coincident with the plane of the laser sheet. The calibration target is a checkerboard patterns with squares of 2 mm.

The spatial resolution is 0.026 mm/pix for camera α 's image and 0.024 mm/pix for camera β 's image. By comparing the image of camera α to the mapped image of camera β , the accuracy of the mapping is estimated to 0.05 mm.

5. Image Mapping

For a given real world coordinates $(X, Y, 0)$ on the laser sheet, the coordinates (x, y, z) in a camera's reference frame [23] are:

$$\begin{bmatrix} x \\ y \\ z \end{bmatrix} = \begin{bmatrix} R_{11} & R_{12} & R_{13} \\ R_{21} & R_{22} & R_{23} \\ R_{31} & R_{32} & R_{33} \end{bmatrix} \begin{bmatrix} X \\ Y \\ 0 \end{bmatrix} + \begin{bmatrix} T_1 \\ T_2 \\ T_3 \end{bmatrix} \quad (5)$$

The pinhole projection (\tilde{v}, \tilde{w}) of this point on the camera's image plane reads:

$$\tilde{v} = \frac{x}{z} = \frac{R_{11}X + R_{12}Y + T_1}{R_{31}X + R_{32}Y + T_3} \quad (6)$$

$$\tilde{w} = \frac{y}{z} = \frac{R_{21}X + R_{22}Y + T_2}{R_{31}X + R_{32}Y + T_3} \quad (7)$$

where Eq. (5) has been substituted. The distorted

coordinates, which are expected to be the pixel coordinates of (v, w) on a captured image, are then given by:

$$v = f_1 \left[\tilde{v} \left(1 + k_1 \tilde{r}^2 + k_2 \tilde{r}^4 + k_5 \tilde{r}^6 \right) + 2k_3 \tilde{v} \tilde{w} + k_4 \left(\tilde{r}^2 + 2\tilde{v}^2 \right) \right] + v_0 \quad (8)$$

$$w = f_2 \left[\tilde{w} \left(1 + k_1 \tilde{r}^2 + k_2 \tilde{r}^4 + k_5 \tilde{r}^6 \right) + k_3 \left(\tilde{r}^2 + 2\tilde{w}^2 \right) + 2k_4 \tilde{v} \tilde{w} \right] + w_0 \quad (9)$$

where, (v_0, w_0) are the coordinates of the principal point and $\tilde{r} = \sqrt{\tilde{v}^2 + \tilde{w}^2}$.

For each camera, applications of Eqs. (5)-(9) define a coordinate transformation U : $u = U(X, Y)$ from real world coordinates to pixel coordinates. The mapping M from u_β to u_α is determined by combining U and its inverse U^{-1} . The inverse transformation U^{-1} is found as follows:

(1) The coordinates $\tilde{v}(u)$ and $\tilde{w}(u)$ are obtained by inverting Eqs. (8)-(9);

(2) The real world coordinates are obtained by substituting \tilde{v} and \tilde{w} in Eqs. (6)-(7).

Applying the obtained U^{-1} to camera β , the real world coordinates corresponds to $(X, Y)U^{-1}(U_\beta)$. The pixel coordinates u_α viewing the same point is given by $u_\alpha = U(X, Y)$. Hence, u_α and u_β are related by the relationship $u_\alpha = U(U^{-1}(u_\beta))$. The mapping M is obtained by computing u_α for all the pixel points u_β belonging to the image region of interest.

6. Concentration Optimization and Temperature Calibration

The coefficients of the concentrations in Eq. (3) depend on the parameters of the optical system. In order to decide an optimal combination of the two concentrations c_{RhB} and c_{SR101} , respectively, an analyze of the cameras output voltages responses as a function of the dyes' concentrations is achieved.

Fig. 2 presents averaged intensities V_α and V_β for different values of c_{RhB} . The solution does not contain SR101. The averaging is performed over an area of (230×630) pix² above the copper disk. The intensity V_α increases linearly with the concentration until $c_{RhB} =$

0.5 mg/L. A decrease seen for $c_{RhB} > 1$ mg/L might be explained by the absorption of the emitted light over the optical path in the solution. The intensity V_β is much lower than V_α , as expected (Fig. 2).

Fig. 3 presents results of a similar experiment obtained by varying c_{SR101} and without adding any RhB to the solution. At low concentrations, both intensities are of the same order of magnitude and behave linearly until $c_{SR101} = 0.5$ mg/L. Distinction of these intensities becomes significant for $c_{SR101} > 1$ mg/L.

A simple application of the two-color LIF thermometry requires linear behavior to V_α and V_β . Therefore, both concentrations should be lower than 0.4 mg/L. Moreover to get accurate results, the measured intensities should be larger than the level of the noise produced by the cameras' sensors. Our

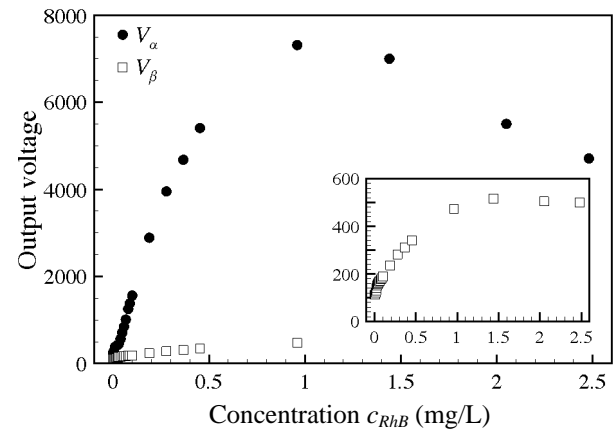


Fig. 2 camera pixel intensities V_α and V_β for different concentrations of RhB in ethanol at $\theta_e = 40^\circ\text{C}$.

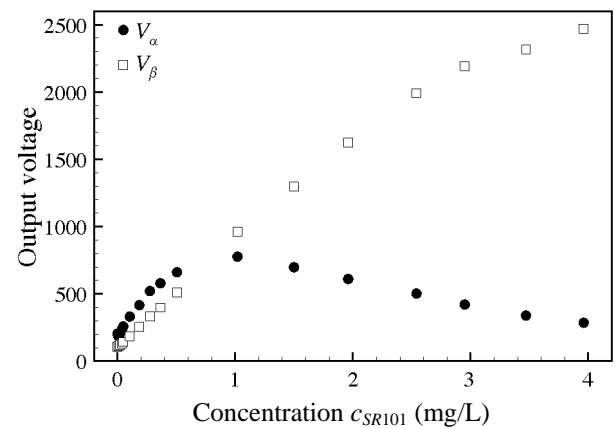


Fig. 3 Camera pixel intensities V_α and V_β for different concentrations of SR101 in ethanol at $\theta_e = 40^\circ\text{C}$.

cameras' sensors have the same offset $V_\alpha = V_\beta = 101$ with a Gaussian noise centered around 30. In the purpose to maximize the sensitivity of the F -function to the temperature ($\partial F / \partial \theta$) and to respect the above requirements, these concentrations $c_{RhB} = 0.1$ mg/L and $c_{SR101} = 0.1$ mg/L have been considered in the following work.

The intensities V_α and V_β observed for these concentrations are shown in Fig. 4 for a temperature range $30^\circ\text{C} < \theta < 74^\circ\text{C}$, in intervals of 5°C . The values of the intensities are normalized by their values at 40°C (1,415 and 423 for cameras α and β , respectively). It can be noted that both dyes remain visible at the ethanol boiling temperature ($\theta_{sat} = 78.4^\circ\text{C}$). Thus both dyes are well suited to be used in nucleate boiling investigation. The intensity V_α decreases by $0.7\%/^\circ\text{C}$, while V_β decreases with a smaller rate $0.2\%/^\circ\text{C}$. By comparing Figs. 2 and 3, one can notice that the observed fluorescence of RhB is higher than that of SR101. As it can be observed in Fig. 2, the RhB emission is not effectively blocked by the filters of camera β . For these reasons the output voltage V_β is significantly influenced by the RhB emission and the decrease in the intensity of camera β , presented in Fig. 4, is then due to the contribution of the RhB fluorescence to V_β . Measurement error due to the sensor noise, associated to camera β and camera α at $\theta_e = 40^\circ\text{C}$, are estimated as $30/423$ and $30/1415$, i.e., 7% and 2%, respectively.

Fig. 5 shows the result of the temperature calibration for this solution, where $V_{\alpha,0}$ and $V_{\beta,0}$ represent the offsets values (Eq. (3)). For computing θ from a given value of F , this linear relation is adopted:

$$\theta = -59.5F + 265.0 \text{ (}^\circ\text{C)} \quad (10)$$

The sensitivity of the F -function to the temperature is $-0.5\%/^\circ\text{C}$. The standard deviation of the temperature data from the calibration (Eq. (10)) is 1.4°C . Once this calibration is made the re-absorption of the RhB emissions along the imaging path will be taken into account by the system itself.

7. Results and Discussion

Fig. 6 shows images of a vapor bubble. The view of camera β has already been mapped onto the image plane of camera α . The bubble has a diameter of around 1 mm and grows at the artificial nucleation site in ethanol of $\theta_e = 40^\circ\text{C}$ (i.e., the subcooling $\Delta\theta_{sub} = \theta_e - \theta_{sat} = 17.2^\circ\text{C}$). In Fig. 6a, hot plumes rising from the disk surface and from the bubble are seen as darker zones, while these hot plumes are not distinguished in Fig. 6b. In both images, a dark band at the right of the bubble (bubble's shadow) and a luminous contour above the bubble can be noticed as presented in Fig. 7. Since the laser sheet enters the

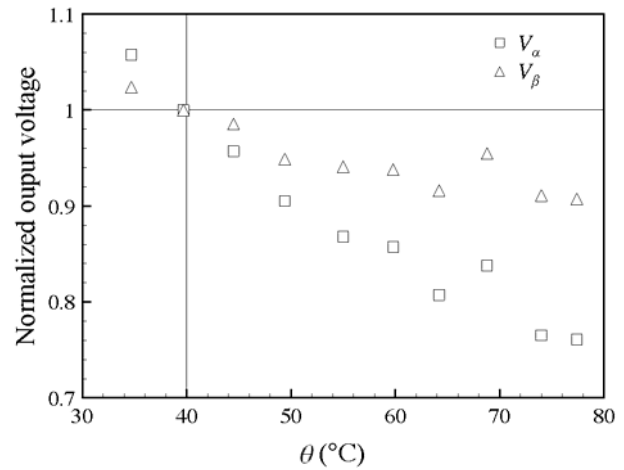


Fig. 4 Normalized pixel intensities for a RhB-SR101/ethanol solution of $c_{RhB} = 0.1$ mg/L and $c_{SR101} = 0.4$ mg/L.

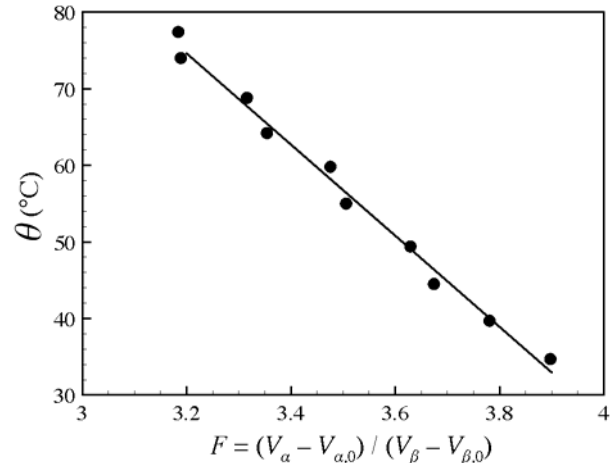


Fig. 5 Temperature calibration for a RhB-SR/ethanol solution of $c_{RhB} = 0.1$ mg/L and $c_{SR101} = 0.4$ mg/L. The temperature varies linearly as a function of F (Eq. (10)).

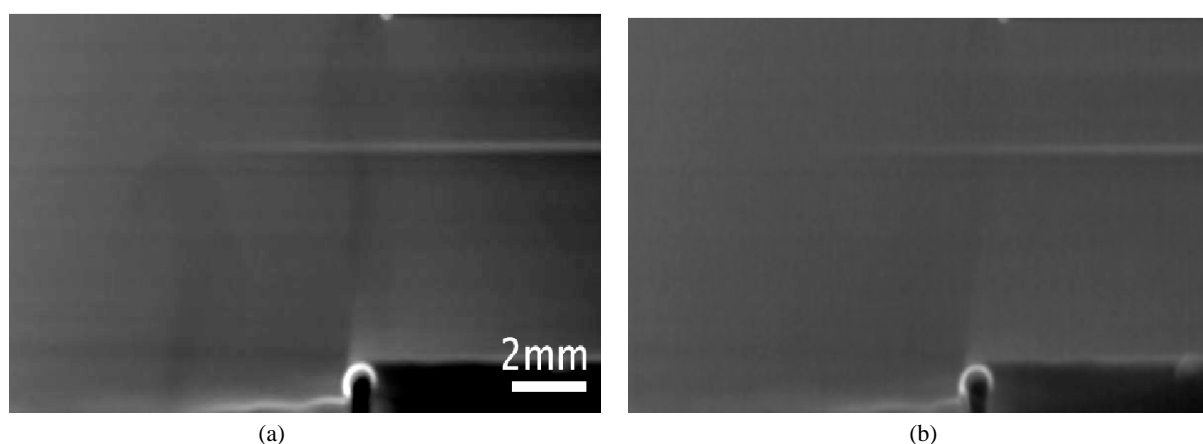


Fig. 6 A vapor bubble growing on an artificial nucleation site in ethanol at $\theta_e = 61.2$ °C. (a) view of camera α and (b) view of camera β .

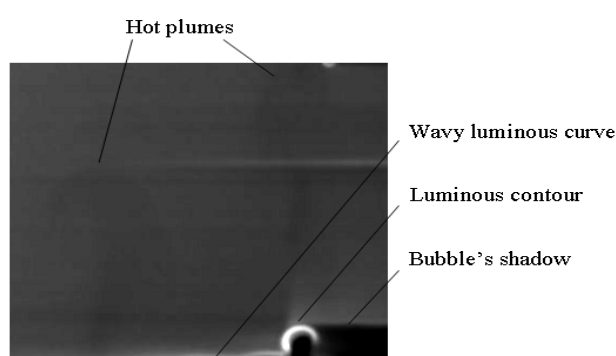


Fig. 7 Close up on the bubble vicinity of Fig. 6a.

measurement area from the left to the right (Fig. 1b), then the bubble's shadow appears in both Figs. 6a and 6b. The luminous contour above the bubble is due to the laser reflection at the bubble surface.

Furthermore, horizontal luminous and dark lines, results of optical imperfection of the setup are also seen in both images. Roughness on the inner and outer tanks' lateral walls can produce such inhomogeneity.

Local fluctuation of θ_e and θ_w could also lead to non-uniform lighting. These non-uniformities are inevitable or difficult to remove in boiling experiments.

The use of a single-color LIF thermometry may give erroneous thermal field and the use of the two color LIF thermometry technique is recommended.

Fig. 8 shows a temperature field at different time steps, it was determined by calculating and converting the F-function. The conversion was achieved by the temperature calibration (Eq. (10)). The ethanol

spinodal limit is 164 °C [24], to better illustrate the temperature field the zones with unphysical temperatures (either lower than 50 °C or higher than 100 °C) are uncolored. At the right of the bubble (shadow zone), the temperature is not determined due to the low intensities of the dyes. Other uncolored zones are found above the copper disk along the wavy luminous curve seen in Fig. 7. These uncolored zones can be due to the insufficient accuracy of the mapping. In fact, the error of our mapping (0.05 mm) is equivalent to half the thickness of the wavy curve. In order to eliminate lighting non-uniformity of such a meso scale, more accuracy mapping would be required.

Except those small zones, the temperature field is successfully obtained over the whole interest area. The bulk liquid temperature is around 60 °C and it is in good agreement with the thermocouples' measurements. The hot plumes are seen as higher temperature zones of 70-73 °C. The luminous contour above the bubble due to the reflection of the light at the bubble surface is successfully corrected. The success in correcting these non-uniformities and in measuring the temperature underlines the significance of the two-color LIF thermometry in boiling experiments.

8. Summary and Perspectives

A novel application method of the two-color LIF

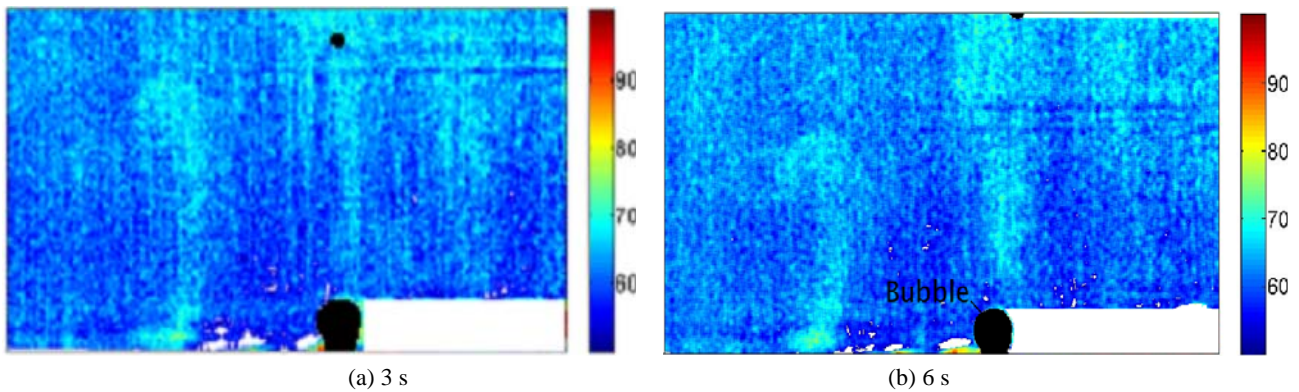


Fig. 8 Temperature field in the vicinity of a vapour bubble growing on an artificial nucleation site in ethanol of $\theta_e = 6.12$ °C, (a) 3 s and (b) 6 s.

thermometry to nucleate boiling investigation is presented. The camera calibration procedure with an accurate image mapping between the two cameras is required for calculating the F -function (Eq. (3)). Two dyes are used, the Rhodamine B and the Sulforhodamine-101, respectively. The optimization of both dyes' concentrations is discussed by observing the fluorescence intensity in ethanol at $\theta_e = 40$ °C within a wide range of concentration up to 4 mg/L (Figs. 2 and 3). The temperature calibration (Eq. (10)) for a solution of 0.1 mg/L of Rhodamine B and 0.4 mg/L of Sulforhodamine-101 shows a sensitivity of $-0.5\%/^{\circ}\text{C}$ for the F -function. This sensitivity is comparable with the sensitivity obtained by Natrajan & Christensen [15] over the temperature range 10 °C $< \theta < 44$ °C ($-1.5\%/^{\circ}\text{C}$).

The temperature field around a vapor bubble in nucleate boiling is successfully obtained with corrections to inevitable inhomogeneous lighting associated with the temperature gradient and the reflection at the bubble surface. This result suggests that the two color LIF thermometry is a promising method for measuring the thermal field in boiling.

To improve the temperature correction, an accurate two-camera image mapping is necessary. This improvement can be performed by increasing the optical magnification. The temperature sensitivity of the F -function can be also improved by optimizing the configuration of optical elements and the dyes'

concentrations. The thickness of the laser sheet is of the same order as the bubble radius, therefore, on going work consists in increasing the bubble size.

At the current stage, the application of two color LIF technique should not be limited to the case studied herein. In an additional future work, this new experimental investigation should be used to validate the numerical approach, based on finite element method (FEM) and computational fluid dynamic (CFD) [25, 26]. This new experimentation would be also used to optimize the heat transfer due to boiling in industrial quenching process [4]. A great advantage should be realized by synchronizing the two-color laser-induced fluorescent thermometry (LIF) with the particle image velocimetry (PIV) [27, 28], to acquire a two-dimensional map of both the temperature and the velocity fields during nucleate boiling.

Acknowledgments

The authors present their acknowledgments to the companies involved in the THOST (Thermal Optimisation System) project managed by Science Computer and Consultants (SCC). The authors are also sincerely grateful to Lionel Freire and Francis Fournier for the help provided during the experimental work and to the student Victor Fronzi for his contribution in the experimental investigations.

References

- [1] A.J. Robinson, R.L. Judd, Bubble growth in a uniform and spatially distributed temperature field, *International Journal of Heat and Mass Transfer* 44 (2001) 2699-2710.
- [2] Y. Chen, M. Groll, Dynamics and shape of bubbles on heating surfaces: A simulation study, *International Journal of Heat and Mass Transfer* 49 (2006) 1115-1128.
- [3] Y. Fujita, Q. Bai, Numerical simulation of the growth of an isolated bubble in nucleate boiling, in: 11th International Heat Transfer Conference, 1998, pp. 422-437.
- [4] N. Kosseifi, Numerical Simulation of Boiling for Industrial Quenching Processes, Ph.D. Thesis, Ecole Nationale Supérieure des Mines de Paris, CEMEF, France, 2012.
- [5] T.A. Kowalewski, J. Pakleza, R. Trzcinski, A. Zachara, Experimental analysis of vapour bubble growing on a heated surface, *Archives of Thermodynamics* 25 (2004) 1-12.
- [6] N. Omenetto, P. Benetti, G. Rossi, Flame temperature measurements by means of atomic fluorescence spectrometry, *Spectrochimica Acta Part B: Atomic Spectroscopy* 27 (1972) 453-461.
- [7] L. Shi, X. Mao, A.J. Jaworski, Application of planar laser-induced fluorescence measurement techniques to study the heat transfer characteristics of parallel-plate heat exchangers in thermoacoustic devices, *Measurement Science and Technology* 21 (2010) 115405-115421.
- [8] F. Guillard, R. Fritzson, J. Revstedt, C. Tragårdh, M. Aldén, L. Fuchs, Mixing in a confined turbulent impinging jet using planar laser-induced fluorescence, *Experiments in Fluids* 25 (1998) 143-150.
- [9] D. Ross, M. Gaitan, L.E. Locascio, Temperature measurement in microfluidic systems using a temperature-dependent fluorescent dye, *Anal. Chem.* 73 (2001) 4117-4123.
- [10] P. Lavieille, A. Delconte, D. Blondel, M. Lebouché, F. Lemoine, Non-intrusive temperature measurements using three color laser induced fluorescence, *Experiments in Fluids* 36 (2004) 706-716.
- [11] A. Petracci, R. Delfos, J. Westerweel, Combined piv/lif measurements in a rayleigh-bnard convection cell, in: 13th International Symposium on Applications of Laser Techniques to Fluid Mechanics, Lisbon 2006, paper 1221, http://ltces.dem.ist.utl.pt/lxaser/lxaser2006/downloads/papers/18_3.pdf.
- [12] P. Lavieille, F. Lemoine, G. Lavergne, M. Lebouché, Evaporating and combusting droplet temperature measurements using two-color laser-induced fluorescence, *Experiments in Fluids* 31 (2001) 45-55.
- [13] J. Sakakibara, R.J. Adrian, Whole field measurement of temperature in water using two-color laser induced fluorescence, *Experiments in Fluids* 26 (1999) 7-15.
- [14] H.J. Kim, K.D. Kihm, J.S. Allen, Examination of ratiometric laser induced fluorescence thermometry for microscale spatial measurement resolution, *Heat and Mass Transfer* 46 (2003) 3967-3974.
- [15] V.K. Natrajan, K.T. Christensen, Two-color laser-induced fluorescent thermometry for microfluidic systems, *Measurement Science and Technology* 20 (2009) 015401-015412.
- [16] J. Coppeta C. Rogers, Dual emission laser induced fluorescence for direct planar scalar behavior measurements, *Experiments in Fluids* 25 (1998) 1-15.
- [17] K. Hishida, J. Sakakibara, Combined planar laser-induced fluorescence particle image velocimetry technique for velocity and temperature fields, *Experiments in Fluids* 29 (2001) 129-140.
- [18] W. Gabler, R. Honig, R. Lachner, F. Mayinger, G. Kappler, Spectroscopic techniques for ram-combustors, in: *Proceeding of 2nd Space Course*, Munich, 1993, pp. 1-60.
- [19] S. Siedel, S. Cioulachtjian, J. Bonjour, Experimental analysis of bubble growth, departure and interactions during pool boiling on artificial nucleation sites, *Experimental Thermal and Fluid Science* 32 (2008) 1504-1511.
- [20] T.A. Kowalewski, J. Pakleza, A. Cybulski, Particle image velocimetry for vapour bubble growth analysis, In *Proc. 8th International Conference Laser Anemometry Advanced and Applications*, Rome, 1999, pp. 243-250.
- [21] J.Y. Bouguet, Camera calibration toolbox for matlab, Home Page, <http://www.vision.caltech.edu/bouguetj/calibdoc/>, (accessed 2010).
- [22] Z. Zhang, Flexible camera calibration by viewing a plane from unknown orientations, in: *Proc. International Conference on Computer Vision*, Corfu, Greece, 1999.
- [23] J. Heikkila, O. Silvén, A four-step camera calibration procedure with implicit image correction, in: *Proc. IEEE Computer Society Conference on Computer Vision and Pattern Recognition*, San Juan, Puerto Rico, 1997, pp. 1106-1112.
- [24] V.P. Carey, *Liquid-Vapor Phase-Change Phenomena*, Taylor & Francis, Bristol, PA, 1992, pp. 158-163.
- [25] E. Hachem, H. Dignonnet, N. Kosseifi, E. Massoni, T.

- Coupez, Enriched finite element spaces for transient conduction heat transfer, *Applied Mathematics and Computation* 217 (2010) 3929-3943.
- [26] N. Kosseifi, E. Hachem, L. Silva, S.A.E. Boyer, E. Massoni, T. Coupez, Numerical simulation of boiling during the quenching process, 10^{ème} colloque national en calcul des structures, <http://hal.archives-ouvertes.fr/hal-00592676/fr/>, Giens, France. (accessed 2011).
- [27] T.R. Meyer, G.J. Fiechtner, S.P. Gogineni, J.C. Rolon, C.D. Carter, J.R. Gord, Simultaneous plif/piv investigation of vortex-induced annular extinction in h₂-air counter flow diffusion flames, *Experiments in Fluids* 36 (2004) 259-267.
- [28] B.J. Balakumar, G.C. Orlicz, C.D. Tomkins, K.P. Prestridge, Simultaneous particle-image velocimetryplanar laser induced fluorescence measurements of Richtmyer-Meshkov instability growth in a gas curtain with and without reshock, *Physics of Fluids* 20 (2008) 124103-124116.

Effect of the Al_2O_3 and BaO Addition on the Thermal and Physical Properties of Ternary Glass System (B_2O_3 -BaO- Al_2O_3)

Djamila Aboutaleb, Brahim Safi, Azzeddine Ayadi and Aicha Iratni

Research Unit Materials, Processes and Environment, Faculty of Science Engineer, Boumerdes University, Boumerdes 35000, Algeria

Received: September 21, 2012 / Accepted: October 28, 2012 / Published: May 25, 2013.

Abstract: In borate glasses, the main structural units are the $[\text{BO}_3]$ triangles and $[\text{BO}_4]$ tetradral which form different superstructural units like; boroxol rings, metaborate rings and chains, pentaborate, diborate, triborate and pyroborate. In this work, the Barium aluminoborate glasses were prepared. Some of properties were investigated by measure like density and chemical durability and the other by calculs. The dilatometric curves were determined and they revealed that the temperature of transition (T_g) and softening (T_s) and the dilatation coefficient increase by addition of Al_2O_3 and BaO content.

Key words: Barium aluminoborate glass, density, chemical durability, dilatometric curves.

Nomenclature

α :	Thermal dilation coefficient, $10^{-6}, \text{K}^{-1}$
n_d :	Index of refraction
d :	Optical dispersion
E :	Longitudinal modulus of elasticity, kbar
σ :	Surface tension $10^{-3}, \text{N/m}$
ρ :	Densities, $\text{g}\cdot\text{cm}^{-3}$
σ :	Compressive stress (σ_c) or with traction (σ_t), MN/m^2
C_p :	Heat capacity, J/gK
λ_c :	Thermal conductivity, W/mK
ϵ :	Electric permittivity

1. Introduction

In special glass systems, the chemical composition plays an important role in determining properties of the glass. The components of glass are distributed into three categories: network formers, network modifiers and intermediate species, which falls somewhere between network formers and modifiers

and may substitute for a network former in the glassy state. The higher valence cations such as Al^{3+} are commonly used as intermediate species [1]. In borate glasses, the main structural units are the $[\text{BO}_3]$ triangles and $[\text{BO}_4]$ tetradral which form different superstructural units like; boroxol rings, metaborate rings and chains, pentaborate, diborate, triborate and pyroborate [2]. Also, in the pure B_2O_3 glass consists of $[\text{BO}_3]$ groups and with increasing alkali concentration, the first incorporation of alkali oxide leads to the coordination shift $[\text{BO}_3]$ to $[\text{BO}^{4-}]$ with alkali ions compensating the charge of the $[\text{BO}^{4-}]$ tetrahedra. A strengthening of the structure occurs, since the points of polyhedra linkage rise from three to four. At higher alkali concentrations, the structure weakened again due to the formation of $[\text{BO}_3]$ groups with nonbridging oxygens. This double change of coordination number explains minima or maxima of some properties which occur with increasing alkali concentration. Furthermore, this anomaly depends also on the temperature. According to Dietzel [3], the

Corresponding author: Djamila Aboutaleb, research fields: special glasses, minerals materials, characterization of materials (glass and mineral materials). E-mail: jojosaf@yahoo.fr.

boron anomaly should not exist in glasses at temperatures above 1,000 °C, i.e., above this temperature only $[\text{BO}_3]$ groups occur in the melt. The association of $[\text{BO}_3]$ planar triangles with oxygen atoms into $[\text{BO}^{4-}]$ groups should, however, occur at lower temperatures. Aluminum oxide acts as an intermediate in glass. Intermediates have a mid-position between network-formers and network-modifiers. Aluminum may either form tetrahedra and so reinforce the network (coordination number 4) or loosen the network in analogy to network-modifiers (coordination number 6). The ionic radius of barium ions is much larger than of aluminum oxide and boron oxide, which results in the coordination number 8. By contrast, the field strength of barium is much smaller resulting in the behaviour as network-modifier. In the $\text{BaO-Al}_2\text{O}_3\text{-B}_2\text{O}_3$ glass system, it was reported that Al_2O_3 behaves as AlO_4 and AlO_6 units in the glass structure [4]. It assumes that aluminium ions enter the structure in the form of three tetrahedral BO_4 and/or Al_2O_3 in the form of AlO_4 having an oxygen in common [5]. Owen [6] proposed for the glass systems of $\text{MO-Al}_2\text{O}_3\text{-B}_2\text{O}_3$; ($\text{M} = \text{Sr}, \text{Ca}$ and Ba) that some of the M atom associate themselves with Al_2O_3 forming AlO_4 and the rest act with B_2O_3 producing BO_4 or non-bridging oxygen ions. The system $\text{BaO-Al}_2\text{O}_3\text{-B}_2\text{O}_3$, have also a negative thermal expansion coefficient, and therefore it is a potential candidate of a zero-expansion material [7, 8]. First research of this system with regard to the thermal expansion coefficient was carried out by MacDowell in 1989 [9, 10].

In the present study some properties of $\text{BaO-Al}_2\text{O}_3\text{-B}_2\text{O}_3$ glass system were investigated by measure like density and chemical durability and the other by calculs. The dilatometric curves were determined and they revealed that the temperature of transition (T_g) and softening (T_s) and dilatation coefficient increases by addition of Al_2O_3 and BaO content.

2. Experiments

2.1 Preparation of the Glass Samples

The glasses selected were prepared starting from the following chemical raw materials; barium carbonate, orthoboric acid and aluminum oxide. The finely crushed mixture was then placed in a platinum crucible and transferred to an electric furnace at temperature ranging from 1,300 °C to 1,400 °C with a stage for 1.5 h. The liquid was then cast in a graphite mold preheated to approximately 250 °C to limit the thermal shocks during hardening. The samples were annealing then at 350 °C for 1 h. The compositions of studied glasses are given in table 1.

2.2 DTA and TGA Analysis

The apparatus used was a simultaneous thermal analysis apparatus type STA 449C. Jupiter, it can give the differential variations in temperatures, changes in weight during treatment and thermal enthalpies exchanged. It works at high temperature furnace with protective tube of Al_2O_3 and temperature range 25 to 1,550 °C. The type of the thermocouple used is Pt/Pt Rh.

The glass transition temperature (T_g) was determined from the second endothermic peak of DTA curve whereas the crystallization temperatures (T_c) was determined by the first exothermic peak of DTA curve [5].

2.3 Dilatometric Analysis

The expansion curves of samples were determined using a dilatometer DIL 402C (Materials Mineral Composite Laboratory (MMCL-Boumerdes-Algeria) at an average speed of heating of $5 \text{ K}\cdot\text{min}^{-1}$. The sample had a rectangular shape with an 8 mm width and a 20-25 mm length.

The glass transition temperature (T_g) was determined from the expansion curve using the interception method, whereas the softening temperatures (T_s) was determined by the maximum temperature of expansion curve [5, 7, 8].

Table 1 Chemical composition of studied B₂O₃-BaO-Al₂O₃ glasses system.

	Composition (weight %)			Composition (molaire %)		
	B ₂ O ₃	BaO	Al ₂ O ₃	B ₂ O ₃	BaO	Al ₂ O ₃
G ₁	95	5	-	97.70	2.29	-
G ₂	85	10	5	91.73	4.88	3.76
G ₃	75	15	10	84.92	7.69	7.77
G ₄	65	20	15	77.5	10.83	12.25

Table 2 Values obtained of T_g and T_s of (BBA) glass system.

Samples	T_g (°C)	T_s (°C)
G ₁	312.3	335.5
G ₂	387.7	417.1
G ₃	422.8	443.8
G ₄	512.8	536.4

Table 3 Values obtained of density (ρ) and molecular volume (V_m) of BBA glass system.

Samples	ρ (g/cm ³)	V_m (cm ³ /mol)
G ₁	1.850	38.665
G ₂	2.143	35.081
G ₃	2.432	32.416
G ₄	2.561	32.391

2.4 Density Measurements

The densities were determined out using Archimedes' method with xylene as an immersion fluid. The relative error in these measurements was about $\pm 0.03 \text{ g}\cdot\text{cm}^{-3}$ and the molar volume V_m was calculated from the molecular weight M and the density ρ according to the relation: $V_m = M/\rho$. The density results are illustrated in Table 3.

2.5 Determination of Chemical Durability

The chemical treatment of the samples under the various conditions (neutral, acidic and basic) was carried and the weight loss of samples was determined.

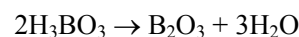
2.6 Theoretical Calculs of Properties

In the structure of glass, the various components contribute a share defined in the effect of certain properties. There would be thus a possibility of calculating by means of additive formulas these properties to leave the composition [11].

3. Results and Discussion

3.1 DTA and TGA Analysis

The (DTA) curves of these glasses, show endothermic peaks between 100 and 200 °C (Fig. 1), knowing that towards the temperature 100 °C, the boric acid starts to lose its water, giving initially metaboric acid, and by dehydration supplements with 300 °C, it forms vitreous boric anhydride according to the following relation:



This is accompanied by an important loss by mass presented in the relative curves TGA, however this loss of mass decreases with the reduction in the content of B₂O₃ (of G₂ towards G₄). The second endothermic peaks which this locate at various temperatures for various glasses represent the temperatures of vitreous transitions, their values increase with the increase in the oxide Al₂O₃ and BaO.

In parallel, various first exothermic peaks corresponding to the beginning of crystallization of the vitreous samples which show also an increase in the values with the increase in the oxide Al₂O₃ and BaO. Thus, the addition of the oxides Al₂O₃ and BaO in the systems of glasses (BBA) increases the temperatures of vitreous transition and the temperatures from crystallization of these glasses.

3.2 Dilatometric Analysis

The obtained curves of thermal dilation are represented in the Fig. 2. For glass G₁ the thermal curve of dilation is representative of glass separated in two phases, because there are two glass transition temperatures represented by two points of inflection on the curve. The B₂O₃-BaO binary system is known by

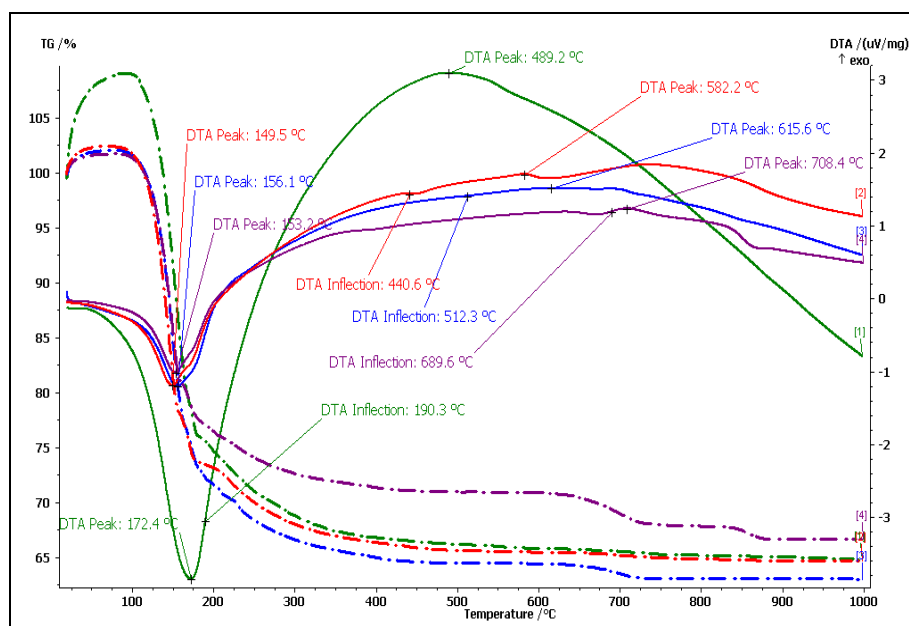


Fig. 1 DTA and TGA curves for obtained (BBA) glass system.

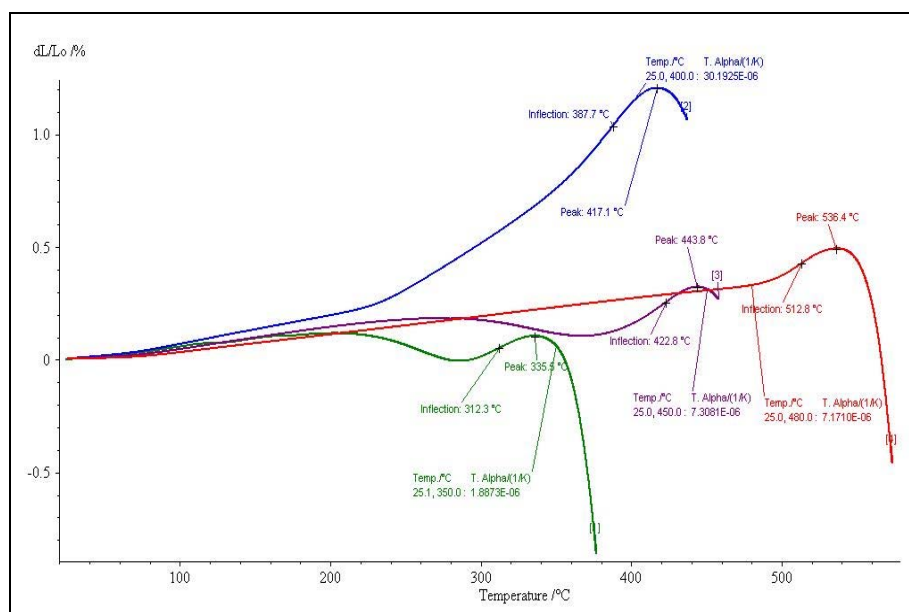


Fig. 2 Expansion curves of for obtained (BBA) glass system.

its mechanism of separation of phase [12, 13]. The G1 sample obtained has a translucent white aspect. With the addition of five percent of alumina (5% Al_2O_3), the phase separation decreases and the other glasses are homogeneous.

The temperatures of vitreous transition T_g and softening temperatures T_s increase by G1 towards G4 with the addition of Al_2O_3 and BaO, because these the last two oxides are known by their role to increase the

viscosity of the molten bath but thermal dilation increases by G1 towards G4. Generally, glasses with the lower expansion coefficient have higher transition and softening temperatures and vice versa [11]. However, it can be seen in Fig. 2 that the expansion increases and the T_g and T_s temperatures increase with additions of Al_2O_3 and BaO oxides.

This is with the molar report/ratio $\text{Al}_2\text{O}_3/\text{B}_2\text{O}_3$ which increases by G1 towards G4, or the B^{3+} ions go

to join with Al_2O_3 by forming the tetrahedrons AlO_4 and the remainder will act with the B_2O_3 by producing not bridging oxygen (NBO) what has to weaken the vitreous network and dilation has to increase. Substitution of BaO for B_2O_3 in the studied glass seems to lead to the conversion of NBO'S formation.

3.3 Density and Molar Volume

Density variation and molar volume for obtained (BBA) glass system as a function of Al_2O_3 mol% are given in Fig. 3a. Adding the BaO and Al_2O_3 oxides increase density: alkali earth ions (Ba) fill the free volume and Al_2O_3 behaves as AlO_4 and AlO_6 units in the glass structure so the molar volume decreases (Fig. 3b).

3.4 Chemical Durability

Results illustrated in Table 4 showed that the samples exhibited an increase in durability under the three media conditions studied (neutral, acidic and basic) with increase of aluminium content. Chemical

attack decreases with increasing the aluminum content in all medium. The reactions between the ion H^+ and the “acid” network can be neglected since the components are packed too strongly to allow for any possibility of migration in the network to take place. On the other hand, the network modifiers have a certain freedom of displacement through vacuum and also the ability to pass through the solution that surrounds them if this vacuum borders the solution. The attack by the alkaline solutions on the other hand is governed by another mechanism.

The OH^- ion is in the case the determining factor, because its ability to react with the network. As a consequence, it appears that this result in a network division, which under certain conditions can result a complete dissolution of glass. It also appears that the solubility of glass increases under basic pH conditions [14]. When comparing the ratio of attack by acid versus water, this attack decreases with increasing Al_2O_3 content, which also reinforced the structure and reduces the chance of network division and destruction.

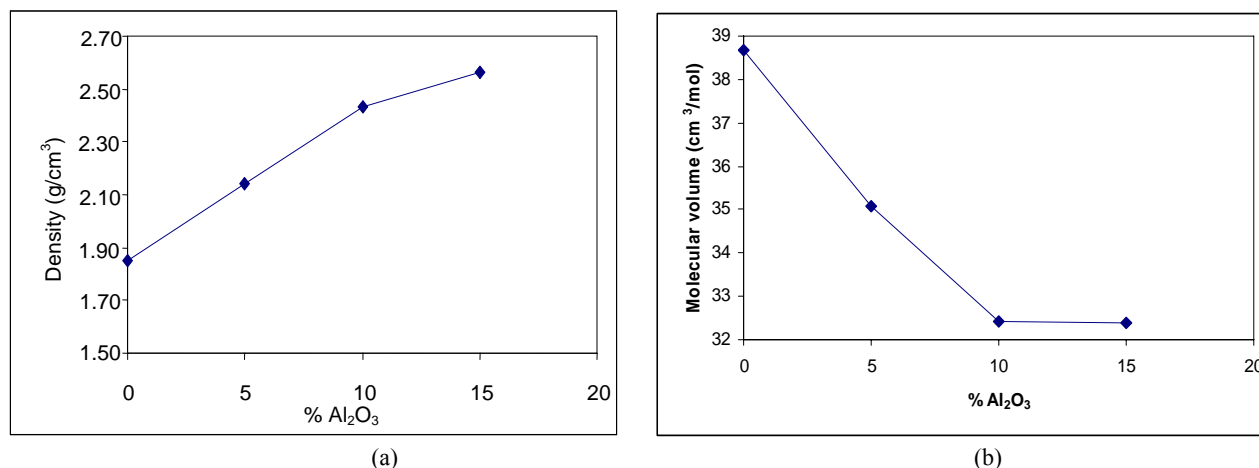


Fig. 3 Variation of ρ and V for obtained (BBA) glass system as a function of Al_2O_3 mol%. (a) density (b) molecular volume.

Table 4 Chemical durability for obtained (BBA) glass system.

Sample	Acid solution (HCl)			Basic solution (NaOH)			Neutral solution (distilled water)		
	M_0 (g)	M_1 (g)	$\frac{M_0 - M_1}{M_0} (\%)$	M_0 (g)	M_1 (g)	$\frac{M_0 - M_1}{M_0} (\%)$	M_0 (g)	M_1 (g)	$\frac{M_0 - M_1}{M_0} (\%)$
G ₁	2.759	1.640	40.55	4.271	3.940	92.74	2.139	0.259	87.89
G ₂	1.443	0.775	46.29	2.228	0.380	89.94	2.382	0.622	73.88
G ₃	2.211	1.715	22.43	4.256	0.947	77.74	4.752	3.264	31.31
G ₄	1.262	1.235	2.13	2.508	1.652	34.13	2.691	1.865	30.69

Table 5 Theoretical properties calculated.

	Properties											
	α in % mass	n_d	d	E	σ	ρ	δt	δc	C_p	λc	ε	α in % molar
G1	0.813	1.48	0.006	252.5	94.5	1.95	64.25	857.5	0.219	0.04	5.84	0.43
G2	2.093	1.49	0.007	307.5	136.0	2.11	62.75	820	0.21	0.045	6.71	1.84
G3	3.364	1.51	0.007	362.5	177.5	2.26	61.25	782.5	0.201	0.050	6.96	3.15
G4	4.639	1.53	0.008	410	219.0	2.45	59.75	745	0.192	0.056	7.60	4.21

3.5 Theoretical Calcul of Properties

The results from the calculated properties are given in Table 5. According to Winkelmann and Appen, it is observed that the expansion values are respectively low in the range of 20-100 °C and 20-400 °C due to the presence of boron oxide B_2O_3 which generally reduces the coefficient of thermal expansion α of glasses [15]. The α values increases (which may be due to the decrease in boron oxide and the presence of BaO and Al_2O_3) and the formation of non-bridging oxygen. Results by Winkelmann and Appen are slightly different and are almost similar. The density increases with the addition of barium and alumina, as both ions have relatively large molar masses.

The presence of boron oxide also increases the refractive index of glasses which explains the high value of the refractive index calculated. Even alkaline earth oxides also contribute to the elevation of the refractive index and dispersion. With the reduction of other oxides such as boron oxide and the increase of barium and alumina the amount of non-bridging oxygen increases and this leads to an increase in the elastic modulus E and Poisson's ratio. Note that the compressive strength σ_c is higher than the tensile strength σ_t [14].

The mechanical strength of glass increases with the strength of the bonds of the glass structure. The samples prepared show low values of mechanical strength, the structure is not rigid enough, and with creation of NBO oxygen, there is a decrease in tensile strength and compression. Ordinary glasses generally are characterized by a specific heat value of about 0.8 CP (J/gk) by boric oxide increases against the property in the glasses. And with the decrease in B_2O_3

and higher alumina, there was decrease in specific heat value. With the addition of Al_2O_3 , there was a slight increase in thermal conductivity e , non-bridging oxygen ions increase the heat transfer inside the glass.

A decrease in the surface tension value was observed in systems of binary or ternary glasses of borates, alkaline earth oxides are important to the surface. There is a relationship between the primitive and the index of refraction as a decisive influence on the polarizability of oxygen ions. When, the B_2O_3 content decrease, an increase of permittivity values with polarizability of ions (non-bridging oxygen ions) was observed with the same manner like the index of refraction.

4. Conclusions

In the studied glass system BaO- Al_2O_3 - B_2O_3 samples have a transparent appearance (homogeneous), except that the sample G1 is heterogeneous and presents phase separation at binary BaO- B_2O_3 glass, then the phase separation disappears with addition of more amount of alumina.

The addition of the alumina at the same time as some barium in the component B_2O_3 contributed to the creation of non-bridging oxygen. Although the temperatures of transitions glassy T_g and softening T_s increased (because of the increase of the viscosity of the bath), Also densities and the coefficients of expansion increased. The creation of non-bridging oxygen led to an increase of the module of elasticity and this fact the reduction in the mechanical properties as the traction resistance and to the compression and the Poisson's ratio but there is an increase in chemical properties. The increase of the polarizability of the

ions oxygen has to lead to the increase of the refractive index and the dispersal as well as the electric permittivity. The properties of transfer increased as the conduction of heat and the superficial tension on the other hand the specific heat decreased.

References

- [1] H.A. Silim, Composition effect on some physical properties and FTIR of alumino-borate glasses containing lithium, sodium, potassium and barium oxides, Egypt. J. Solids 29 (2) (2006) 293-302.
- [2] G.A. Khater, The use of some egyptian clays for the production of glass-ceramic materials, M.Sc. Thesis, Ain Shams University, 1986.
- [3] A. Dietzel, Glass structure and glass properties: 2. Glastechn. Ber. 22 (1948) 81-86.
- [4] G.A. Khater, E.M.A. Hamzawy, Effect of different nucleation catalysts on the crystallization behavior within the $\text{CaO-MgO-Al}_2\text{O}_3\text{-SiO}_2$ system, Silic. Ind. 73 (2008) 103-106.
- [5] C. Hirayama, Properties of aluminoborate glasses of group II metal oxides electrical properties. J. Am. Ceram. Soc. (45) (1962) 288-293.
- [6] A.E. Owen, Properties of glasses in the system $\text{CaO-B}_2\text{O}_3\text{-Al}_2\text{O}_3$: Part 1. The DC conductivity and structure of calcium boroaluminate glasses, Phys. Chem. Glasses 2 (1961) 87-98.
- [7] E.J. Smoke, Ceramic compositions having negative linear thermal expansion, J. Am. Ceram. Soc. (34) (1951) 87-90.
- [8] R.M. Hovhannisyan, Rafaelites-new kind of glass ceramics with low thermal expansion and low melting temperatures on the basis of alkaline earth aluminium borates, Glass Technol. 44 (2003) 96-100.
- [9] J.F. MacDowell, Aluminoborate glass-ceramics with low thermal expansivity, J. Am. Ceram. Soc. 73 (1990) 2287-2292.
- [10] J.F. MacDowell, P. Yan, Alkaline earth aluminoborate glass-ceramics, US Patent 4861734 (1989).
- [11] H. Scholze, Glass: Nature, Structure and Properties, Springer, New York, 1991,
- [12] D. Aboutaleb, Study of phase separation on borate and borosilicate glasses, Ph.D. Thesis, Boumerdes University, Algeria, 2010.
- [13] D. Aboutaleb, J. Douglad, B. Safi, O. Jbara, A. Iratni. Phase separation and chemical durability in the $\text{SiO}_2\text{-B}_2\text{O}_3\text{-Na}_2\text{O}$ (SBN) glass system, Asian Journal of Chemistry 24 (2) (2012) 473-480.
- [14] H.E. Lin, W.R. Foster, Studies in the system $\text{BaO-Al}_2\text{O}_3\text{-SiO}_2$, The polymorphism of celsian ($\text{BaAl}_2\text{Si}_2\text{O}_8$), Am. Mineral. 53 (1966) 134.
- [15] J.E. Shelby, Introduction to Glass Science and Technology, The Royal Society of Chemistry, Cambridge, 1997, pp. 48-67.

Research into Excited Long Lived 0.6-6.0 keV Energy Levels in the Cathode Solid Medium of Glow Discharge by X-Ray Spectra Emission

Alexander Borisovich Karabut

FSUE SIA LUTCH, Podolsk 140055, Moscow Region, Russia.

Received: January 31, 2013 / Accepted: February 27, 2013 / Published: May 25, 2013.

Abstract: X-ray emissions have been registered in experiments with high-current glow discharge from the different cathode and different plasma forming gases within 100 ms and more after turning off the current. The emission X-rays was realized: in the form of laser microbeams (up to 10^4 beams a second and up to 10^{10} X-ray of quanta in a beam, angular divergence was up to 10^{-4}). The fine structure of X-ray spectra were detected using a bent mica crystal X-ray spectrometer and recorded on X-ray film after the discharge current switching off (during up to 20 h afterwards). The X-ray energy was 0.8-6.0 keV. The possible mechanism and phenomenon model of producing the X-ray emission on the solid medium cathode with the excited energy levels was considered.

Key words: High-current glow discharge, solid medium cathode, X-ray emission.

1. Introduction

The experiments on defining a possible mechanism of high energy phenomena in the solid-state cathode medium of the high-current glow-discharge were carried out before. The generation of penetration radiation was registered by the researches of high energy process in solid cathodes of electric discharge [1]. The experiments were carried out on the high-current Glow Discharge device in D_2 , H_2 , He, Kr and Xe at pressure up to 10 Torr, current up to 300 mA and the Glow Discharge voltage ranging 1,500-4,300 V. The cathode samples being made of Al, Sc, Ti, Ni, Nb, Zr, Mo, Pd and Ta, W. The registration of X-ray emission was performed using Al_2O_3 -based TLD (Thermo-Luminescent Detectors), the pine hole and PM scintillating detectors for the recording of temporal characteristics [2-7]. The following modes were brought during the experiments: (1) diffusion

X-ray emission was observed in the form of separate X-ray flashes (up to 10^5 X-ray in flashes/s and up to 10^4 X-ray photons in a flash), (2) X-ray beams emission by small angular divergence occurs during the discharge burning and up to 100 ms and more after the current turning out. The X-ray spectra were registered in film using the curved mica crystal X-ray spectrometer. The X-ray spectrum were registered both as bands of the continuum with energies ranging 0.6-10.0 keV and as spots resulting from the emission of series of high-density monoenergetic X-ray beams (with energies of 0.6-10.0 keV) characterized by small angular divergence. The spectra were repeatedly recorded during the glow discharge operation and after the glow discharge current switch off (for up to 20 h afterwards) [9]. The results obtained with different types of detectors are related to each other well. All the experimental results have 100% reproducibility. Experiment on the X in the absence of current electrical discharge of particular importance for a variety of application uses.

Corresponding author: Alexander Borisovich Karabut, doctor, Ph. D., research fields: plasma, laser and nuclear physics. E-mail: abkarab@mail.ru.

2. Experiments

2.1 Glow Discharge Device

The measurements were carried out using the glow discharge device consisting of a water-cooled vacuum chamber, the cathode and the anode assemblies (Fig. 1a). The cathode design allowed the placement of cathode samples made of various materials on a water-cooled surface. The experiments were carried out using a high-current glow discharge in D_2 , H_2 , He, Kr and Xe and the cathode samples being made of Al, Sc, Ti, Ni, Nb, Zr, Mo, Pd, Ta and W.

2.2 Electric Discharge Power Supply

A pulsed power supply was used in the experiments. The scheme of the pulse, periodical power supply was contained a sequence of high-voltage transistor switches, which are controlled from the driving pulse generator. Power supply contained five high-voltage transistor switches with operating voltages up to 4,500 V and current up to 300 mA (Fig. 1c).

3. X-Ray Registration

3.1 X-Ray Scintillator-Photomultiplier Detectors

The energy, spatial and time characteristics of the penetrating radiation were determined with use of the scintillation detectors supplied with the

photomultipliers (PM). The signal from PM was transferred to a fast preamplifier and then to the two-channel computer digital oscillograph with the limit resolution frequency of 50 MHz per a channel [5].

X-ray emission in the form of laser beams was registered after passing the trailing edge of the glow discharge current pulses and turning glow discharge current. X-ray emission in the form of laser beams was registered for different cathode materials (Figs. 2a, 2b) and different gazes (Fig. 3).

3.2 X-Ray Energy Measurements.

The intensity of the luminous flux from the scintillator in the mode of generating the X-ray laser beams was very much. In this case, the amplification constant of the radiation recording system changed by changing the supply voltage of the photomultiplier and changing the amplification constant of the oscillograph [8]. Under some experiments the luminous-absorbing filter attenuating the luminous flux coming to PM was installed between the scintillator and PM. Two types of the filters attenuating the luminous flux by 50 times and by 2500 times respectively were used. For the PM scintillator detector the relative intensity of the X-rays was determined as the total of the amplitudes ΣA_i of all the X-ray bursts within the time interval of 1 second. The

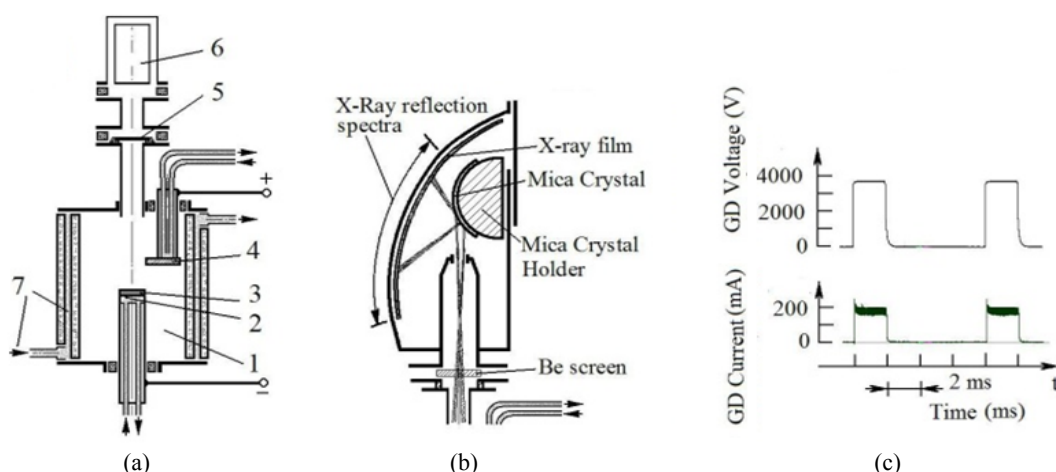


Fig. 1 Schematic representation of the experiment: (a) glow discharge device, (1) discharge chamber, (2) cathode holder, (3) cathode sample, (4) anode, (5) be foil screens, (6) X-ray scintillator, photomultiplier detectors, (7) cooling water; (b) X-ray spectrometer; (c) Glow discharge voltage and current oscillograms.

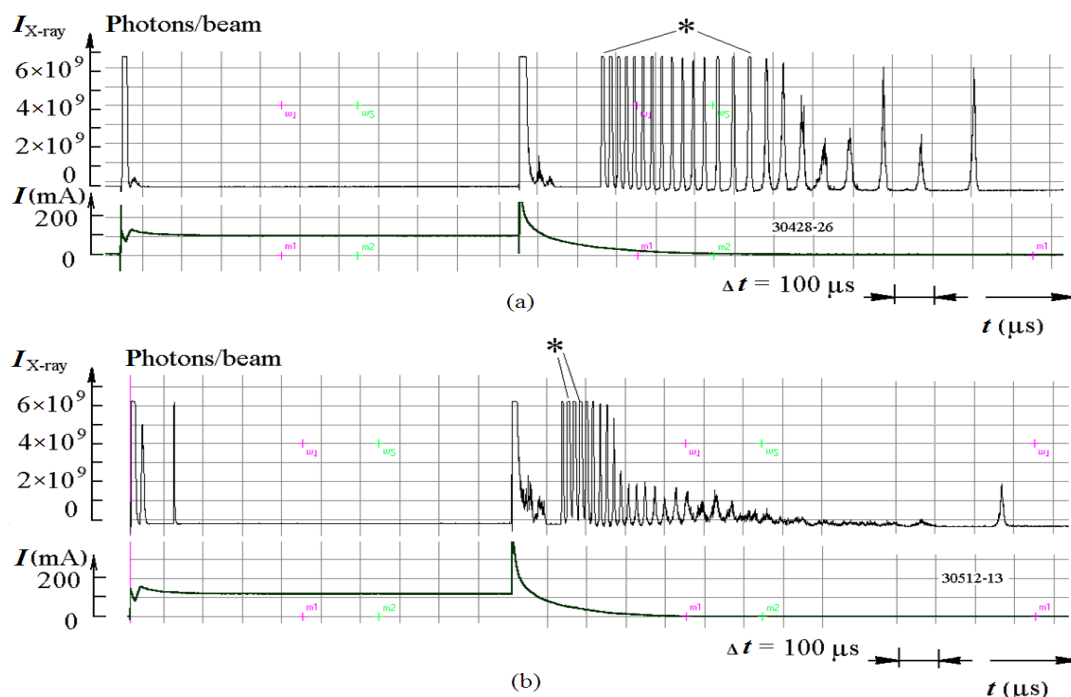


Fig. 2 The typical oscillograms of bursts from X-ray laser beams (PM, scintillator with optical filter) in the discharge for different kind of assemblies. (a) the cathode sample is Ta; (b) the cathode sample is Mo, current, 100 mA, D2. (a) PM, scintillator arrange at a distance of 21 cm from cathode; (b) PM, scintillator arrange at a distance of 70 cm from cathode.

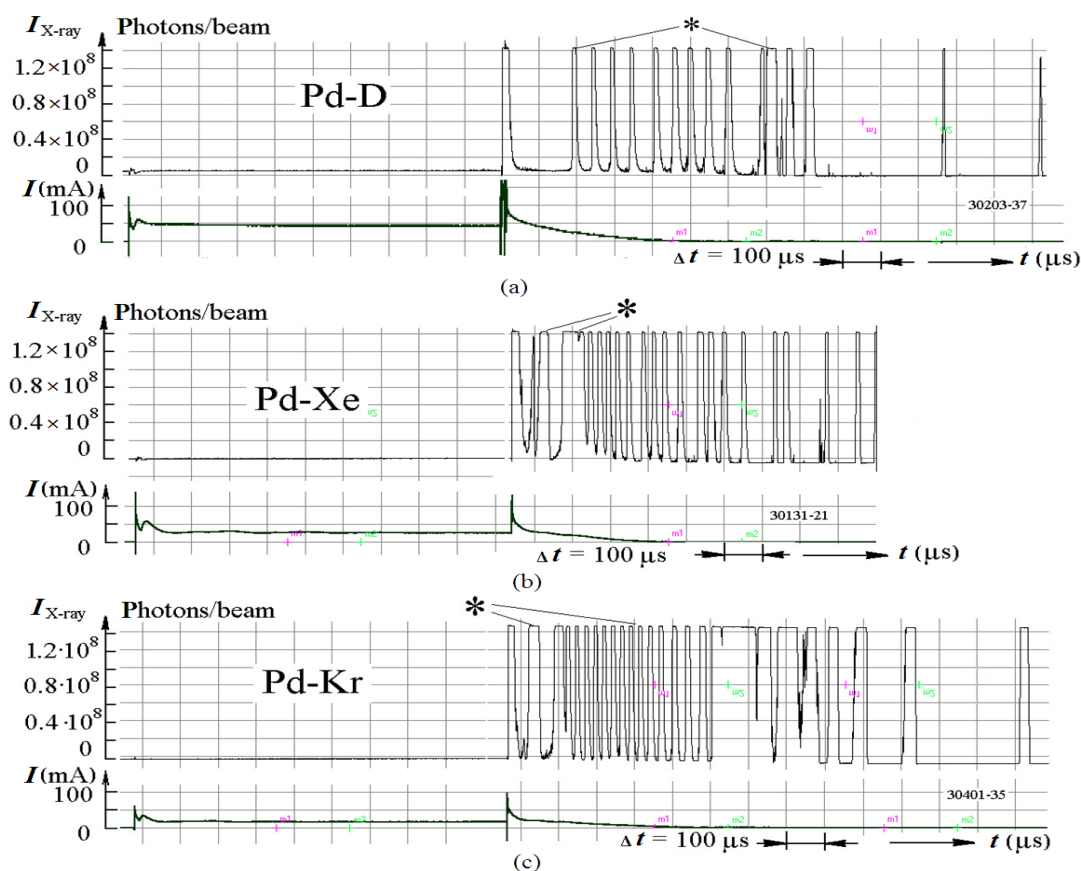


Fig. 3. The typical oscillograms of bursts from X-ray laser beams (PM, scintillator) in the discharge for different kind of gases. The cathode sample is Pd, current, 50 mA. *, the pulse peak was cut a discriminator of amplifier. (a) D2, (b) Xe, (c) Kr.

experiments with using the system of the scintillator, PM and shields made of the beryllium foil with thickness of 15 μm and 30 μm gave the assessment of the X-rays energy value of $E_{\text{X-ray}} \approx 1.0\text{-}2.5$ keV (for different cathode materials) (Table 1).

3.3 The X-Ray Emission Temporal Characteristics

X-ray emission as a function of time was studied with photomultiplier scintillator detectors.

The X-ray emission production begin after glow discharge the switching on in some time.

The time delay of X-ray emission production decrease for the increase of glow discharge current and voltage. The time delay of X-ray emission beginning is very small for high voltage glow discharge. Presumably the solid medium activation and the inverse population creation in solid after glow discharge switch on realize after some time.

The X-ray emission production occurred during the glow discharge operation, and, after the glow discharge current switch off. The generation of X-ray emission in the form of laser beams began when the glow discharge operational parameters increased (duration of current pulses, current density, GD voltage) and was observed as powerful flashes for the different cathode materials and for the different

plasma forming gases. X-ray beams emission was registered through several time after passing the trailing edge of the Glow Discharge current pulses (Fig. 4). The different values of the time delay was registered in experiments [9]. The temporal characteristic of X-ray beams emission was made for the following conditions: time zero point correspond of the trailing edge time of the discharge current pulse, the number of X-ray beams was counted for each value of the time delay. The temporal characteristic of X-ray beams emission show what the time delay are the fix values with the ± 2 μs deviation (Fig. 5).

4. X-Ray Spectra Registration after Glow Discharge Switch off

The X-ray emission spectra were measured using the curved mica crystal X-ray spectrometer (the mica crystal holder is 50 mm diameter), with the spectrum being registered on X-ray film [9, 10]. The film includes the refraction spectra, the direct X-ray lighting, and reflection spectra, with reflection spectra used for data processing. The direct X-ray lighting limits the reflection spectra in the high energy area. The wavelength and the energy of the X-ray were determined according to the expression: $m\lambda = 2d \sin\theta$;

$$E_{\text{X-ray}} = 1.235/\lambda \quad (1)$$

Table 1 X-Ray photon energy for discharge current absence.

Material of Cathode	Al	Sc	Ti	Ni	Mo	Pd	Ta	Re	Pt	Pb
Glow discharge voltage (V)	1,650	1,540	1,730	1,650	1,420	1,650	1,600	1,520	1,650	1,610
Glow discharge current (mA)	130	130	170	150	210	138	38	125	138	138
X-ray energy, current switch off, $E_{\text{X-ray}}$ (keV)	1.68	1.5	1.46	1.96	1.33	1.71	1.62	1.38	1.75	1.45

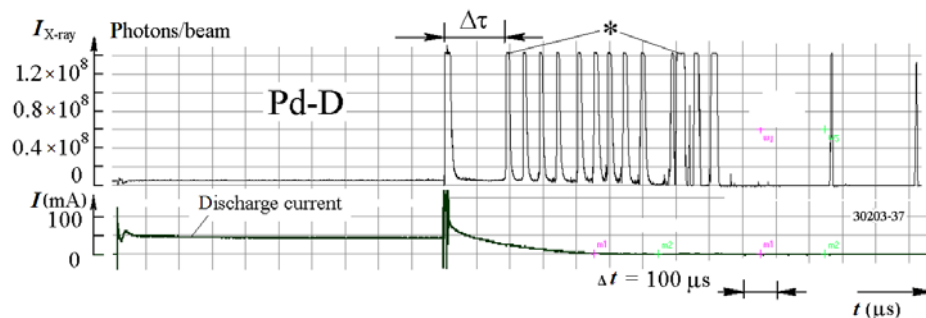


Fig. 4 The typical oscillograms of bursts from X-ray laser beams (PM, scintillator) after glow discharge turning. The cathode sample is Pd, D2 discharge current, 50 mA.

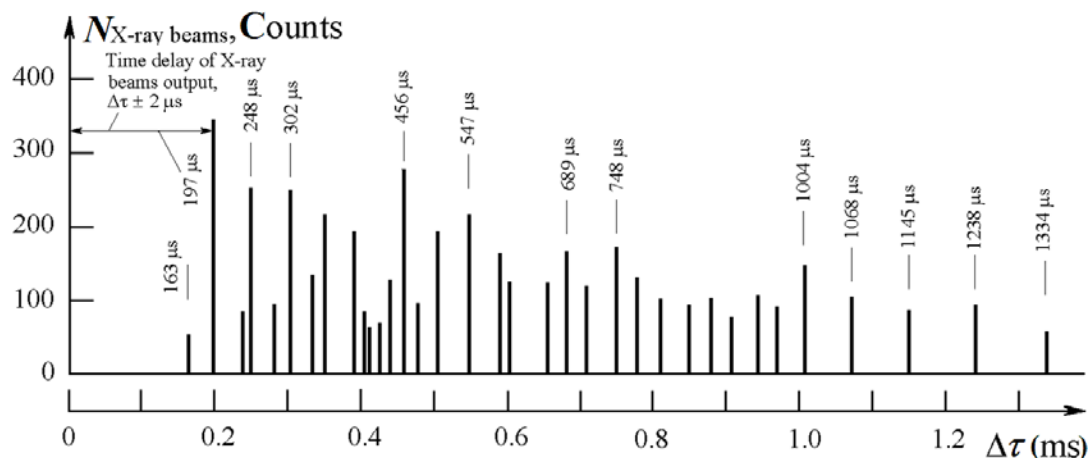


Fig. 5 Temporal characteristic of X-ray beams emission. The cathode sample is Pd, D2 discharge, current, 50 mA.

where m is the spectrum order; λ stands for the X-ray emission wavelength in nm; $2d$ is the constant of the mica crystal lattice ($2d = 2.0$ nm); and θ represents the reflection angle. The spectra were repeatedly recorded during the glow discharge operation and after the glow discharge current switch off (for up to 20 h afterwards). The spectra spots were located in spectral areas specific for a given cathode material used (Figs. 6-9).

5. Phenomenological Model of High Energy Cathode Processes

X-ray emission was registered from cathode electric discharge for electric current absents. These results are the consequence of a fundamental phenomenon unknown before: “Formation of a crystal lattice of a solid body when bombarding its surface by plasma ions of an electrical discharge of metastable excited long-living (up to tens ms and more) states with the excitation energy of 1-3 keV and more in a solid body”. This phenomenon was registered in experiments for all cathode materials and all plasma forming gases [10]. Now opinion it exist that the electrons in metals carry relaxation of excited levels. Experiments with registration X-ray emission from the cathode electric discharge in the absence of discharge current allows to conclude that in metals can create the inverted population environment with energy 1-3 keV and more long-lived excited states.

Formation of excited energetic levels with such energy values are supposed to occur in processes of non-elastic interaction of the plasma ions of the electric discharge with electronic shells of the solid

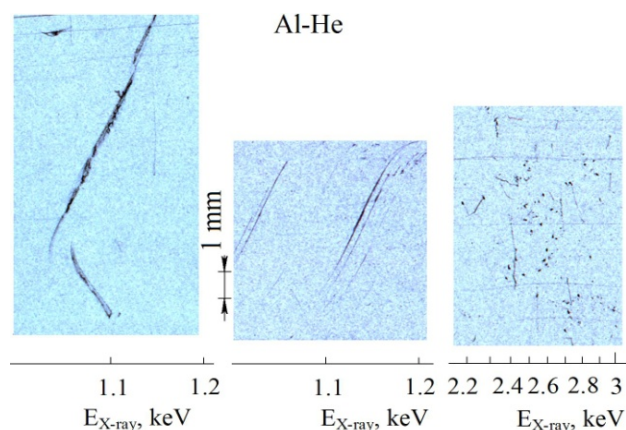


Fig. 6 X-ray energy spectra in the spots and bands modes for Al cathode after the He glow discharge switch off. Exposition time is 20 h.

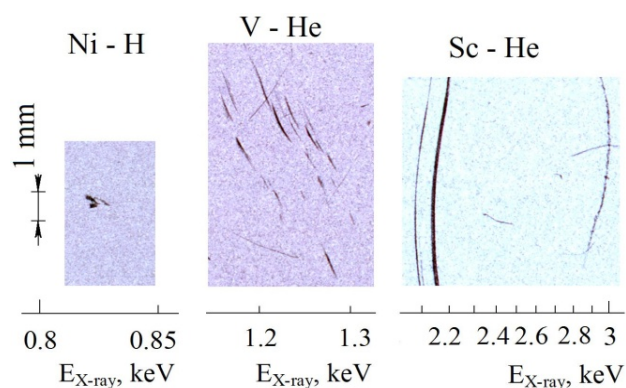


Fig. 7 X-ray energy spectra in the spots and bands modes for Ni, V and Sc cathodes after the He glow discharge switch off. Exposition time is 20 h.

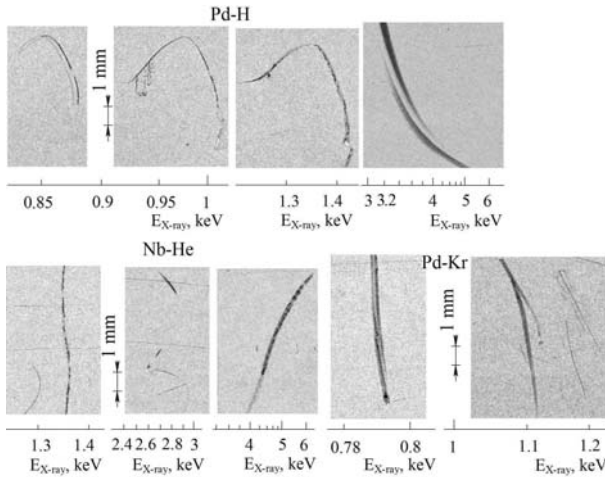


Fig. 8 X-ray energy spectra in the spot modes for different cathode materials after the glow discharge switch off. The cathode material and plasma gas forming was indicated. Exposition time is 20 h.

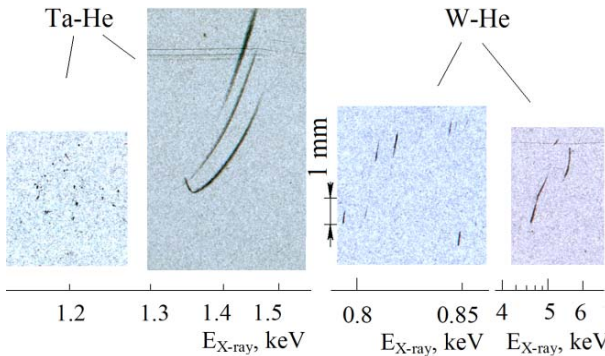


Fig. 9 X-ray energy spectra in the spots and bands modes for Ta and W cathodes after the He glow discharge switch off. Exposition time is 20 h.

body ions. Fast relaxation of the metastable long-living excited ions states with the generation of X-ray emission. The totality experimental results permit to consider the assume low energy nuclear reactions phenomenon theory in the solid medium of the electric discharge systems cathodes.

The main experimental result is following: The lifetime of the long-lived excited states with 1-3 keV energy in solid is possibly.

One can single out the following electric discharge systems areas and physical phenomena observed within them:

The obtained experimental results allow to consider the possible energy processes in the cathode material solid. The following processes may lead to initiation

of low energy nuclear reactions:

- Deuterium ions acceleration in the Glow Discharge near-cathode area to energies from several hundred eV up to a few thousand eV.

- Non-resilient processes of deuterium ions collision with the crystal lattice ions (Pd^{4+} ions for Palladium). These processes cross-section related to non-adiabatic transition is determined according to massey criterion ξ . For $\Delta E = 0.7-1.5$ keV (the near-cathode discharge conditions) the massey criterion ≈ 1 and the non-resilient processes cross-section for optic polar phonons formation becomes close to gaso-kinetic one. Under these conditions the electron frame is displaced relative to nucleus and a dipole or optic polar phonon is formed. The initial optic polar phonons frequency is ω_{op} . At energies $W = 1$ keV $\omega_{op} = 0.95 \times 1,019 \text{ s}^{-1}$ which is higher than the plasma frequency $\omega_p = (1.3-2.5) \times 1,016 \text{ s}$, plasmons are not produced and there is no compensation for the arising spatial division of charges.

- At big concentration of initial optic phonons (high charge current density) non-linear unharmonic processes start playing their essential part. Presumably, processes of the 3rd and the 4th order begin.

$$h\omega_{1 \text{ in}} + h\omega_{2 \text{ in}} \rightarrow h\omega_3 \text{ and } \omega_1 < \omega_3 > \omega_2 \quad (2)$$

$$h\omega_{1 \text{ in}} + h\omega_{2 \text{ in}} + h\omega_{3 \text{ in}} \rightarrow h\omega_4 \text{ and } \omega_1 < \omega_4 > \omega_2, \quad \omega_4 > \omega_3 \quad (3)$$

These expressions mean that two ($h\omega_{1 \text{ in}}, h\omega_{2 \text{ in}}$) or three primary phonons are combined and formed into one $h\omega_3$ or $h\omega_4$. In this way out of a bog number of primary phonons with energies of 0.7-3.0 keV a small number of high energy phonons (up to tens and hundreds keV) is formed. The primary phonons energy spectrum is displaced in the direction of bigger values.

Presumably, some long-lived excited levels with energies up to several keV are formed in the cathode solid by the primary and secondary optic phonons energy. The excited energy levels for different materials are 0.8-6.0 keV.

The non-equilibrium excited energy states with the population density of $n_{\text{exit}} [\text{cm}^{-3}]$ and a characteristic temperature of $T_{\text{exit}} \approx 0.8\text{-}6.0 \text{ keV}$ were deexcited with X-ray emission.

6. Conclusions

The experimental research of this fundamental phenomenon has allowed to create an essentially new type of the device: "The X-ray solid-state laser with a wave length of the radiation of 0.2-1.5 nm, duration of separate pulses of 10^{-11} - 10^{-13} s and beam power in pulses up to 10^7 W ". The obtained results show that creating optically active medium with long-living metastable levels with the energy of 1-3 keV and more is possible in the solid.

Acknowledgments

Authors are happy to express their thanks to: professor Runar Kuzmin, solid and nuclear physic, Moscow State University, Sergey Pikuz, Doctor Ph.D., plasma physic, RAS Lebedev Physics Institute, George H. Miley, professor, plasma and nuclear physic, Ill. University, Peter L. Hagelstein, professor, plasma and laser physic, MIT for their help in this work.

References

- [1] A.B. Karabut, Ya.R. Kuchеров, I.B. Savvatimova, Nuclear reaction on in the cathode gas discharge, Pisma in GTF (Sov. Tech. Phys. Lett.) 16 (12) (1990) 53-57.
- [2] A.B. Karabut, Ya.R. Kuchеров, I.B. Savvatimova, Nuclear product ratio for glow discharge in deuterium, Physics Letters A 170 (1992) 265-272.
- [3] Ya.R. Kuchеров, A.B. Karabut, I.B. Savvatimova, Metod and apparatus for long-term continuous energy production, US Patent, 93/08007 (1993).
- [4] A.B. Karabut, Research into powerful solid X-ray laser (wave length is 0.8-1.2 nm) with excitation of high current glow discharge ions, in: Proceedings of the 11 International Conference on Emerging Nuclear Energy Systems, Albuquerque, New Mexico, USA, 2002, pp. 374-381.
- [5] A.B. Karabut, Experimental research into characteristics of X-ray emission from solid-state cathode medium of high-current glow discharge, in: Proceedings of the 10th International Conference on Cold Fusion, Cambridge, MA, USA, 2003, pp. 585-596.
- [6] A.G. Lipson, A.S. Roussetski, A.B. Karabut, G.H. Miley, Gain of dd, reaction and X-ray emission generation in high current pulsed glow discharge in deuterium with Ti, cathode at 0.8-2.45 kV voltage, Journal of Experimental and Theoretical Physics, Russia 100 (2005) 1175-1189.
- [7] A.B. Karabut, Experimental results on excess power, impurity nuclides, and X-ray production in experiments with a high-voltage electric discharge system, Journal Condensed Matter Nucl. Sci. 6 (2011) 1-20.
- [8] A.B. Karabut, Excess heat production in Pd/D during periodic pulse discharge current in various condition, in: Proceedings of the 11th International Conference on Cold Fusion, France, 2004, pp. 178-193.
- [9] A.B. Karabut, Study of deuterium loading into pd cathode samples of glow discharge, in: Proceedings of 9th International Workshop on Anomalies in Hydrogen/Deuterium Gas Loaded Metals, Siena, Italy, 2010.
- [10] A.B. Karabut, Research into excited 0.6-6.0 keV energy levels in the cathode solid medium of glow discharge by X-ray spectra emission, Journal Condensed Matter Nucl. Sci. 8 (2011) 1-17.

New Composite Electrode Material Based on Glassy Carbone/Polythiophene/MnO₂

Imene Chikouche, Ali Sahari, Fahima Charef and Ahmed Zouaoui

Faculty of Technology, Ferhat Abbas University, Setif 19000, Algeria

Received: November 30, 2012 / Accepted: January 06, 2013 / Published: May 25, 2013.

Abstract: In this paper, it presents the work which consists to develop and characterize a modified electrode with a conductive polymer film, poly [3-methyl thiophene] then incorporating manganese dioxide MnO₂ into the film. The deposition of the polymer film on the surface of the glassy carbon electrode is realized by the electrochemical oxidation of the monomer [3-methyl thiophene] in an organic medium. Then the electrode obtained was immersed in a solution containing ions Mn⁴⁺ to introduce into the polymeric film. The technique of insertion of manganese ions is performed by interaction with the polymer film. The electrochemical oxidation of the modified electrode in an aqueous medium will precipitate the manganese dioxide in the form of particles in the polymer film. In this study, it was found that several parameters affect the amount of manganese dioxide introduced as the pH of the medium and the thickness of the polymer film.

Key words: Modified electrodes, conductive polymer, polythiophene, manganese dioxide, energy storage.

1. Introduction

The urgent need for electric systems and devices that require power sources of high performance have stimulated the research areas related to energy storage. In addition, the increasing environmental and economic impact of the production and the use of fossil fuels have stimulated the search for alternative energy sources, such as electrochemical energy (batteries, fuel cells and electrochemical capacitors) [1]. In this regard, conventional capacitors and batteries are recognized as highly attractive energy storage devices to satisfy the above needs.

Composite materials composed of conductive polymers and inorganic particles have attracted considerable attention because they can combine the advantages of both components and have potential applications in many areas [2]. A variety of organic polymers and inorganic solids have been successfully combined to form nanocomposites structures [3-5].

Polythiophene is one of the promising conducting polymers for use in rechargeable batteries due to its high conductivity, high theoretical specific capacity, and low cost.

The electrochemical modification of electrode surface by polymer films containing metal particles is an effective method to prepare modified electrodes with specific electrocatalytic properties and orient the electrochemical properties of reactions occurring at the interface of these electrodes [6-8].

In this paper, we present our work which consists to develop and study a modified electrode with a conductive polymer film, poly [3-methyl thiophene] and to incorporate manganese dioxide MnO₂ in the film. We will study the influence of certain parameters on the amount of incorporated manganese dioxide.

2. Experiments

In our experience, the electrochemical study of manganese was carried out in two different environments. In aqueous media, the solvent used is distilled water and the sulphate sodium "Na₂SO₄" as

Corresponding author: Imene Chikouche, doctorate student, research field: electrochemistry of materials. E-mail: Chikouche_imene@yahoo.fr.

supporting electrolyte. In an organic medium, the solvent used is acetonitrile, CH₃CN, and the supporting electrolyte is lithium perchlorate, LiClO₄. The reagents used are manganese sulphate, MnSO₄, 2H₂O and the monomer 3-methyl thiophene.

The apparatus used for the characterization of our modified electrode (cyclic voltammetry and coulometry) is VoltaLab 40 (PGZ 301) controlled by a voltamaster software of type radiometer to control the potential and record the electrical current.

The experiments were performed in a three electrode cell. The working electrode is a glassy carbon disk of 0.07 cm² (3 mm of diameter). It was polished with diamond preparation, and then rinsed with distilled water and dried with Joseph paper before each manipulation. The reference electrode on saturated calomel has a fixed and constant potential. The auxiliary electrode is an electrode with a stainless platinum wire.

3. Results and Discussion

3.1 Study of Electrochemical Behavior of Manganese (II) on a Glassy Carbon Electrode

The electrochemical behavior of manganese was studied on a glassy carbon electrode of 0.07 cm² surface by digital cyclic voltammetry in a solution of manganese (MnSO₄) 10⁻² M with 10⁻¹ M of Na₂SO₄.

The obtained curve on a potential range of -1.6-1.6 V/SCE is characterized by the presence of a weak oxidation peak around 0.310 V corresponding to the oxidation of manganese introduced in the reduction of ions of manganese (II) and a very intense peak at 1 V attributed to the formation of Mn⁴⁺ ions. At the return sweep we also observe two peaks in the vicinity of 0.780 V/SCE and 0.005 V/SCE corresponding to the reduction of Mn⁴⁺ species in Mn³⁺ and the Mn³⁺ in Mn²⁺, respectively (Fig. 1a).

Successive scans show an increase of peak intensity of reduction and oxidation. The increase in oxidation peaks is due to the modification of the electrode surface during the scans. The beginning of the oxidation peak in the vicinity of 0.8 V from the sixth cycle corresponds to the oxidation of Mn²⁺ to Mn³⁺ (Fig. 1b).

3.2 Electropolymerization of the Monomer (3-Methyl Thiophene)

The monomer 4 × 10⁻³ M was electropolymerized on glassy carbon by cyclic voltammetry in an organic medium of acetonitrile 0.1 M in lithium perchlorate.

The obtained curve (Fig. 2) shows the presence of an irreversible oxidation peak at 1.45 V corresponding to the oxidation (polymerization) of the monomer and therefore to the formation of poly [3-methyl thiophene]

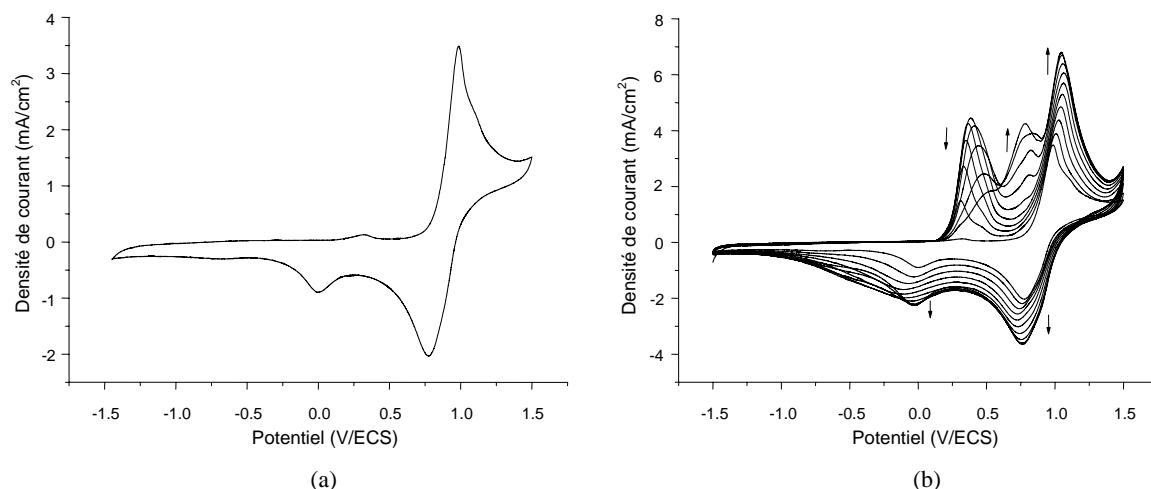


Fig. 1 Oxydo-reduction cyclic voltammograms Manganese (II) plotted on glassy carbon electrode in an aqueous solution 10⁻² M MnSO₄, at $\nu = 100$ mV/s. (a) first cycle and (b) successive scans (10 cycles).

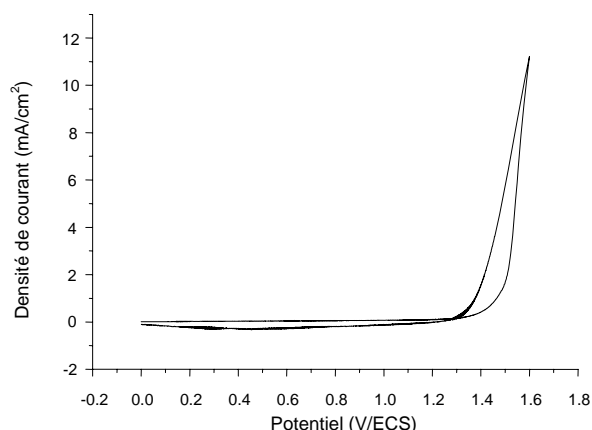


Fig. 2 Cyclic voltammetry curve of the monomer onto glassy carbon electrode ($S = 0.07 \text{ cm}^2$) in CH_3CN 0.1 M LiClO_4 and $4 \times 10^{-3} \text{ M}$ of 3-methyl thiophene, $\nu = 100 \text{ mV/s}$.

deposited on the electrode surface. In return, we see a reduction wave at 0.455 V corresponding to the reduction of the polymer film deposited on the electrode.

Successive scanning leads to the growth of the polymer film deposited on the electrode surface. This is confirmed by the electrochemical response which exhibits a reversible wave in the vicinity of 0.4-0.6 V, attributed to polythiophene (Fig. 3).

3.3 Incorporation of Manganese (IV) in the Polymer Film

In order to incorporate manganese dioxide in the polymer film, we deposited a poly [3-methyl thiophene] film on the surface of a glassy carbon electrode. The electrode thus modified is immersed in a solution of 10^{-2} M MnSO_4 for 10 min to allow the incorporation of Mn (II) by interactions. Then, the electrode was rinsed with distilled water for removing the excess of manganese (II) not associated with the polymer. A cyclic voltammetry was performed in a solution of 10^{-1} M Na_2SO_4 in the potential range between 400 and 1,600 mV at a scan speed $\nu = 10 \text{ mV/s}$ to show the formation of manganese dioxide in the polymer film. The curve obtained is characterized by an intense peak at 1.4 V corresponding to the oxidation of the incorporated Mn (II) in Mn (IV) onto the surface of the modified electrode (Fig. 4).

3.4 Influence of the Medium Concentration on the Amount of Incorporated Mn (II)

A glassy carbon electrode modified with a poly [3-methyl thiophene] film was immersed in solutions MnSO_4 of different concentrations for 10 min and then oxidized in 10^{-1} M Na_2SO_4 by cyclic voltammetry with a scanning speed $\nu = 10 \text{ mV/s}$.

The evolution of the quantity of incorporated manganese in function of the solution concentration is shown in Fig. 5. We note that the amount of

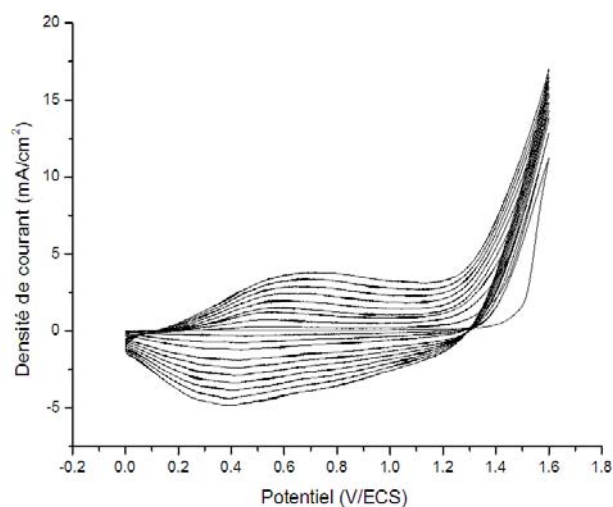


Fig. 3 Diagram of cyclic voltammetry of the electropolymerization of the monomer by successive scans on a glassy carbon electrode ($S = 0.07 \text{ cm}^2$) in CH_3CN with 0.1 M LiClO_4 and $4 \times 10^{-3} \text{ M}$ of monomer at $\nu = 100 \text{ mV/s}$.

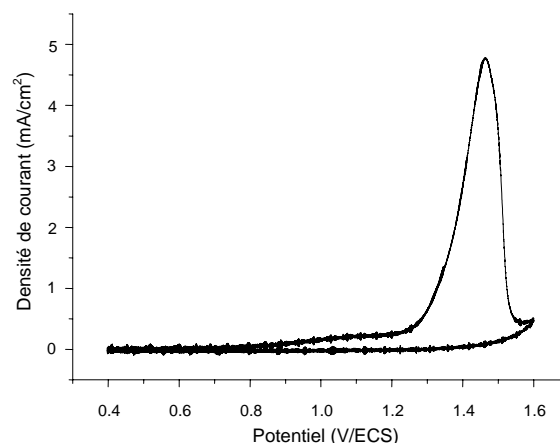


Fig. 4 Cyclic voltammetry diagram of Manganese (II) on glassy carbon electrode modified with a polymer film in an aqueous solution of Na_2SO_4 10^{-1} M for 10 min after immersion in a solution containing cations of Manganese (MnSO_4 10^{-2} M), at $\nu = 10 \text{ mV/s}$.

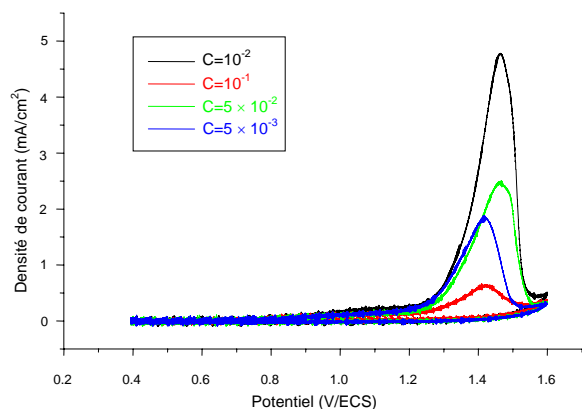


Fig. 5 Anodic oxidations curves of incorporated Manganese (II) in the polymer film in 10^{-1} M Na_2SO_4 after immersion of modified electrodes for 10 min at various concentrations, at $v = 10$ mV/s.

incorporated manganese varies with the concentration. It appears that the interaction between manganese cations and the polymer film depends on the concentration. The optimum incorporated amount is obtained for a concentration of 10^{-2} M.

3.5 Influence of Medium pH on the Amount of Incorporated Mn (II)

We varied the pH of the solution 10^{-2} M MnSO_4 to see its influence on the incorporation of manganese (II) in the polymer film deposited on the glassy carbon electrode. The modified electrode is immersed in the solution of MnSO_4 at different pH between 3.9 and 7 and then rinsed with distilled water to remove excess ions of manganese (II) not retained by the polymeric film. The electrode is then oxidized in an aqueous solution containing only the supporting electrolyte Na_2SO_4 10^{-1} M to oxidize manganese cations (II) retained in the film of manganese (IV) by cyclic voltammetry with a scan rate of 10 mV/s.

The voltammograms obtained at different pH are summarized in Fig. 6. We note that the current intensity of the oxidation peak varies with the medium pH; the amount incorporated is maximal at pH 5.27.

3.6 Effect of Thickness of Poly [3-Methyl Thiophene] Film

To see the effect of film thickness of poly [3-methyl

thiophene] on the amount of incorporated manganese, we passed, by coulometry, various charges: 5 mC, 10 mC and 15 mC for depositing layers of a polymer film of various thicknesses. These modified electrodes were then immersed for 10 min in a solution of 10^{-2} M MnSO_4 to allow the incorporation of manganese (II) in the film by interaction, and then oxidized in an aqueous solution containing Na_2SO_4 10^{-1} M by cyclic voltammetry at a scan rate of 10 mV/s.

We note that the intensity of the peak oxidation is more important for less thinner films (Fig. 7). The interactions between manganese cations and the

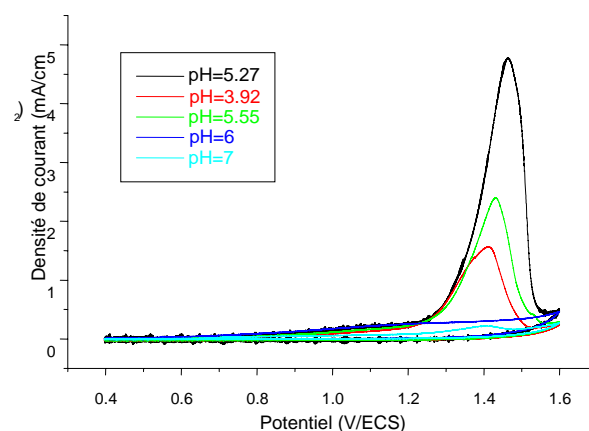


Fig. 6 Anodic oxidations curves of Manganese (II) deposited in the polymer film in 0.1 M Na_2SO_4 , after immersing the modified electrodes for 10 min in a solution of MnSO_4 10^{-2} M at different pH and at $v = 10$ mV/s.

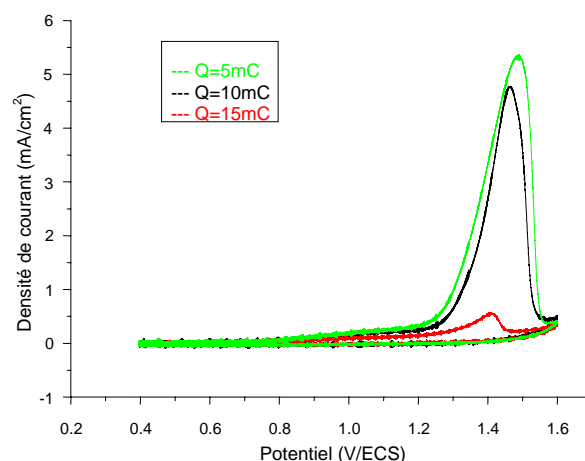


Fig. 7 Anodic oxidations curves in 10^{-1} M Na_2SO_4 Manganese (II) incorporated into the polymer film after immersion of modified electrodes for 10 min in a solution of MnSO_4 10^{-2} M at different thicknesses and at $v = 10$ mV/s.

polymer film depend on the film thickness. When the film is thick, the interactions decrease due to the non permeability of the polymer.

4. Conclusions

In this work, the film deposition of poly [3-methyl thiophene] to the surface of the glassy carbon electrode is done by the electrochemical oxidation of the monomer in an organic solution of acetonitrile. The inclusion of the manganese dioxide in the films of poly [3-methyl thiophene] is performed by immersion of the modified electrode in an aqueous solution containing manganese ions for incorporation in the polymeric film by interaction, followed by an electrooxidation to precipitate the manganese dioxide particles. The presence of manganese dioxide (Mn⁴⁺) in polymer films is confirmed by the presence of an oxidation peak of incorporated manganese.

We found that several parameters affect the amount of incorporated manganese dioxide such as the solution concentration, the medium pH and the thickness of the polymer film.

References

- [1] E.C. Rios, A.V. Rosario, R.M.Q. Mello, L. Micaroni, Poly(3-methylthiophene)/MnO₂ composite electrodes as electrochemical capacitors, *Journal of Power Sources* 163 (2007) 1137.
- [2] X.X. Liu, L.J. Bian, L. Zhang, L.J. Zhang, Composite films of polyaniline and molybdenum oxide formed by electrocodeposition in aqueous media, *J. Solid State Electrochem* 11 (2007) 1279.
- [3] A. Lerf, Intercalation compounds in layered host lattices: supramolecular chemistry in nanodimensions, *Handbook of Nanostructured Materials and Nanotechnology*, H. Nalwa, ed., Academic Press, New York 5 (2000) 1-166.
- [4] S.J. Komarneni, Feature article: Nanocomposites, *J. Mater. Chem.* 2 (1992) 1219.
- [5] Ozin, G. A.; Ozkar, S. *Adv. Nanochemistry: Synthesis in diminishing dimensions*, *Mater.* 4 (1992) 612.
- [6] A. Zouaoui, O. Stéphan, M. Carrier, J.-C. Moutet, Electrodeposition of copper into functionalized polypyrrole films, *J. Electroanal. Chem.* 474 (1999) 113.
- [7] J.C. Moutet, A. Zouaoui, Poly[(3-pyrrol-1-ylpropyl)malonic acid]: Synthesis, ion-exchange properties and complexation of copper cations, *J. Electrochim. Acta* 46 (2001) 4035.
- [8] T. Melki, A. Zouaoui, B. Bendemagh, I.M.F. de Oliveira, G.F. de Oliveira, J.C. Leprêtre, et al., Electrosynthesis and catalytic activity of polymer-nickel particles composite electrode materials, *J. Braz. Chem. Soc.* 20 (8) (2009) 1523.

Gas Sensing Mechanism of Metal Oxide Doped PANi Composites

Kailash R. Nemade and Sandeep A. Waghuley

Department of Physics, Sant Gadge Baba Amravati University, Amravati 444 602, India

Received: December 03, 2012 / Accepted: January 06, 2013 / Published: May 25, 2013.

Abstract: Novel hybrid gas-sensitive materials were made-up by means of metal oxide (MOX) doped organopolymers. The hybrid gas-sensitive materials were prepared by varying molar concentration of Bi_2O_3 and Y_2O_3 MOX in conducting polymer PANi. The hybrid materials have tested upon exposure to LPG gas. The sensitivity of both composites materials was studied at room temperature. The gas sensing mechanism explained on the basis of chemisorbed/adsorbed oxygen. The materials were characterized by FTIR and SEM analysis.

Key words: Gas sensing, metal oxide, PANi.

Nomenclature

PANi: Polyaniline

1. Introduction

Polymer-metal or metal oxide nanocomposite is a new class of material that combines the advantages of both organic polymer material and inorganic metal or semiconductor oxide and shows improved optical, electrical and mechanical properties for gas sensor applications. The gas sensing properties of films depend not only upon the individual components used but also on the morphology and the interfacial characteristics. The composite films that combine materials with synergetic behaviours possess unique physical, chemical, optical, mechanical, magnetic and electrical properties unavailable from that of the component materials and have attracted much attention for a wide range of device applications such as gas sensors. Recently, various nanocomposite films consisting of either metal-metal oxide, mixed metal oxides, polymers mixed with metals or metal oxides, or carbon nanotubes mixed with polymers, metals or

metal oxides have been synthesized and investigated for their application as active materials for gas sensors. Design of the nanocomposite films for gas sensor applications needs the considerations of many factors, such as the surface area, interfacial characteristics, electrical conductivity, nanocrystallite size, surface and interfacial energy, stress and strain, etc. which depend significantly on the material selection, deposition methods and deposition process parameters. The conducting polymers have shown great promise in sensory applications. The localized electronic states combined with the restriction on the extent of delocalization makes most of the conductive polymers behave like p-type semiconductors. As these polymers are redox-active, their conductivity can be changed by means of doping/dedoping. A great number of sensing applications are designed by exploiting nature of conducting polymers [1]. Cioffi, et al. investigated polymer films embedded with Pd or Au nanoparticles for detecting vapours of organic solvents [2].

The importance of environmental gas monitoring is well understood and much research has been focused on the development of suitable gas sensitive materials. Recently, there has been considerable interest in exploiting organic substances such as porphyrin,

Corresponding author: Sandeep A. Waghuley, Ph.D., professor, research fields: sensors, conducting glasses. E-mail: sandeepwaghuley@sgbau.ac.in.

phthalocyanines and doped conductive polymers for this purpose. The conducting polymers are good candidates for the elaboration of chemical or electrochemical sensors. Among the conducting polymers, polyaniline (PANi) is a promising sensing material and can be synthesized by chemical, electrochemical or plasma methods, and in each case, the composition, morphology and physical properties of the resulting polymer are strongly dependent on the detailed reaction conditions [3].

In present work, two different composites were synthesised by chemical route. The PANi/Bi₂O₃ and PANi/Y₂O₃ composites were prepared by varying molar concentration of MOX. The prepared samples were characterized by FTIR analysis on shimadzu (model: 8400s). The morphology of powders was investigated by using JEOL-JSM (Model-6063) SEM instrument.

2. Experiments

AR grade (SD fine, india) chemicals were used for this work. The composites PANi/Bi₂O₃ and PANi/Y₂O₃ were prepared by chemical route. The ammonium persulphate was used as oxidant for polymerisation of PANi. The samples of Bi₂O₃/PANi composites were prepared of 0.5 M and 1 M tested for LPG gas whereas Y₂O₃/PANi composites prepared by varying molar concentration from 0.4-2 M. The thick films of prepared samples were fabricated by screen-printing method on SiO₂ substrate. The silver electrodes were coated on the films for electrical contact purpose. The electrical resistance of the film was measured by using a voltage drop method.

3. Results and Discussion

3.1 FTIR Analysis

The FTIR spectra of the PANi/Bi₂O₃ and PANi/Y₂O₃ composites powder samples were recorded in the range 4,000-400 cm⁻¹ to confirm polymerisation shown in Figs. 1 and 2, respectively. The FTIR spectrum of the PANi base shows six principal

absorptions at 1,590, 1,508, 1,304, 1,210, 1,145 and 831 cm⁻¹. The peaks at 1,590 cm⁻¹ and 1,508 cm⁻¹ are assigned to C-C ring stretching vibrations. The peaks at 1,304-1,310 cm⁻¹ correspond to N-H bending. The bands at 1,145 and 831 cm⁻¹ can be attributed to the in plane and out-of-plane C-H bending modes, respectively. The corresponding peaks for the PANi salt appear at 1,560, 1,482, 1,306, 1,245.9, 1,148 and 814 cm⁻¹, respectively. The peak at 2,390 cm⁻¹ could be attributed as due to NH stretching mode and the 1,653 cm⁻¹ bond to the NH bending vibration [4]. The several peaks from 400 to 600 cm⁻¹ attributed to vibration of Bi-O bonds displayed in Fig. 1, confirming the formation of Bi₂O₃ [5]. The peak observed in Fig. 2 at 415 cm⁻¹ which may be attributed to the presence of Y-O bond in Y₂O₃ [6].

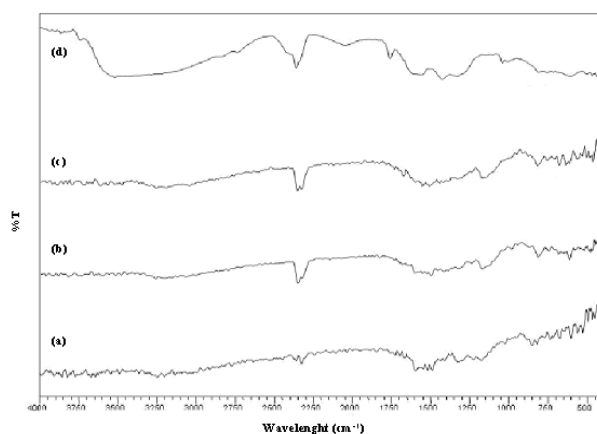


Fig. 1 FTIR spectra of (a) PANi; (b) 0.5 M; (c) 1 M and (d) Bi₂O₃.

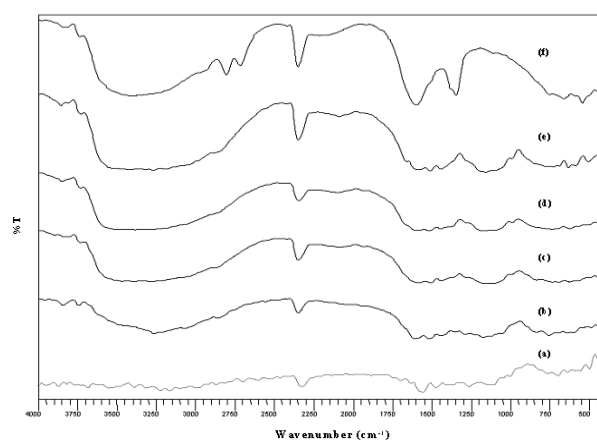


Fig. 2 FTIR spectra of (a) Y₂O₃; (b) 0.4 M; (c) 0.8 M; (d) 1.2 M; (e) 1.6 M and (f) 2 M.

3.2 SEM Analysis

The SEM analysis examined the surface topography of prepared samples and the representative images are shown in Figs. 3 and 4. The SEM reveals an agglomerated powder with a fluffy appearance. This process yields highly agglomerated composite material with fluffy morphology, which play vital role in capturing the gas molecules. This type of morphology highly functional in gas sensing action.

3.3 Sensing Response

The PANi/Bi₂O₃ composites thin films were tested towards LPG gas at room temperature. The sensor response is defined as in Eq. (1) [7].

$$S = (R_g - R_a)/R_a \quad (1)$$

where, R_a is the resistance of sensor in air and R_g is the resistance in gas, respectively. The resistance of the films was found to be decrease with concentration of LPG. Sensing response of the films was measured for different concentration of LPG gas at room temperature Fig. 3. The gas chamber having volume 5 L attached to sensing system for sensors testing. Gas was introduced in chamber with the help of injection. Each injection has capacity to inlet 38 mg LPG.

The sensing responses of PANi/Y₂O₃ composites films were also tested toward LPG gas shown in Fig. 4. The sensor response is defined as Eq. (1). The resistance of the films was found to be decrease with concentration of LPG gas.

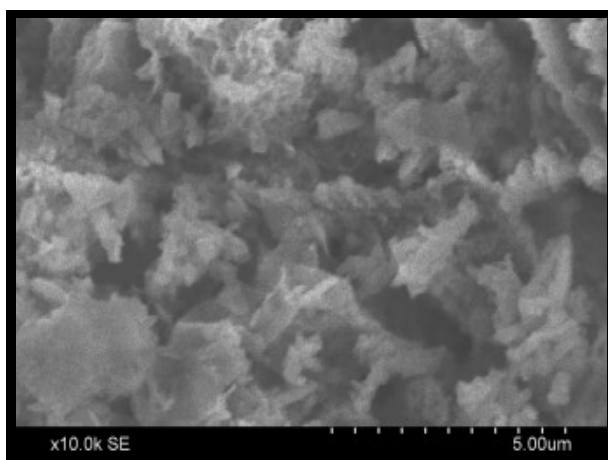


Fig. 3 SEM micrograph of Bi₂O₃(0.5 M) doped PANi.

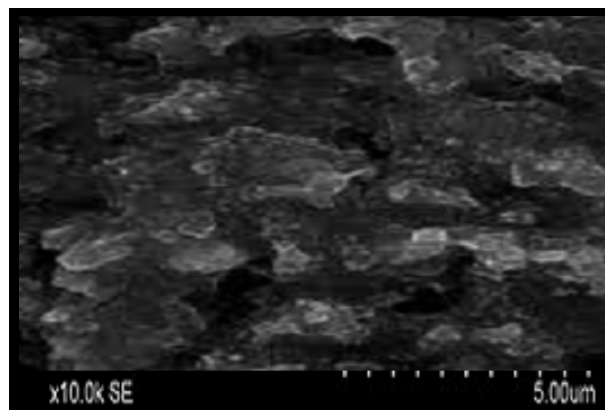


Fig. 4 SEM micrograph of Y₂O₃ (0.4 M) doped PANi.

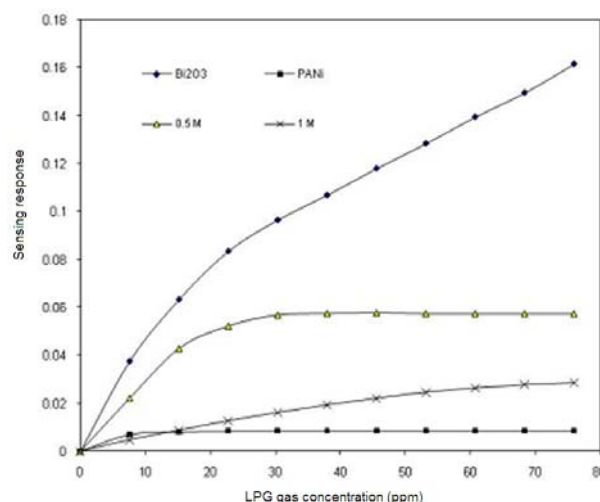


Fig. 4 Sensing response of and PANi/Bi₂O₃ composites.

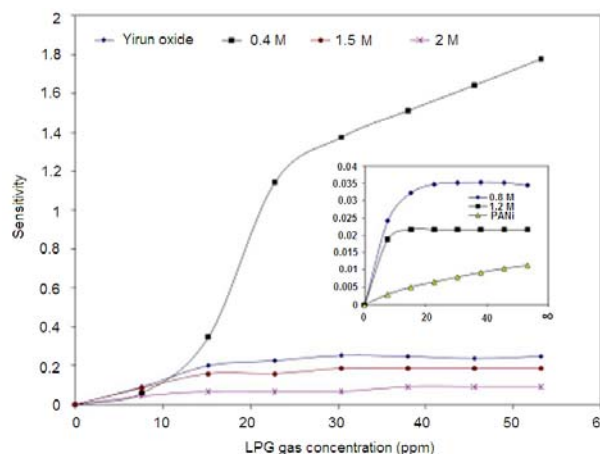
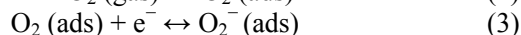
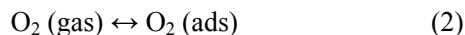


Fig. 5 Sensing response of PANi/Y₂O₃ composites.

The sensing mechanisms for prepared materials were described on the basis of chemisorptions reaction. The chemisorptions reaction play different role for oxidising gas and reducing gas. The sensing mechanism for both composites explained from

reaction on the sensor surface, resulting in a change in concentration of adsorbed oxygen. This reaction may be represented as Eq. (2) and Eq. (3) as follows



The free electron shown in Eq. (3) on left hand side affected by the nature of gas. The oxidising gases inject electrons from material surface, where as the reducing gases added electrons in the bulk of materials. Therefore, resistance of materials was found to be increase in presence of oxidising gas. On the other hand, resistance of materials were found to be decrease in presence of LPG gas due to its reducing nature.

4. Conclusions

The FTIR analysis of both composites confirmed the polymerisation of aniline monomer and composites bonding. The morphology of prepared samples studied by SEM micrograph. The surface morphology play imperative role in analysis of sensing mechanism. The sensing response found to be higher for pure Bi_2O_3 from PANi/ Bi_2O_3 composites at room temperature, whereas the (0.4 M) PANi/ Y_2O_3 composite shows higher sensing response.

Acknowledgments

Authors are very much thankful to Head, Department of Physics Sant Gadge Baba Amravati University, Amravati for providing necessary facilities.

References

- [1] S.C. Hernandez, D. Chaudhari, W. Chen, N. Myung, A. Mulchandani, Single polypyrrole nanowire ammonia gas sensor, *Inter Science* 19 (2007) 2125-2130.
- [2] N. Cioffi, L. Torsi, I. Farella, D. Altamura, A. Valentini, N. Ditaranto, et al., Deposition and analytical characterization of fluoropolymer thin films modified by palladium nanoparticles, *Thin Solid Films* 449 (2004) 25-33.
- [3] R. Kumar, S. Singh, A.K. Misra, Development of NO_2 gas sensor based on plasma polymerized nanostructure polyaniline thin film, *J. Minerals and Materials Characterization & Engineering* 9 (2010) 997-1006.
- [4] J. Stejskal, Polyaniline, preparation of conducting polymer, *Pure Appl. Chem.* 74 (2002) 857-867.
- [5] F. Miyaji, T. Yoko, S. Sakka, Effect of Bi_2O_3 on physical, optical and structural studies of $\text{ZnO}-\text{Bi}_2\text{O}_3-\text{B}_2\text{O}_3$ glasses, *J. Non-Cryst. Solids* 126 (1990) 170-175.
- [6] T.K. Vishnuvardhan, V.R. Kulkarni, C. Basavaraja, S.C. Raghavendra, Synthesis, characterization and a.c. conductivity of polypyrrole/ Y_2O_3 composites, *Bull. Mater. Sci.* 29 (2006) 77-83.
- [7] K.R. Nemade, R.S. Palspagar, K.A. Koparkar, S.S. Kosalge, G.T. Bhalerao, G.G. Muley, et al., Sensitivity and dynamic response of Zinc oxide thin films to carbon dioxide gas, *Bionano Frontiers (Special Issue)* (2010) 133-135.

Evaluation of Effect of Eddy Currents in PLC Influenced by Atmospheric Corrosion in the Electronics Industry

Gustavo López Badilla¹, Elizabeth Romero Samaniego², Sandra Luz Toledo Perea², Miriam Maleny García Castellon³ and Luis Alberto Gameros Rios³

1. Researcher-Academic, Technological Institute of Mexicali (TIM), Mexicali, Baja California, México

2. Researcher-Academic, Technological Institute of Ensenada (TIE), Ensenada, Baja California, México

3. Students of Electronic Engineering, Technological Institute of Mexicali (TIM), Mexicali, B.C., México

Received: March 22, 2013 / Accepted: April 15, 2013 / Published: May 25, 2013.

Abstract: Inductive proximity sensors contain an internal coil. When a current flow through it, a magnetic field is generated, which has the direction of the electric currents involved in it, as electrical flow in the input or output area. The coil or winding of the inductive sensor induces Foucault currents in the material to be detected, that are originated by eddy currents. These electrical flows generate a magnetic field, which opposes to the sensor coil, causing a reduction in the inductance of micro inductors of electronic devices. This reduction of the internal inductance originates bad function in the micro inductors used in the programming logic controller (PLC). This PLC is in the manufacturing processes of the electronics industry and reduces their operation yielding. Sometimes the actuators of these electronic systems not operate correctly, and causing stops in the activities of industrial equipments and machines, being a factor of economic losses. A study of micro evaluation of these inductors which are elements of the relays of PLC was made to determine the influence of corrosion in these components. The analysis showed micro corrosion in these devices with images obtained of the scanning electron microscopy (SEM) and also was made a correlation of the climatic factors as relative humidity (RH) and temperature with the corrosion rate (CR). The evaluation was made in indoor of an industrial plant which fabricate microelectronic components in Mexicali city. The major factors, which cause an adverse effect in the operation of PLC of this industrial plant was the humidity and sulfurs, which originates the deterioration of components of PLC. The study was made from 2010 to 2011.

Key words: Foucault currents, PLC, micro corrosion, electronics industry.

1. Introduction

In the electromagnetic process, the induced current is forced to follow well defined paths through wires made of conductive material. The electrical equipment are formed by parts, pieces of conductor moving in a magnetic field or are located in a variable magnetic field, leading to circulating currents induced by the conductor volume. These are called eddy currents or Foucault currents. When placing a piece of metal in a magnetic field varying with time $B(t)$, generates an electric field that produces a motion of free charges in

the metal conductor, causing an electromagnetic field as is mentioned in the next mathematical equation:

$$\oint E \cdot dl = - \frac{d}{dt} \int_s B \cdot dS \quad (1)$$

This Foucault current generates variations in the electromagnetic systems used in the electronics industry [1].

1.1 Foucault Currents

The eddy currents occur when an electrical conductor passes through a variable magnetic field, or vice versa. The relative movement causes an electron flow or current induced within the electrical conductor. These circular currents create electromagnetic fields

Corresponding author: Gustavo López Badilla, Dr., research fields: environment, corrosion, materials and surface analysis. E-mail: glopezbadilla@yahoo.com.

with opposing magnetic fields to the effect of applied magnetic field. If the magnetic field applied is very strong, or the electrical conductivity of electrical conductor is higher, with a high speed or relative motion; the parasite currents and fields will be very high as an opposition of normal electrical current [2]. The cores of coils and transformers are generated induced voltages, due to variations magnetic flux those that are in the cores. These induced voltages are caused by eddy currents, occurring in the core, which are called Foucault currents, and are not optimal for good electrical efficiency of electromagnetic devices. Eddy currents create energy losses through the Joule effect. More specifically, these currents transform electrical energy, as kinetics in unwanted heat, being a negative effect in the electromagnetic of electronic systems. It, decreases the efficiency of many devices using magnetic fields variables such as core transformers iron and electric motors used in the electronics industry. These electrical currents losses are minimized using cores with low magnetic conductivity (such as ferrite) or thin magnetic material sheets, known as laminates. Electrons cannot cross the insulating layer between the laminate and, therefore, no can open circular arcs. Charges accumulate at the ends of the laminate, in a process analogous generate the Hall Effect, producing electric fields that precluding further accumulation of charges and eliminating the eddy currents. If the distance is very short between adjacent laminated, (for example while the number of laminates per unit area are higher, and perpendicular to the applied field), it will remove higher currents Foucault, and therefore less heating of core [3].

1.2 Electromagnetic Induction

A variation of the magnetic flux induces current metal parts, and these currents are called parasites currents. If have an iron and a rotating metal disc around an axis, and a part of the disc passes inside to the magnetic field created by the magnet, will occur a variation of magnetic flux which induces a current in

the object as a variation and represented by Lenz's law [4]. The eddy currents produce two effects: one side is a magnetic brake disc and other heating by Joule effect, which can be inconvenient. This can be reduced to avoid the possible paths inside the metal parts. For example, in the transformers are laminated iron cores minimizing these electrical current losses in the electromagnetic systems and reducing the presence of eddy currents. If compare the function of electromagnetic system with the pendulum operation, the materials are similar, which are constituted by copper plate. Between the poles of an electromagnet is observed to be slowing up completely stopped, this effect occurring rapidly the higher the intensity of field. Being a copper plate material magnetic braking of the pendulum is not due to attraction of the magnet poles. In the plate, when is cutting the flow between the pole pieces, an electromotriz force (EMF) are induced according to Lenz's law. As copper is a good conductor and the plate offers a great the passage section of the flow, its ohmic resistance is small and intense, being induced currents [5]. These currents are opposed to the action of the source produces, and the self-oscillation of the pendulum, thus acting as a brake. These systems operate as similar activities.

1.3 PLC

A programmable logic controller (PLC) is a computer used in automatic engineering or industrial automation to automate electromechanical and electromagnetic processes, such as control of machinery on factory assembly lines of manufacturing areas. PLC is used in many industries and machines. These PLC are designed for multiple input and output to control variables as temperature ranges, immunity to electrical noise, and resistance to vibration and impact and other characteristics presented n the electronics industry [6]. Programs to control machine operation are typically stored in battery backed or non-volatile memories. A PLC is an example of a hard real-time system where the output results must be

produced in response to input conditions within a limited time; otherwise it will not produce the desired results. In recent years, small products called programmable logic relays (PLRs), have become more common and accepted to be used in industrial plants with electronic devices and systems. These are very similar to the PLC, and are used in some activities being one of them, the light industry, where exists few signals coming from the real world and some emerging, that are involved at low cost. These small devices are typically made in a common physical size and shape by several manufacturers, and branded the largest manufacturers of PLC to complete their lower end product range. Most of them are between 8 and 12 digital inputs, 4 and 8 discrete outputs, with 2 analog inputs. The size is usually about 10 cm wide and 7.5 cm high and 7.5 cm deep. Most of these devices include a small LCD screen for viewing simplified ladder logic, only a very small portion of the program is visible at any given time and the status with open and close operations. Normally these screens are accompanied by a four way rocker keypad plus four more separate push buttons, and are used to navigate and edit the logic. Most have a small plug for connecting via RS-232 or RS-485 to a personal computer so that programmers can use simple Windows applications for programming instead of being forced to use the LCD screen and the set of small switches for this purpose. PLC are usually modular and greatly expandable, the PLR are usually not modular or expandable, but their price can be two orders of magnitude less than a PLC and they still offer robust design and deterministic execution logic [4].

1.4 Corrosion in Electromagnetic Devices (EMD)

The majority of industries are characterized by the implementation of manufacturing processes with electronic devices and systems, to control, storage and measure some variables in these industrial processes. The production areas have electrical,

electromechanical, electromagnetic and electronic components. These types of macro and micro devices are exposed to aggressive environments in indoor industrial plants in specially in the electronics industry. These harsh atmospheres have corrosive gases and particles and affecting to these facilities. In specially, the use of electronic devices and boards, with components sensitive to the presence of corrosion, are damaged very easy and fast [7]. It decrease the production yielding of technological systems, and is exposed to significant risks, especially when it comes, the operation of electric circuits or printed boards, that can be attacked by various acid gases found in the atmosphere. Additionally, this problem may go largely unnoticed for the operator, only becoming visible when an error or an unexpected shutdown of a production process. One of the air pollutants in Mexicali city which was made this study, is the hydrogen sulfide, which generates sulfurs with the combination of oxygen of the atmosphere. Electromagnetic devices as relays, which are used in electronic devices as PLC, suffer of the corrosion phenomena, and in sometimes not function very well or as an inoperative component. This concern to specialized people of the electronics industry, where utilized a lot quantity of PLC to control various operations in the manufacturing processes. The presence of corrosion affects directly to PLC of industrial plants, damaging their external electrical connections and connectors, in some times only generating corrosion products and in other times, brakes the metallic contacts of copper. Also deteriorate the internal connectors electrical, which are covered by corrosion products and operate inadequately.

The electromagnetic devices (EMD) are very important systems in the electronics industry [8].

1.5 Electronics Industry in Mexico

The electronics industry is an important key to the industrial development of our country, with favorable evolution in the past decade and a market-oriented

industry transitioned to a competitive industry where it is used mainly for the export market. The most important export products are of high technology with a lot of products, being the principal the televisions, cell phones, computer equipments and decoders, as well as some electro-medical equipment and electronic components with integrated circuits of photosensitive semiconductor devices, switches, control panels, transistors and some capacitors [2]. The electronics industry is very important in the manufacturing industry in Mexico, which is measured through economic indicators such as employment, exports and foreign direct investment. This is clearly an industry dominated by multinational companies have established subsidiaries in Mexico for more than five decades. Five sectors up to the electronics industry: electronics consumer, personal computers, telecommunications equipment, electronic components and industrial and medical equipment. In the second half of the nineties, the electronics industry in Mexico was strongly benefited from the signing of the Free Trade Agreement (NAFTA): the value added grew at an average annual rate of 16.4% between 1994 and 2000. Direct industry grew occupied by 192,000 employees in 1994 to 384,000 in 2000. The period between 2001 and 2003 was outright contraction due to lower global demand and strong competition from other countries, mostly in Asia, among other factors. Figures for 2004 show a significant industry recovery, but still below the levels reached in 2000 [6].

In 2004, the electronics industry in Mexico accounted for 0.9% of the national value added and 4.8% of the manufacturing, and 298,000 workers employed directly. Total exports of the industry in the same year were 42.908 million dollars and for the first time in 10 years presented a deficit in the balance of trade: imports totaled 45.697 million dollars. For its hand, foreign investment totaled \$ 696 million in 2004. The main sectors of the electronics industry in Mexico are consumer electronics, computers personal and

telecommunications equipment, industrial and medical equipment but have been growing at rates higher than the industry average. More than 75.0% of the companies are located in states northern border of the country, mainly in Sonora, Baja California and Chihuahua. Jalisco is the state of inside the country with the largest number of companies in the electronics industry [8].

2. Methodology

Corrosion appeared in the microelectronic devices evaluated in the electronics industry of Mexicali, generating the Foucault currents which have an adverse effect in the electromagnetic systems. For this analysis was evaluating the production yielding of some PLC used in indoor of industrial plants of this city [9]. Also were analyzed climatic factors and air pollution levels to determine the effect in the corrosion rate (CR) of metallic surfaces of PLC. Evaluation was made of internal and external electrical connectors and connections of PLC during the period evaluated and show the corrosion types in summer and winter seasons.

2.1 Materials and Methods

The first process was the evaluation of the operation of relays in winter and summer as electromagnetic devices to analyze the phenomena as a differential transformer with the primary and secondary windings, to detect Foucault currents.

The evaluation of corrosion products to determine the chemical agents that react with the metallic surfaces of copper of electrical connectors of PLC, and know the type of corrosion in each seasons evaluated: summer and winter. The materials used were the electrical connections of PLC deteriorate [10, 11], to correlate with the CR with the concentration levels of hydrogen sulfides (H_2S), sulfur oxides (SO_x), nitrogen oxides (NO_x), ozone (O_3) and carbon monoxide (CO), obtained of the Environmental Monitoring Systems (EMS) with the air quality standards (AQS).

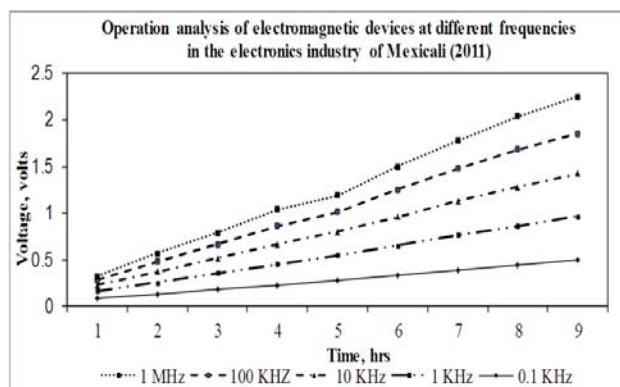


Fig. 1 Evaluation of operation of relays of PLC in an electronics industry in Mexicali (2011).

This information have relevance to the electronics industry, because this chemical agents as particle or gasses, penetrate to indoor of this type of industrial plants. To correlate the information of CR and the concentration levels in indoor of the electronics industry, was measure sulfurs with the technique of sulfatation plate (TSP) [12].

2.2 Atmospheric Corrosion

Atmospheric corrosion (AC) in indoor of the electronics industry is commonly generated by the aggressive environments formed for the presence of sulfurs that in the Mexicali city in winter principally overpass the AQS and damage the metallic surfaces of electrical connectors and connections of the PLC. This originates low capacity in the production processes and in sometimes is necessary stop the manufacturing lines in the industrial areas to repair the PLC or to replace these electronic devices with electromagnetic systems as relays [5].

2.3 Surface Analysis

Corrosion products and type of corrosion forms are evaluated by the SEM technique at different scales, obtained the best illustrations to compare at 500× as the higher view in a microphotography and at 5× the small view to know at very small scale the corrosion process. These microphotographs showed the deterioration of the metallic copper surfaces in each season evaluated [3].

3. Results

The presence of corrosion in electromagnetic devices of PLC is a concerned aspect to managers and owners, which works with the specialized people to reduce or avoid it. This generates a great economic losses by the Foucault currents appeared that decrease the productive yielding of the electromagnetic components and originates expensive costs by the generation of heat in these type of devices used in the electronics systems.

3.1 Effect of Foucault Currents in Operation of EMD

Foucault currents originate the loss of electrical current of the electromagnetic devices, and depending of the frequency of operation, is the magnitude of this current loosed. In this study, an analysis of a relays as a mean, used in the PLC by 9 h a day, in every day of the week, in three months, showed the different operation of this electronic devices at 0.1 KHz, 1 KHz, 10 KHz, 100 KHz and 1 MHz (Fig. 1).

As showed the last figure, the output voltage at different frequencies are represented the volts that loss the electromagnetic devices indicated in the evaluation process. At 0.1 KHz, the lowest voltage loosed was around 0.01 V and the highest was 0.02 V. In the 1 KHz, was showed a maximum voltage loosed of 0.025 V with a minimum was 0.3 V. At 10 kHz, the smallest value was 0.035 V and the biggest the 0.045 V and in the 100 KHz the highest magnitude was 0.09 V and the smallest was 0.04 V. At 1 MHz the maximum value of loosed voltage was 0.12 V and the minimum was 0.06 V. This meaning, that at high frequency values are loosed more quantity of volts, and at this magnitude of frequency operate the electromagnetic devices of PLC by the reduced times to function.

3.2 Correlation of CR, Climatic Factors and Air Pollution

All figures represents the relation between the CR of cooper and the climatic factors evaluated in this study, as are RH and temperature, associated to the

principal air pollutants mentioned above. The chemical agent who promotes the corrosion process with major negative effect in copper and silver probes was the H_2S in the first three graphs, and in the Fig. 4, was the SO_x added with the NO_x . The summer analysis shows the higher values of CR than in winter season in both metallic specimens evaluated. In all ranges, the CR was very fast and generates the higher negative effect, showing pitting corrosion with all air pollutants evaluated, in some areas of the metallic probes. In an electrical connection or connector, this electrochemical process will be a cause of an electrical resistance and in a short future can be deteriorate very fast these electrical components. This will avoid the electrical conductivity and turn off the industrial equipments and machines, which decreases the manufacturing productivity. The air pollutants were represented in the analysis by different colors: H_2S as light green, SO_x with light blue, NO_x as dark bluer, O_3 with blue green and CO as yellow for the average of 2011 in all chemical agents. The analysis was in the summer and winter seasons to compare the values of the concentration levels of air pollutants evaluated. To the Fig. 2, in August of 2011, indicates the H_2S generates a maximum CR was 233 $gr./m^2 \cdot year$ at 84% of RH, 41 °C of temperature and 0.035 ppm. In this season, the SO_x generate a major CR of 177 $mgr./m^2 \cdot year$, at 87% of RH, 38 °C of temperature and 0.23 ppm. The effect of NO_x in the CR, originates the higher value of 132 $gr./m^2 \cdot year$ at 83% of RH, 40 °C and 0.12 ppm. The O_3 have an negative effect, generating a maximum CR of 182 $gr./m^2 \cdot year$ at 87% of RH, 37 °C of temperature and 0.15 ppm and the CO generates a major CR of 193 $gr./m^2 \cdot year$ at 84% of RH, 42 °C of temperature and 42 ppm.

The same process occurs in the Fig. 3, indicating the month of December 2011, where the CR presented was in major grade of deterioration of CR, than in summer. In this period of analysis, the maximum CR influenced by H_2S was 255 $gr./m^2 \cdot year$ at 87% of RH, 20 °C of temperature and 0.056 ppm. For the SO_x ,

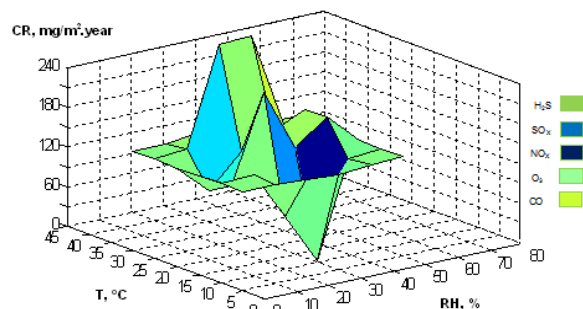


Fig. 2 Correlation of CR of cooper with climatic factors in summer in Mexicali (2010). AQS of air pollutants: H_2S (0.03 ppm), SO_x (0.14 ppm), NO_x (0.05 ppm), O_3 (0.12 ppm), CO (35 ppm).

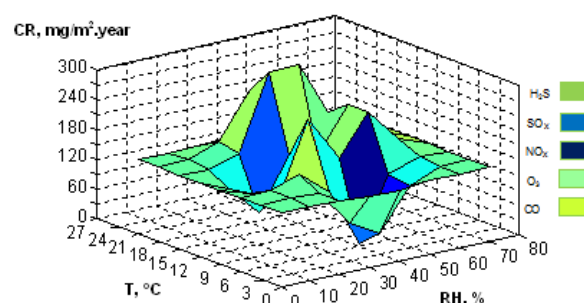


Fig. 3 Correlation of CR of cooper with climatic factors in winter in Mexicali (2010). AQS of air pollutants: H_2S (0.03 ppm); SO_x (0.14 ppm); NO_x (0.05 ppm); O_3 (0.12 ppm) and CO (35 ppm).

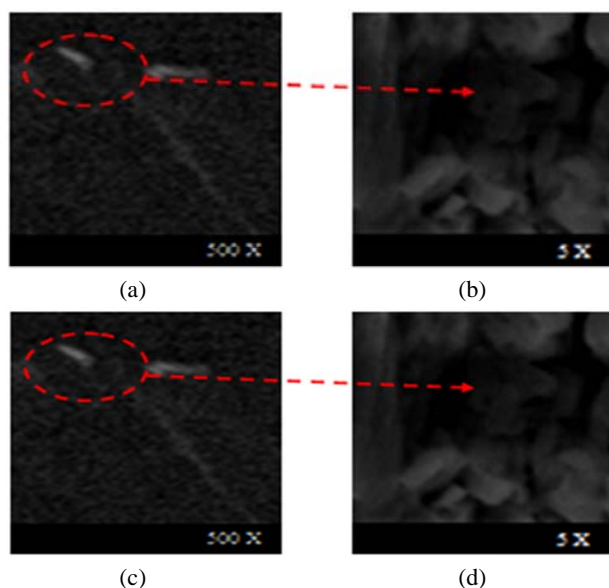


Fig. 4 Microanalysis of the deterioration of metallic surfaces of electrical connectors and connections of electromagnetic devices of PLC evaluated in indoor of a electronics industry in Mexicali (2011) in summer at (a) 500x; (b) 5x; winter at (c) 500x and (d) 5x.

the higher value of CR was 242 gr./m²·year at 82% of RH, 19 °C of temperature and 0.39 ppm. With the effect of NO_x the major CR was 152 gr./m²·year at 86% of RH, 21 °C and 0.27 ppm. To the O₃, the maximum CR was 239 gr./m²·year, at 82% of RH, 18 °C of temperature and 0.32 ppm and to the CO the CR higher value of was 158 gr./m²·year at 47% of RH, 31 °C of temperature and 76 ppm.

3.3 Microanalysis of Surfaces of EMD Deteriorate

SEM technique show the deterioration of the metallic connectors and connections of electromagnetic devices used in the PLC. Fig. 4 indicates at 500× the uniform corrosion in the majority of the surface and at 5× represents the pitting corrosion presented in a small zones of the surfaces evaluated. This damage was in the areas of electrical pathways, causing electrical failures in these types of electronic devices and systems. In the red line are showed the major deterioration.

The pitting corrosion appeared, was occurred by the variations of RH and temperature and the air pollution levels that exceed the AQS, showing the great major damage in winter than in summer. In both are represented at 5×, pitting corrosion, but in winter in the same scale are bigger than in summer.

4. Conclusions

The corrosion that occurs in industrial plants, generates great economic losses, which concern people involved in these areas. Various research institutions on ways to know the origin of the different types of corrosion that can occur. One of the types of companies, where is a major concern on this topic, is the electronics industries, where occur constantly the corrosion phenomena. The electromagnetic devices suffer a variety of problems in their conduction areas in the surface films by exposition of air pollutants. When combined atmospheric agents with variations in RH and temperature, metallic materials used in the electronic systems as PLC, decrease their resistance

corrosion of the connectors and conductive paths. This causes the formation of metallic filaments that grow between routes driving and rigid and flexible circuits between electrical connections and connectors as metallic pins or electrical unions. With increasing miniaturization of systems electronics and the explosive increase in its availability, it is estimated that the corrosion and deterioration of metal materials electronic, with incalculable consequences. The characteristics of modern electronic equipment high voltage contemplate factors, speed of operations, very small currents, miniaturization and extremely sensitive to corrosive agents. This can lead to some failures generate technical and atmospheric pollutants that attack metallic materials of electronic devices.

References

- [1] P. Dillon, MTI & DOE Launch Project Partnerships, Communications Materials Technology Institute of the Chemical Process Industries, Inc., 2000.
- [2] B.G. López, Characterization of corrosion of metallic materials in the electronics industry in Mexicali, Ph.D. Thesis, B.C., 2008. (in Spanish)
- [3] B.G. López, S.B. Valdez, K.R. Zlatev, P.J. Flores, B.M. Carrillo, W.M. Schorr, Corrosion of metals at indoor conditions in the electronics manufacturing industry, *Anti-Corrosion Methods and Materials* 54 (6) (2007) 354-359.
- [4] B.G. López, S.B. Valdez, W.M. Schorr, V.H. Tiznado, H.G. Soto, Influence of climate factors on copper corrosion in electronic equipments and devices, *Anti-Corrosion Methods and Materials* 57 (3) (2010) 148-152.
- [5] L.B. Gustavo, V.S. Benjamin, S.W. Miguel, R. Zlatev, T.V. Hugo, S.H. Gerardo, et al., AES in corrosion of electronic devices in arid in marine environments, *Anti Corrosion Methods and Materials* 58 (6) (2011) 331-336.
- [6] A. Moncmanova, *Environmental Deterioration of Materials*, Universidad de Sevilla, WIT Press, Spain, 2007, pp. 108-112.
- [7] L. Veleza, B. Valdez, G. López, L. Vargas, J. Flores, Atmospheric corrosion of electro-electronics metals in urban desert simulated indoor environment, *Corrosion Engineering Science and Technology* 43 (2) (2008) 149-155.
- [8] R. Zlatev, B. Valdez, M. Stoycheva, L. Vargas, G. López,

M. Schorr, Simposium 16: NACE "Corrosion and Metallurgy", IMRC 2009, Cancun, Mexico.

- [9] ISO 9223:1992, Corrosion of metals and alloys, corrosivity of atmospheres, classification.
- [10] ISO 11844-2:2005, Corrosion of metals and alloys, classification of low corrosivity of indoor atmospheres, determination and estimation attack in indoor atmospheres, ISO, Geneva, 2005.
- [11] ISO 11844-1:2006, Corrosion of metals and alloys, Classification of low corrosivity of indoor atmospheres, Determination and estimation of indoor corrosivity, ISO, Geneva, 2006.
- [12] ASTM G91-11, Standard Practice for Monitoring Atmospheric SO₂ Deposition Rate for Atmospheric Corrosivity Evaluation.

The Influence of the Concentration of Dissolved Substances in the Effluent Sulfate Pulp and Paper Mills on the Productivity of Semi-Permeable Membranes

Terpugov Grigory¹, Truberg Arseniy², Katsereva Olga¹ and Terpugov Daniil¹

1. Borisa Galushkina str., Moscow 17, 224 Russia

2. Geroev Panfilovcev, Moscow 3/1, 349 Russia

Received: November 14, 2012 / Accepted: December 16, 2012 / Published: May 25, 2013.

Abstract: The ability of treatment of pulp and paper production wastewater is showed by carbon-graphite and polymeric membranes. The influence of lignins, organic and inorganic substances containing in wastewater on specific capacity is studied. Capacity calculation of different types of membrane is suggested.

Key words: Membrane, specific capacity, sulphate pulp mill, waste water.

1. Introduction

The pulp and paper industry (PPI), along with woodworking enterprises occupy first place in terms of waste water, wasting almost 1.5 billion m³ of wastewater per year.

Waste water from PPI entering on the treatment facilities contain considerable amounts of suspended and dissolved substances both organic and inorganic. Their composition is very diverse. This is due to the fact that during the production of cellulose about 50% of organic substances of wood goes into solution, forming a concentrated liquor, some of which (5%-20%) falls in the effluent.

The use of membrane technology in the pulp and paper industry is most promising in three ways [1]:

Obtaining commercial products of improved quality.

Pre-concentration of liquor by reverse osmosis in advance of concentration by evaporation [2-4].

Membrane technology can also be used to

concentrate the weak liquor, which formed at the stage of pulp washing.

The objective of this work was to study the influence of the concentration of multicomponent solutions on the specific productivity of membrane separation process, and getting the dependencies that could be recommended for technological calculations of membrane equipment for wastewater treatment. [5, 6]

2. Experiments

Studies were conducted on model solutions prepared by diluting the concentrated black liquor and real solutions of sulphate pulp and paper industry wastewater. We used as ultrafiltration (carbon graphite) membranes and reverse osmosis (composite) membranes with the characteristics shown in Table 1.

When choosing a membrane for process of wastewater treatment guided by the fact that the development of generalized method of calculation needed a membranes made of different materials and different specific productivity, selectivity and the degree of "compactibility" in a fairly wide range.

Corresponding author: Terpugov Grigory, professor, research fields: ecological and environmental problems, membrane processes. E-mail: mamont58@mail.ru.

Table 1 Characteristics of the membranes.

Type of membrane	Conditional notation (brand name)	The pore size (μm)	The selectivity of the membrane ϕ of 0.15% solution of NaCl (%)		Specific productivity of clean water G_0 ($\text{l/m}^2\cdot\text{h}$)	
			$P = 1.96$ (MPa)	$P = 3.43$ (MPa)	$P = 1.96$ (MPa)	$P = 3.43$ (MPa)
Carbon-graphite	1U	0.4-0.6	-	-	-	55.83
	2U	0.4-0.6	-	-	-	56.23
	3U	0.6-0.8	-	-	-	69.21
	4U	0.6-0.8	-	-	-	68.44
	5U	0.8-1	-	-	-	98.105
Composite	OFAM	-	79.60	86.72	29.61	32.86
	MGA-80	-	72.55	80.10	24.14	27.04
	MGA-90	-	89.04	91.24	20.53	23.40
	OPAM	-	85.32	89.84	28.24	31.91

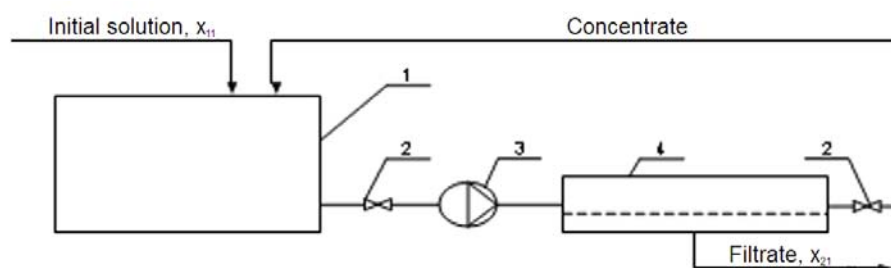


Fig. 1 The experimental setup of membrane separation. (1) container, (2) cock, (3) pump and (4) membrane module.

The concentration of dissolved solids were determined by standard methods. The timing of the experiments ranged from 1 to 40 h, depending on the operating pressure, type of membrane and quantity of extracted samples needed for analysis [7].

Schematic diagram of the apparatus is shown in Fig. 1.

In the experiment recorded the concentration of the filtrate, and the performance of the membranes.

Analysis of published data on the dependence of the osmotic pressure of the solution of Na_2SO_4 and sulphate liquor [1] of the solution concentration (Fig. 2) suggests that Na_2SO_4 is a major component that contributes to the osmotic pressure of sulphate liquor. Based on this conclusion, the study of the influence of the concentration of dissolved substances in the effluents of sulfate pulp and paper industry on the specific productivity, count towards only the ion content of Na^+ .

In the generalized method of determining, the productivity of different types of membranes, used productivity in the shape of a relative value of G/G_0 ,

for the possibility of applying the developed methodology to the membranes that differ by type of material and productivity. Fig. 2 shows the experimental dependence of the relative productivity (the ratio of the productivity of the membrane G to its productivity for distilled water, G_0 , containing approximately 10 mg of Na^+/l and in some cases determined by the manufacturer and indicated in the passport of the membrane) of carbon-graphite membrane and composite membranes at an different operating pressure on the logarithm of the concentration of sulfate liquor mg of Na^+/l .

3. Results and Discussion

The analyzing the experimental data revealed that it is possible to determine productivity of the membranes as a function on the concentration of sulfate liquor without conducting a series of experiments. We propose the following method of constructing design line:

- With the help of Fig. 2, or other literary data for depending on the osmotic pressure of the concentration

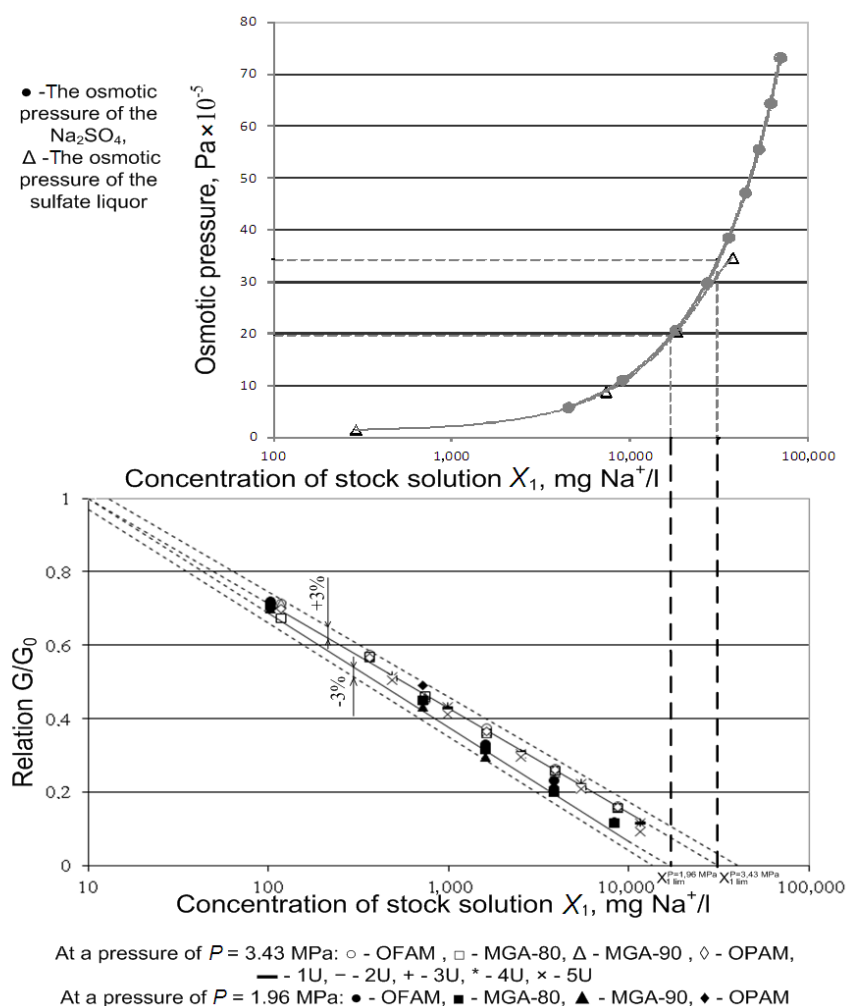


Fig. 2 (a) The dependence of the osmotic pressure of the solution concentration, (b) the dependence of the relative productivity of composite and carbon-graphite membranes on the concentration of sulfate liquor.

of Na_2SO_4 at an operating pressure, is determined by the limiting concentration of sodium ions $x_{1 \text{ lim}}$, in which there is no driving force for membrane separation process, and, hence, productivity;

- For any type of membrane relative performance will be equal to unity at a concentration of 10 mg of Na^+/l .

- Line, drawn through these two points of the described by the equation:

$$G/G_0 = b - c \cdot \lg x_i \quad (1)$$

c , the slope of the line; b , a point of intersection with the axis of y .

Lines constructed by using the proposed method in Fig. 2 (black solid line in the field of experimental data), demonstrate that this technique are useful for

assessing the performance of different types of membranes depending on the concentration of wastewater kraft pulp production, in the working range of concentrations.

4. Conclusions

Thus, the presented results of experiments on the separation of sulfate wastewaters with the use of composite and carbon-graphite membranes, allow us to conclude that the specific productivity of different types of semi-permeable membranes in a wide range of concentrations of these flows can be calculated with sufficient accuracy. The calculation of the productivity of membrane systems is conducted on the basis of passport data for G_0 , and background data on

the concentrations of Na^+ -ions in a solution of Na_2SO_4 , in which the osmotic pressure becomes equal to the worker and the permeability of the membrane vanishes.

References

- [1] J.I. Dytnerky, Baromembrane Processes, Chemistry, Moscow, 1986.
- [2] Best Existing Technologies in Paper and Pulp Industry, Ecology and Business, St. Petersburg, 2004, p. 600.
- [3] Technological normatives of wastes and emissions of contaminants and volumes of wastes of pulp and paper plants in Russia 4.1.4.2, Ecology and Business, St. Petersburg, 2004, p. 600.
- [4] G. Terpugov, The development of process wastewater and process liquids with the use of membrane technology: Dis. ... dock, Those, Sciences, Moscow, 2000.
- [5] V.N. Balitsky, T.V. Kirsanova, E.A. Komyagin, V.N. Mynin, G.V. Terpugov, V.A. Kirsanov, Usage of membrane technology in pulp and paper industry, Ecology and Industry in Russia 7 (2002) 33-35.
- [6] N. Afanafyev, O. Brovko, T. Lichytina, L. Parfenova, Technology of fraction division and ultrafiltration of technical lingosulphates, Pulp, Paper, Pasteboard 1 (2007) 60-62.
- [7] A. Truberg, O. Silos, G. Terpugov, Influence of concentrations of dissolved substances in wastewater of sulphate pulp plants on selectivity of semipermeable membranes, Chemical Industry 11 (2010) 38-42.

Classification of Raw Sources of Rare-Earth Elements in Kazakhstan

Madali Naymanbayev, Nina Lokhova and Zhazira Baltabekova

JSC "Center of Earth Sciences, Metallurgy and Ore Beneficiation", Almaty 050010, Kazakhstan

Received: February 21, 2013 / Accepted: March 27, 2013 / Published: May 25, 2013.

Abstract: The characteristics of the mineral composition of ores and valuable set of components: The technology of processing depending on the type of mineralization, the nature of the impregnation of ore minerals and their composition have been considered. There have been given technological schemes for processing concrete objects. The analysis of fitness fields for industrial development (degree of scrutiny, the effectiveness of developed enrichment and hydrometallurgy technology) has been provided.

Key words: Rare-earth-rare-metal deposits, technological research, enrichment, hydrometallurgy.

1. Introduction

World mining of rare earth metals has rapidly grown in the last 15 years and it has been increased for than twice.

One of the major problems of rare earth industry creation and development in Kazakhstan is raw material provision.

Kazakhstan disposes of significant deposits of rare earth elements (RARE EARTH ELEMENTS (REE) in the minefields of different in genetic type and complexity. However, on quality Kazakhstan ore deposits are significantly inferior to foreign one presented with high-tech rich ore deposits of rare earth itself [1]. In the ores of Kazakhstan complex deposits REE are available in low concentrations and being as supplementary associated components.

Ores are diverse, complicated in technological manner and processing them requires nonroutine solutions.

2. Results and Discussion

Description of rare-earth deposits and associated rare-earth metals deposits.

Analysis of outcomes of physical & chemical and technological researches maintained in studying a number of deposits containing rare earth elements, indicates that the following elements can be considered for potentially-industrial production of rare earth products with regard to complexity of their development [2]:

- Carbonatite deposits: containing zirconium, niobium, tantalum, scandium, rare earth elements, Krasnomayskoe deposit, in Akmola region, in which elements of the cerium group are 92%-93% in the amount of REE (37%-42% cerium, lanthanum 18%-20%, 15%-18%, neodymium 15%-18%);
- Albite granites containing: niobium, tantalum, zirconium, rare earth elements, Borsyksay deposit, in Aktobe region (the content of the sum of rare earth elements up to 0.19%, of which the yttrium group is up to 0.011%) and upper Espe;
- Stratified deposits: Vanadium deposits Balasauskandyk in South Kazakhstan region are the most attractive among them (the content of rare earth elements is 0.02%-0.053%) and Kurumsak in

Corresponding author: Madali Naymanbayev, PhD (Eng), research fields development of theoretical bases and creation of effective rational technologies of complex processing of polymetallic, titanite, magnesite and rare-earth raw materials with extraction of valuable components. E-mail: madali_2011@inbox.ru.

Kyzylorda region (REE content is 0.041%-0.092%).

Karatau phosphorus deposits: Sholaktau, Zhanatas, Aksay, Cox and Kokdzhon differs with industrial concentrations of rare earth elements. A content of the amount of rare earth elements varies from 614 to 1,088 g/t. Elements of yttrium group are dominating among the rare earth elements.

The content of the sum of the individual rare earth elements and rare earth elements are summarized below [3]:

- Zhanatas field: the average content of ΣREE 614 g/t; including yttrium 300 g/t; ytterbium 4.0 g/t; cerium 110 g/t; lanthanum 200 g/t.
- Aksai field: the average content of ΣREE 938 g/t, including yttrium 440 g/t, ytterbium 8 g/t, cerium 210 g/t, lanthanum 280 g/t.
- Sholaktau field: the average content of ΣREE 1,088 g/t; including yttrium 520 g/t; ytterbium 8.0 g/t; cerium 250 g/t; lanthanum 310 g/t.
- Kokdzhon field: the average content of ΣREE 630,5 g/t, including yttrium 312 g/t; ytterbium 5.5 g/t; cerium 138 g/t; lanthanum 175 g/t.
- Cox field: the average content of ΣREE 700 g/t, including yttrium 376 g/t; ytterbium 6.0 g/t; cerium 166 g/t; lanthanum 152 g/t.

Considering the unique Karatau phosphorus reserves and high content of rare earth elements, they should be considered one of the primary sources of rare earth elements in the country.

Uranium-bearing deposit Melovoe ($Y/\Sigma\text{REE} = 21.5\%$), located in Mangistau region, is also related to this group. In the 80s of the last century there were received yttrium and heavy lanthanides concentrates.

- Weathering crust (deposits Kundybay, Akbulak, Kostanai region). Rare earths and yttrium are located in the ion-sorption shape and form their own minerals.
- Titanium-zirconium placers containing rare earth metals in zircon, monazite and xenotime. The total content of rare earth metals in the Obukhov placer (Akmola region) in the minerals of the heavy fraction is 0.45%, and zircon from 0.1% to 1.9%.

Practical interest represent the upper Espe ($Y/\Sigma\text{RZM} = 11.7\%$), located in the Semipalatinsk region [4].

The field is represented by two stock formed outputs of alkali granites (big and small), the dimensions are 3 and 1.5 km². The granites are characterized by higher (2-10 times more than clark) concentrations of zirconium, niobium, tantalum, lithium, thorium, yttrium and rare earth metals.

Rare-metal and rare-earth-metal mineralization with industrial content of metals is concentrated in two types of ore, alkaline (albitized) mineralized granites and metasomatic reversed rocks (fenites).

The content of rare earth elements in mineralized granites is 0.1%-0.57%; an average of 0.25% and in fenites, 0.1%-0.64%; an average of 0.48%. Vein-shaped ore bodies and pegmatite of grand exit are most enriched with rare earth metals.

The main mineral containing rare earth metals, gagarinit, which contains 58.3% of REE stocks, 48.4% are concentrated in the pyrochlore and zircon. Yttrium and rare earth metals of the yttrium group are present mainly in Gagarinit, which is easily opened with acids. The main carrier of the cerium group, pyrochlore, also can be found bastnezit, monocyte, cerium gagarinit and fluorite. Dysprosium is concentrated in gadolinite, morit, ittrobastnezite, fergyusanite. Gadolinium and erbium is concentrated in xenotime and ittrosinhizite. Ytterbium, yttrium and erbium are the most common in Torit and feretories.

The deposit Upper Espe requires further exploration and further research on the enrichment of finely disseminated ores.

Of rare-earth deposits actually explored the most interesting ore occurrence is Kundybay ($Y/\Sigma\text{REE} = 33.4\%$), located in Kostanai region, it is associated with the Mesozoic weathering crust of ancient metamorphic rocks.

Weathering crust is zonal. Composition of the zones depends on the weathering level and is due to the ratio of relict and newly formed minerals. The

former include amphibole, mica, graphite, retile, ilmenite, sphene, titan magnetite, kulsonit; to the second: kaolin, limonite, gibbsite, goethite, hydro micas, rare earth elements.

Study of mineralogical characteristics of raw materials showed that Kundybayskoe ore occurrence represents a new genetic type of deposits of rare earth elements, which does not have analog in the world [5]. It is characterized by coupling with the crust of weathering of metamorphic rocks, previously unknown association of minerals of rare earth elements (Churchit, ittrorabdofanit, neodymium and ytterbium bastnezit), significantly yttrium composition, with uniquely high content of europium and other deficient lanthanide. A considerable part of the rare earth elements are situated in non removable by flotation and gravity methods forms of enrichment, probably in the structure of clay minerals.

Among the rare-earth deposits associated with weathering crusts the promising field is Akbulak ($Y/\Sigma REE = 34.4\%$) located in the Kostanai region [6].

The deposit is confined to linear weathering crusts developed along the southeast contact of the granite-gneisses from the Precambrian slates, within the rare-earth-rare-metal zone with the length 17 km, the width of 2-3 km. Crushed stone and clay-wood weathering crust are the productive ones. Mineralization can be traced throughout the section of the weathering crust. The depth of the roof of the ore deposit varies from 0.50 to 33.0 m, foot, from 4.0 to 64.5 m, average reservoir thickness, 13.2 m.

Linear strip ratio, assuming a development of the open method, varies from 0.0 (in the southern part) to 1.5 (in the central and northern parts of the deposit). The average content of yttrium oxide is 272 g/t (at carrying 100 g/t, the amount of oxides of rare earth elements is 790 g/t).

The main ore minerals are xenotime, rabdofanit, Churchit, bastnezit, tsirtolit. Perhaps some rare metal and rare earth elements are in ionic form and are associated with mica, clay minerals of the weathering

crust, as well as hydroxides of iron and manganese.

On material composition it is similar to the deposit Kundybay, and rare earth mineral rabdofanit is of larger size.

Besides of the group of rare earth elements installed on the field and can be simultaneously extracted: tin (50-100 g/t), silver (15.10 g/t), niobium (10.30 g/t), gallium (10.30 g/t), lithium (30-40 g/t).

Throughout the deposit were estimated reserves as per category C2, prospected resources R1, with a minimum capacity 4.0 m and cut-off grade of 100 g/m of yttrium oxide.

The deposit Akbulak requires resuming exploration work to refine the inventory and perform research to develop technologies for extraction of rare earth elements for industrial development of the field.

3. Engineering Researches

Based on the type of rare metals and rare earth mineralization, composition and structure of the ore various technological schemes are proposed, based on both the complex beneficiation and hydrometallurgical processing as well as on hydrometallurgical technologies directly, as shown in the example of few deposits.

Their main peculiarities are primary enrichment (after grinding to the optimal size corresponded to average grain size of rare metal minerals) with gravity methods using jigging machines, spiral separators and concentration tables, final processing of gravity concentrates using magnetic and electrical separation.

The staff of the Eastern Research Institute of Nonferrous Metals (ERINM) investigated the possibility of enrichment the ore deposits of Upper Espe to extract the pyrochlore, zircon, gagarinit, monazite, bastnasite to the products suitable for hydrometallurgical processing. It is recommended gravity scheme of material enrichment with fineness of $-0.044 + 0.2$ mm and $-0.0044 + 0.02$ mm [7].

It was proposed to complete the scheme on the cycle of obtaining complex concentrate. The resulting

complex concentrates contain masses.‰: Nb_2O_5 6.42-7.75; ZrO_2 17.0-28.1; $\Sigma\text{REE}_{\text{oxides}}$ 1.09-2.55. with the extraction of ore 40.9-43.4; 19.5-31.0 and 15.8-37.0, respectively to that.

Nabiev (Uzbekistan), Favorskaja (Kazakhstan) in 50-60 years were involved in technology of extraction of rare earth metals and yttrium at the processing of phosphate [8]. According to them 73.5%-80.0% of rare earth elements metals and yttrium transfers into solution during the decomposition of phosphate with 20% nitric acid at a stoichiometric ratio. The resulting solution was neutralized with ammonia in a mixture with air. On the content of rare earth elements in the sediment pH plays an important role. The yield of sediment and concentration of rare earth elements in it is inversely proportional to each other. In the sediment obtained at pH 2.0, contained 5.1% and at pH 0.4%-37.5% of the amount of oxides of rare earth elements. The optimal deposition was taken at pH 1.2. The proposed method was not implemented in production.

On superphosphate plants in Kazakhstan and Uzbekistan Karatau phosphorus ore are processed for fertilizer by sulfuric acid method, in which only 27% of rare-earth metals are dissolved, transfers into fertilizer and applied to land, and the remaining 73% fall in waste of production.

Technological studies of kundybayskie titanium-yttrium-rare earth ores were conducted in 1965-1998.

It was found that the natural minerals of rare earth elements are mainly represented with phosphates [9]:

- Churchite: is found only in the weathering crust. The content from trace to 5,700 g/t, noted with high content of europium;
- Xenotime: the content from traces to 244 g/t;
- Monazite: content from trace to 151 g/t;
- Rhabdophanite: content from trace to 19 g/t;
- Bastnasite: content from trace to 528 g/t, in some samples up to 2,440 g/t;
- Hydrophosphate REE: new water mineral that is

found only in the weathering crust, the contents from trace to 341, in some samples 5,747 g/t.

The most common is the churchite, its maximum concentration in some samples is 5.1%. However, the total content of rare earth elements in all found own minerals is only slightly (2-3 times) higher than clark values for the Earth's crust and constitutes 15%-25% of the total content of rare earth metals in the ore.

In the heavy (sand) fraction, the main carriers of the rare earth elements are their own minerals, primarily Churchite. In the light fraction of weathering crust rare earth elements are contained in adsorbed associated state, probably at the nodes and between nodes of the structural lattice of clay minerals in the form of individual ions and small aggregates, which are released during weathering of rock-forming minerals.

Very subtle germination and accumulation of rare earth metals in waste rock causes the difficulties of traditional methods of enrichment. Under the scheme, which provides granular concentration of ores and magnetic separation of crude concentrate, obtained a product containing 3% of rare-earth elements oxides, at the extraction of 13.9%. Flotation method obtained a concentrate containing 1.35% of rare-earth elements oxides, at the extraction of 12.6%.

In this regard, big prospects have ways of hydrometallurgical extraction of rare earth elements, based on de cation exchange or complete destruction of the lattice of minerals and the transference of rare earth elements into solution. The most effective appear to be relatively simple and economical method, developed by employees of Chemical and Metallurgical Institute (Karaganda city, Kazakhstan) under the guidance of Sharipov, et al. [7].

It consists in leaching raw ore with 18-20% of sulfuric acid solution, the separation of high-silicon sludge and the solution with decanting method, the sorption of rare-earth elements with cation KU-2-8 elution with the solution of 10%-20%, sulfuric acid solution and the allocation of 25% concentrate of rare earth elements in the form of the oxides. According to

calculations made by developers of ways of pounds cost 25% concentrate of REE was 45% of its market value (the price of that period).

Preliminary technological research of Akbulak ores, in two samples, showed total extraction of rare earth elements 62% (sulfuric acid leaching method) and 94% (using nitric acid), followed by processing of solutions with known methods to obtain individual rare earth elements.

4. Conclusions

Rare-earth elements occurring in rare-metal minerals mainly consist of calcium, niobium, tantalum, titanium, strontium, thorium, Uranus, fluorine, carbon and phosphor, including sodium and silicon in alkali massive.

Rare-earth minerals can be divided into two major groups: minerals with rare-earth minerals as the main/one of the main elements (monazite, xenotime, bastnaesite etc.), and minerals with rare-earth minerals as the associated elements, which partially replace the main elements (apatite, phosphorite, zirconium, Uranus, titanium etc.).

Summarized raw materials of all the above mentioned fields are significant and provide an opportunity to select objects according to their degree of preparedness and scrutiny, to create a production of rare earth concentrates and metals in Kazakhstan.

References

- [1] L.Z. Bykhovskii, S.D. Potanin, Geological and industrial types of rare earth deposits, Raw Minerals, Geological and Economic Series, Moscow: Publishing SIMS 28 (2009) 157.
- [2] A.A. Abdulin, H.A. Bespaev, E.S. Votsalevskij, Deposits of rare metals and rare earths in Kazakhstan, Almaty, 1998, p. 136.
- [3] A. Dzhurumbaev, V.N. Urich, Prospects for integrated processing of Karatau phosphate for fertilizers. Collection: Phosphates and alumina silicate based on mineral resources of Kazakhstan, Alma-Ata: Nauka (1984) 29-33.
- [4] E.I. Semenov, Mineralogy of Rare Earths, USSR Academy of Sciences, Moscow, 1963. p. 412.
- [5] A.A. Pocoluev, L.P. Rihvalov, S.L. Nikolaev, On the complex nature of uranium ores and rare metal deposits of the North Kazakhstan ore province, in: Materials of the International Conference "Mineral Resources, a key factor in the integration of Kazakhstan into the global economy", Almaty, 1993, pp. 169-171.
- [6] N.L. Radenko, T.D. Koretskaya, On the prospects of the rare-earth mineralization in Kazakhstan, in: Materials of International Conference "Toporkovsk reading" Ore., 1999, pp. 187-195.
- [7] B.S. Uzhkenov, G.R. Bekzhanov, L.B. Ivanov, Rare metals and rare earths in Kazakhstan, Almaty, 2011, p. 277.
- [8] M.N. Nabiev, Nitric acid processing of phosphates, Tashkent, 1976, p. 367.
- [9] S.M. Ulasyuk, V.S. Kiseleva, The study of the material composition and technological characteristics of the rare-earth weathering crust, Process Evaluation of Mineral Resources (1981) 38-44.



Journal of Materials Science and Engineering B
Volume 3, Number 5, May 2013

David Publishing Company
9460 Telstar Ave Suite 5, EL Monte, CA 91731, USA
Tel: 1-323-984-7526, 323-410-1082; Fax: 1-323-984-7374, 323-908-0457
<http://www.davidpublishing.com>, www.davidpublishing.org
materials@davidpublishing.org, materials1934-8959@hotmail.com

